DESIGN OF AN ELECTRICALLY SMALL WEARABLE ANTENNA WITH A REACTIVE IMPEDANCE SUBSTRATE OPERATING AT 433 MHZ

by

Martin Roestorff

Submitted in partial fulfilment of the requirements for the degree
Master of Engineering (Electronic Engineering)

in the

Department of Electrical, Electronic and Computer Engineering
Faculty of Engineering, Built Environment and Information Technology

UNIVERSITY OF PRETORIA

August 2016

SUMMARY

DESIGN OF AN ELECTRICALLY SMALL WEARABLE ANTENNA WITH A REACTIVE IMPEDANCE SUBSTRATE OPERATING AT 433 MHZ

by

Martin Roestorff

Supervisor:	Prof JW Odendaal
Co-supervisor:	Prof J Joubert
Department:	Electrical, Electronic and Computer Engineering
University:	University of Pretoria
Degree:	Master of Engineering (Electronic Engineering)
Keywords:	Reactive impedance substrate, wearable antenna, electrically small antenna, radiofrequency identification

The primary objective of this investigation was the development of a design procedure for a compact wearable antenna operating at 433 MHz that can be used for finding lost miners in underground mines in emergency situations. To accomplish this objective the antenna was to have a relatively high gain of 5 dBi, and a compact size at less than 0.5 λ_0 by 0.5 λ_0, where λ_0 is the wavelength of 433 MHz in a vacuum. The chosen solution was to use a basic antenna with a reactive impedance surface (RIS) reflector. As it was known beforehand that the final product would be large, and therefore expensive, it was decided to use a low-cost material to manufacture the antenna. FR-4 was selected as the antenna’s dielectric material because it is inexpensive and readily available, at the cost of having high dielectric losses.

Various RIS designs were investigated, and the square patch RIS was found to be most suitable for this application. The final RIS design was a 2 by 2 square patch RIS. It was deemed unnecessary to use a complex antenna design, due to the fact that the RIS was already rather large. It was decided to use a basic planar monopole antenna, because integrating even a basic antenna with an RIS would result in a very complex model.

The final antenna was developed by first designing an RIS unit cell to have a zero-degree reflection coefficient phase at the design frequency, then the antenna was designed to

resonate at the design frequency. Both the RIS unit cell and antenna were first optimised for the design frequency before being combined to form the integrated antenna. The integrated antenna was then optimised according to the design goals.

Two antennas were designed, one for optimal performance, and the other to be as compact as possible. The first of the two antennas, the standard planar monopole antenna, had a wide practical -10 dB impedance bandwidth of 25.1 %, with more than 5 dBi boresight gain over the same frequency band. The second of the two antennas, the loaded planar monopole antenna, used the standard planar monopole antenna as a starting point before optimising for as compact a size as possible, whilst maintaining practical performance. The loaded planar monopole antenna achieved a practical impedance bandwidth of 5.28 %, with at least 5 dBi boresight gain over the same frequency band. The final size of the standard planar monopole antenna was 0.4 λ_0 long, 0.4 λ_0 wide, and 0.069 λ_0 high, and the final loaded planar monopole antenna was 0.346 λ_0 long, 0. 346 λ_0 wide, and 0.107 λ_0 high.

Concerning wearability, human loading did not detune either of the antennas in such a way as to render the design frequency of 433 MHz outside the respective impedance bandwidths. The front to back power ratio, i.e. the ratio between the average power radiated into the front hemisphere and the average power radiated into the rear hemisphere, was larger than 10 dB in the two antennas’ respective -10 dB reflection coefficient bands. This means that if a human were to wear one of these antennas, the antenna’s performance would not degrade, and the majority of the radiated power will be radiated away from the human.

In summary, a design procedure was developed, two antennas were designed through said procedure, and the final designs were manufactured. The manufactured antennas verified the design procedures and proved that they are practical. The final designs achieved the goals for this investigation by being compact, wearable, and relatively inexpensive.

LIST OF ABBREVIATIONS

A	Ampere
BAN	Body area network
BW	Bandwidth [Hz]
c	Speed of light [m/s]
C	Coulomb
cm	Centimetre
CST	Computer simulation technology (2014 version)
dB	Decibel
dBi	Antenna gain in dB relative to an isotropic antenna
EM	Electromagnetism
f	Frequency [Hz]
F	Farad
$FBW_{\pm 90^\circ}$	Fractional bandwidth from +90° to -90°
f_c	Centre frequency
FR-4	Flame retardant 4
FSS	Frequency selective surface
g	Gram
GSM	Global system for mobile communications
GSM900	GSM band at 900 MHz
GSM1800	GSM band at 1800 MHz
H	Henry
Hz	Hertz
JC	Jerusalem cross
JC-FSS	Jerusalem cross frequency selective surface
IFA	Inverted-F antenna
K(z)	Complete elliptic integral

kg	Kilogram
m	Metre
mW	Milliwatt
MHz	Megahertz
n	Number of molecules per unit volume
PIFA	Planar inverted-F antenna
rad	Radians
RIS	Reactive impedance surface
RF	Radiofrequency
RFID	Radiofrequency identification
SAR	Specific absorption rate [W/kg]
$\tan \delta$	Loss tangent
UHF	Ultra-high frequency (300 MHz to 3 GHz)
UMTS	Universal mobile telecommunications system
V	Volt
W	Watt
Z	Impedance [Ω]
α	Molecular polarizability [$\mathrm{C \cdot m^2/V}$]
ε	Dielectric permittivity [F/m]
ε_0	Dielectric permittivity of free space [F/m]
ε_r	Relative permittivity [F/m]
η	Intrinsic wave impedance [Ω]
η_0	Free space wave impedance [Ω]
θ	Spherical coordinate: altitude [degrees]
λ_0	Wavelength in free space [mm]
λ	Wavelength in dielectric medium [mm]
μ	Magnetic permeability [H/m]

μ_0	Magnetic permeability of free space [H/m]
μ_r	Relative permeability [H/m]
φ	Spherical coordinate: azimuth [degrees]
ω	Radian frequency [rad/s]
Ω	Impedance

TABLE OF CONTENTS

CHAPTER 1 INTRODUCTION

1.1 PROBLEM STATEMENT

1.1.1 Context of the problem

In underground mines radiofrequency identification (RFID) systems operating at 433 MHz are common as they are used to keep track of personnel, equipment, and supplies. The miners in underground mines typically have low-powered RFID systems on their person that communicate with other tracking systems. This tracking system lets the user know how many miners are underground, where they have been working, and where they are currently located. In an emergency situation where miners get trapped or lost underground, these tracking systems help by giving rescuers the last known location of the miners, but it cannot assist after searching has commenced. To that end rescuers can employ a system that can actively communicate with the RFID systems on the lost or trapped miners, thereby allowing the rescuer to ascertain where the miners are relative to their own position. A possible solution would include a directional antenna that can be worn by the rescuer while they are looking for miners [1, 2, 3].

As research into antenna miniaturisation has allowed for the realisation of antennas small enough to be considered wearable at increasingly lower frequencies, the possible applications for body area networks (BANs) have increased. BANs, which can allow for wireless communication between different subsystems located on a single human, as well as allowing wireless intrapersonal links between a BAN and remote systems, can now be implemented over an ever increasing range of frequencies [4, 5, 6]. This has led to the development of more and more antennas that can be used whilst being worn by a human.

Some advancements have been made in the use of BANs in consumer products, such as adaptive routing techniques and telecommunication systems [4, 7, 8]. A considerable amount of research has also gone into the development of BANs, and by extension antennas, for use in medical applications [5, 9, 10]. It has however been shown that human loading, due to the close proximity between an antenna worn by a human and the human in question, can have an adverse effect on antenna performance – effectively detuning the antenna's input characteristics [7, 10, 11].

The antenna in [5] managed to solve the human loading issues in the 2.4 GHz medical band. This antenna made use of an artificial magnetic conductor (AMC), which has been known to enable antenna miniaturisation as well as bandwidth improvements [12, 13, 14]. A reactive impedance surface (RIS) was used in [15] to decrease the size, and increase the bandwidth, of a patch antenna in the frequency range of 420 MHz to 450 MHz. This antenna was designed to have a directional radiation pattern, and to be insensitive to platform effects when mounted on a vehicle. The RIS was designed on what is described as a low loss ceramic with a dielectric constant of 10.2, a description that best fits the SMAT-10 ceramic that has a loss tangent of smaller than 0.00015 and a density of 3.46 g/cm^3 [16]. As this antenna was operational at 433 MHz it has paved the way for directional wearable antennas operating in the radio-frequency identification (RFID) frequency band. The drawbacks of this antenna include the high manufacturing costs due to expensive materials, and the challenges to customisability due to the complex RIS implementation used.

1.1.2 Research contribution

The contribution provided by this study is the design of antennas that can be used for finding lost miners in underground mines. The antennas were designed for 433 MHz, and each used an RIS to improve the wearability of the antennas by increasing the percentage of energy radiated away from the wearer, whilst maintaining a compact size. The antennas were realised on a low-cost lossy substrate with very basic antenna and RIS designs. The main research contribution of this study was to improve upon the results that have previously been achieved by reducing design complexity and cost.

1.2 RESEARCH OBJECTIVES

This study will focus on the design of a low-cost, RIS backed, directional, wearable antenna. The research objectives for this study are summarised below:

- The primary objective of this study is the development of a design procedure for a low-cost, RIS backed, directional, wearable antenna. Care will be taken to ensure that the design is as simple as possible by removing unnecessary features and using only basic shapes.

- A secondary objective of this study is to investigate the effect of the loss tangent of materials used on the antenna's performance.
- A cursory investigation will be done on the trade-offs for making the antenna as small as possible. This investigation will be facilitated by comparing the performance of an antenna that was optimised for size against an antenna that was optimised for performance.

1.3 APPROACH

The operating principles for RIS backed antennas will be thoroughly investigated before choosing RIS configurations with an acceptable trade-off between performance and complexity. The different RISs will be designed for use at 433 MHz and compared in terms of performance and complexity. After choosing the optimal RIS it will be combined with a planar monopole antenna and the RIS and antenna will then be optimised in simulation for performance and size. Based on the aforementioned steps a design procedure will be compiled to aid future designers.

An investigation will also be done in simulation on the effect of the loss tangent of the dielectric medium used to design the RIS and the antenna. This investigation will be done as a parametric study of the dielectric medium's loss tangent.

Finally, one prototype of each of the antennas will be manufactured – one prototype of the antenna optimised for a compact size, and one prototype optimised for performance. These prototypes will then be evaluated through measurement to validate the simulated results.

1.4 OVERVIEW OF STUDY

Chapter 1 provided context for this study. The problem statement was defined, the research contributions were identified, and the research objectives were specified.

Chapter 2 is an investigation into the literature relevant to this study. The literature study contains research on wearable antennas, antenna miniaturisation, and reactive impedance surfaces (RIS). The designs for a planar monopole antenna, as well as the material properties of Flame Retardant 4 (FR-4) are also investigated.

Chapter 3 is an investigation into the designs for the RIS that is to be used in this study. Two RIS designs are investigated, the square patch RIS and the I-shape RIS, and the best RIS design will be selected. Appropriate design parameters for both RISs will be identified and listed.

Chapter 4 presented the design for a planar monopole antenna, which will be integrated with the RIS designed in Chapter 3. The integrated antenna will be optimised for performance, where the final design will be used as a starting point for a new antenna that will be optimised for compact size. Investigations will also be done into the effects of the loss tangent of the dielectric material, and the effects of human loading on antenna performance.

Chapter 5 shows the results of manufacturing and testing the two antennas designed in Chapter 4. The impedance characteristics will be measured, including the impedance bandwidth and the effect that human loading has on the antennas' impedance bandwidth. Various radiation characteristics will also be measured and compared with simulated results. Through testing the manufactured antennas, the accuracy of the simulation models will be investigated, and in doing so the design procedures will be verified.

Chapter 6 is the conclusion of this dissertation which summarises the results of the study, discusses the findings, and presents recommendations for future work.

CHAPTER 2 LITERATURE STUDY

2.1 INTRODUCTION

RFID systems are commonly used in underground mines to keep track of moving supplies, equipment and personnel. As RFID systems that communicate in the 433 MHz band are already worn by most miners, these systems were identified as an ideal tool for locating lost or trapped miners in emergency situations. One of the most promising methods for locating lost or trapped miners is for a rescuer to wear a directional antenna, which can be used to locate the low power RFID tag worn by the miner [1, 2, 3]. To that end, this study investigates the design of a directional antenna that can be worn by a rescuer in emergency situations in underground mines.

This chapter investigates the challenges involved in designing wearable antennas, as well as presenting some of the most common and effective techniques for improving antenna wearability. Common antenna miniaturisation techniques are discussed, and reactive impedance surfaces (RISs) are investigated in more detail as an antenna miniaturisation technique, for directional planar antennas, as well as for improving antenna wearability. Finally, an investigation is done into Flame Retardant 4, commonly known as FR-4, as a low-cost antenna substrate with the goal of designing a cost effective wearable antenna operating at 433 MHz [17, 18].

2.2 WEARABLE ANTENNAS

The most important considerations in the design of wearable antennas are the size and mass of the antenna, the effects of human loading on antenna performance, and the electromagnetic (EM) energy absorbed by human tissue. The size of an antenna can be modified through the use of antenna miniaturisation techniques, and the mass of an antenna can be modified through the use of materials with different densities. The problem of human loading negatively impacting antenna performance is not easily solved, but an effective method for minimising these effects is to use antenna designs that minimise the near field interactions between antenna and human tissue. To limit the amount of EM energy absorbed by human tissue the output power of the antenna needs to be limited. If higher power is required, an antenna's radiation characteristics should be modified so as to radiate most of its power away from the human wearing the antenna in question, as well as decreasing the amount of reactive energy in the antenna's near field [17, 18].

2.2.1 Improving antenna wearability through miniaturisation

When improving the wearability of an antenna the first step is typically to decrease the size of the antenna. Through miniaturisation an antenna becomes easier to handle, and less obtrusive when worn. If an antenna is miniaturised to improve the wearability of the antenna, be it through introducing meanders, fractals, or meta-materials into the antenna design, care should be taken to not decrease wearability by making the antenna uncomfortable to wear or handle due to the antenna's shape or mass.

According to the Clausius-Mossotti law, provided in Equation (2.1), the dielectric constant (ε_r) of a dielectric material is proportional to the product of the molecular polarizability of the material (α), and the number of molecules per unit volume (n) [19]. As n is directly related to the density of the material, Equation (2.1) shows that, for a given α value, the dielectric constant of a dielectric material will increase as its density increases. Due to the relationship between density and dielectric constant care should be taken when choosing a dielectric material, because using a highly dense material can cause the antenna to be too heavy to be comfortably worn.

$$\frac{\varepsilon_r - 1}{\varepsilon_r + 2} = \frac{4\pi}{3} n\alpha \tag{2.1}$$

2.2.2 Decreasing the negative effects of human loading on antenna performance

As the negative effects of human loading on antenna performance are caused by near field interactions between an antenna and human tissue, these interactions must be decreased if human loading is to be reduced. One method that has had a measure of success is dielectric loaded matching. The method of dielectrically loading antennas in lossy media has been used to improve the performance of both submerged and subterranean antenna systems. This method entails encasing an antenna in a dielectric shell with a similar dielectric constant as the surrounding medium, and thereby insulating the antenna and decreasing the effects of the surrounding medium on the antenna's surface currents [17, 18].

Although dielectric loading is very effective for reducing human loading on implanted antennas, it is not necessarily the most effective method for externally worn antennas. A very effective method for reducing human loading is to design an antenna to have low near field energy. As one of the operating principles for RIS backed antennas is that the RIS reduces reactive near field energy, an RIS can reduce the negative effects on antenna performance due to human loading considerably [5, 14, 20].

Another solution that should be mentioned is the addition of a tuning circuit to the wearable communication system. These tuning circuits can be implemented to always search for the optimal impedance match between the antenna and the rest of the system. Such a tuning circuit typically consists of modifiable capacitive elements, a directional coupler, power detection circuit, and a tuning controller circuit. This solution assumes that human loading will create a mismatch between the antenna and the rest of the system and aims to adapt to this mismatch, rather than prevent it [21, 22].

2.2.3 Limit EM energy absorbed by human tissue

The amount of power absorbed per unit mass – i.e. the absorbed power per unit volume divided by material density – is called the specific absorption rate (SAR), which is used as a measure of the heating rate of tissue. The permissible exposure to EM power for humans is regulated by various agencies who specify the exposure limits as an electric field strength (V/m), magnetic field strength (A/m), or power density (mW/cm^2) for a specified period of time. An efficient way to minimise SAR for wearable antennas is to maximise the component of radiated power that does not contribute to the wearer's exposure [17].

One of the most common indicators of the ratio of transmitted power to power absorbed by human tissue is the front to back ratio of an antenna. The front to back ratio of an antenna is the ratio of the boresight far field magnitude (at $\theta = 0°$, and $\varphi = 0°$ in Figure 2.1) to the far field magnitude in the opposite direction (at θ = 180°, and φ = 0° in Figure 2.1) [5, 17, 23]. This direct front to back ratio does not however conclusively give the ratio of transmitted to absorbed power. Assuming an antenna is worn in such a way that the front hemisphere radiates away from the human, and the rear hemisphere radiates towards the human, the ratio of transmitted to absorbed power is better approximated by calculating the ratio of the average of the radiated power in the front hemisphere and the average of the radiated power in the rear hemisphere.

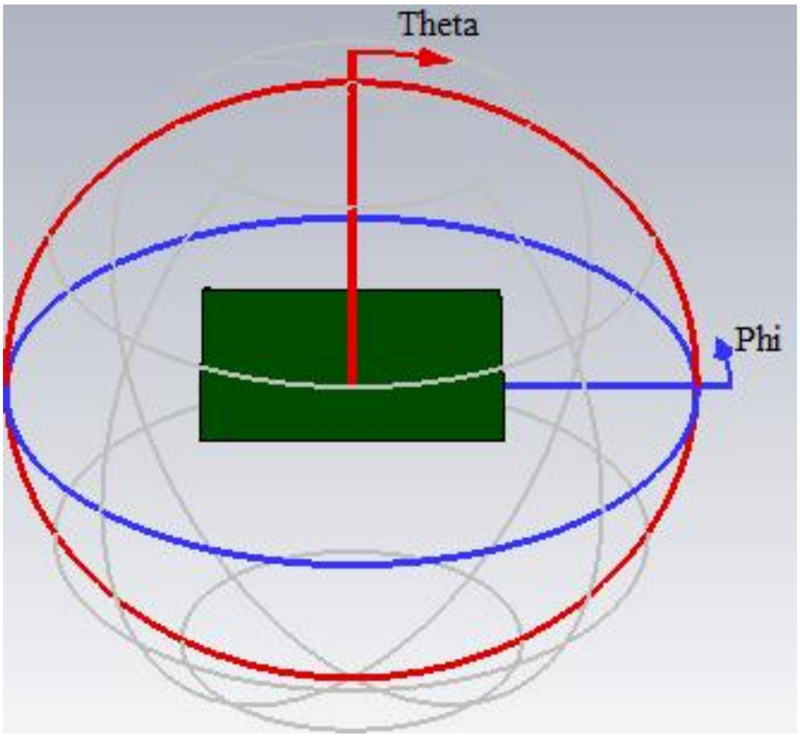

Figure 2.1. Far field spherical angles.

2.2.4 Integrating antennas into clothing

An effective implementation of wearable antenna techniques is to integrate antennas into clothing in such a way as to be unobtrusive for the wearer. This has been achieved by designing antennas that function both as an antenna and as a button, using typical clothing textiles as the antenna substrate, or using specialised textiles that have been designed for use in clothing-based circuits [24, 25, 26]. Another alternative that is being explored is integrating antennas into jewellery items such as rings or earrings [27, 28].

2.2.5 Wearable antennas at 433 MHz

433 MHz falls in the RFID frequency band, and the RFID antennas that are typically designed to be worn are used as receiving antennas, or in short range communication systems. These antennas typically have omnidirectional patterns, low gain (lower than 0 dBi), high losses, or a combination thereof [29, 30, 31, 32]. Directional antennas operating at 433 MHz are typically physically large, such as the antenna from [33] that has dimensions of 250 mm by 250 mm by 8 mm, while achieving a gain of 4.36 dBi and an impedance bandwidth of 5.2 %.

2.3 ANTENNA MINIATURISATION

Antenna miniaturisation is the process of decreasing the size of an antenna by modifying the base design through the use of various methods. This is typically done by altering the form of the antenna, introducing foreign elements into the design, and using different materials for construction [23]. After choosing a substrate with the optimal trade-off between ε_r (relative permittivity), cost, and losses for a specific project, further minimisation can be achieved by modifying the antenna design.

2.3.1 Meandering antennas

One of the most common size reduction strategies currently employed is the use of meandered paths for originally straight antennas such as monopoles or dipoles, which are then also known as meander-line antennas [34, 35, 36, 37]. To create a meander-line antenna the original straight antenna design is modified by folding the radiating part of the antenna so as to decrease its size in one dimension, and increasing its size in another dimension. An example of a meander-line antenna can be seen in Figure 2.2 where a microstrip monopole antenna (shown on the left) is miniaturised as a meander-line antenna (on the right).

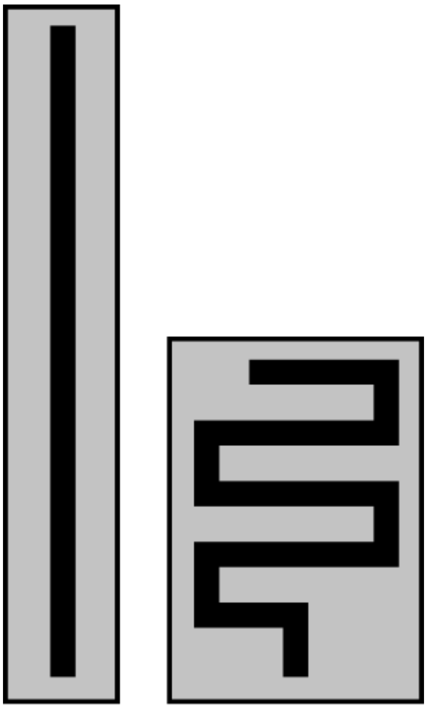

(a) (b)

Figure 2.2. Examples of meander-line antennas where the conductor is indicated in black and the substrate is in grey. (a) Standard monopole. (b) Meandered monopole.

Meanders can also be introduced into slot antenna designs in much the same way as for monopoles and dipoles, except that in this case it is the slot (non-conducting area) that is folded [38, 39, 40, 41]. The main drawback of meandered antennas is that the reduction in size due to meandering also decreases the antenna's impedance bandwidth and gain [37]. In the 1 GHz or higher frequency range the typical gain for a meandered half-wave dipole is around 1 dBi, and the gain for a meandered quarter-wave monopole is about 2.5 dBi [34, 37], compared to 2.2 dBi for a straight half-wave dipole, and 5.2 dBi for a straight quarter-wave monopole [17, 23].

2.3.2 Inverted-F antennas

The Inverted-F Antenna (IFA) is a miniaturised monopole antenna that is formed by folding a part of the monopole wire parallel to the ground plane, to form an inverted L structure. The design is then augmented with a conductor that connects the monopole directly to the ground plane, which forms the iconic inverted F structure. The bandwidth of the IFA can be improved by replacing the antenna wire with conductor strips, which is then referred to as a Planar Inverted-F Antenna (PIFA) [37, 42, 43, 44]. The IFA can also be placed in the same plane as the ground plane to decrease its height – this configuration is called a coplanar IFA [37].

2.3.3 Fractal antennas

The use of fractal geometries as a means for antenna miniaturisation is proposed in [45]. This technique is implemented by introducing fractal folds into the otherwise straight lines of an antenna structure [45, 46, 47]. Typically, the introduction of fractals into an antenna structure decreases the antenna's size, at the cost of decreasing the antenna bandwidth or gain [45, 46, 47, 48].

A Sierpinski fractal structure was shown in [49] to operate in the GSM900, GSM1800, and 2 GHz UMTS frequency bands whilst achieving a size reduction of 40 % compared to a GSM900 monopole antenna. A fractal antenna based on a Durer Pentagon was proposed in [50] and achieved a size reduction of 15 % compared to a pentagon patch antenna operating at the same frequency. Koch curves were used to reduce the size of microstrip patch antennas by as much as 39 % in [51] at the cost of reducing the impedance bandwidth by 27.57 %.

2.3.4 Meta-materials

Meta-materials, also known as meta-substrates or meta-surfaces, are created by introducing either conductive or magnetic materials, or both, into dielectric media. Through the application of carefully engineered meta-materials the properties of the substrate can be modified with the rest of the antenna to achieve superior performance compared to using a standard dielectric substrate. By modifying the relative permittivity and permeability (ε_r and μ_r) of the substrate it is possible to reduce the required size of an antenna, whilst increasing its radiation efficiency. The three most common types of meta-materials are magneto-dielectric, embedded circuit, and reactive impedance surface (RIS) structures [20, 47, 52].

Magneto-dielectric materials are constructed by introducing elements with a μ_r that is larger than 1 into a dielectric medium with an ε_r that is also larger than 1. One of the drawbacks of using a high ε_r material for antenna miniaturisation is that the electromagnetic field is concentrated in the high ε_r areas. This field confinement reduces antenna efficiency. A solution to the field confinement problem is to reduce the ε_r of the substrate, whilst increasing the substrate's μ_r. An antenna can typically be miniaturised by a miniaturisation factor (n) that is equal to the square root of the product of the ε_r and μ_r of the antenna substrate, as indicated in Equation (2.2) below [20, 52].

$$n = \sqrt{\varepsilon_r \mu_r} \tag{2.2}$$

From Equation (2.2) it can be derived that, for a given miniaturisation factor, if the ε_r is reduced by a factor, the μ_r has to be increased by the same factor. In this way a magneto-dielectric material substrate allows a miniaturised antenna to have a higher efficiency than if a standard dielectric substrate were used.

Although magneto-dielectric materials can be very effective, they are typically expensive to manufacture. Two solutions to this problem are embedded-circuit meta-materials and reactive impedance surfaces. Embedded-circuit meta-materials are constructed by introducing multiple resonant loops into a dielectric with low permittivity so as to oppose the magnetic flux of the antenna, and thereby produce an effective permeability. A coupling capacitance is also formed between the loops and the antenna, which produces an effective permittivity. In this way an embedded-circuit meta-material can be modified so as to have ideal permittivity and permeability over the required frequency band [20].

An RIS creates a surface that presents a reactive impedance to an antenna that is somewhere between a perfect electric conductor (PEC) and a perfect magnetic conductor (PMC). An RIS decreases the required size of an antenna, when used instead of a ground plane, by interacting with the antenna and compensating for its capacitive or inductive properties. An RIS consists of a periodic structure over a PEC plane.

2.4 REACTIVE IMPEDANCE SURFACES

An RIS was presented in [14] as a means to increase bandwidth, improve front to back ratio, and reduce the size of an antenna, when used instead of a PEC or AMC reflector. It was therefore decided that an RIS will be used as a part of the wearable antenna design in this study. This warrants deeper investigation into the fundamental operating principles of RISs, as well as an investigation into different types of RISs.

2.4.1 The fundamental operating principles of reactive impedance surfaces [14]

When an antenna is placed in close proximity to a PEC plane, the EM field radiated by the antenna forms an image of the antenna’s electric current. This image current will, in turn, also radiate an EM field that interferes with, and possibly cancels out, the radiated EM field from the physical antenna. For the typically narrow bandwidth where constructive interference occurs the PEC plane will almost double the antenna’s directivity, but the antenna’s performance will decay rapidly as the frequency moves away from its centre frequency.

As an alternative, an artificially magnetic conductor (AMC), which is designed to act as a PMC, can be used instead of a PEC ground plane. The surface currents induced on a PMC plane by an antenna will be in phase and parallel to that of the antenna itself. This means that if the antenna is against the PMC plane the radiated EM fields will add up in phase, aiding impedance matching and increasing bandwidth when compared to using a PEC ground plane. Unfortunately using a PMC plane also increases the reactive near field energy, as was the case when a PEC plane was used. Due to the fact that PMCs are approximated by AMCs, which consist of resonant structures with finite conductor and dielectric losses, this means that the lossy AMC dissipates some of the reactive near field energy, which decreases the antenna’s efficiency.

A PEC presents a plane wave reflection coefficient that causes a phase shift of 180° to the incoming EM field, and an AMC endeavours to present a plane wave reflection coefficient that does not cause a phase shift in the reflected EM plane wave. An RIS on the other hand presents a plane wave reflection coefficient with a phase that varies between -180° and 180°. Because of the variable phase of the RIS plane, the RIS could be designed to compensate for the reactive near field energy of the antenna. This means that if the antenna presents a certain reactive impedance component the RIS can be designed in such a way that the induced antenna image has the opposite reactance, thereby cancelling out the reactive component of the antenna impedance. This allows the antenna to resonate at a much lower frequency than otherwise possible.

In [14] it was shown that the mutual coupling between an ideal dipole is minimised at a normalised reactance of 0.33. This gave rise to a rule of thumb of designing an RIS to present a plane wave reflection coefficient with a phase of 90° as a starting point, and then modifying the RIS to optimise antenna performance (as was done in [5]).

2.4.2 Periodic square patch RIS

The most basic RIS is a periodic array of square patches on a dielectric substrate backed by a PEC plane, as can be seen in Figure 2.3. The equivalent inductor-capacitor circuit is realised by the capacitance that forms between the square patches, and a parallel inductance formed by the PEC plane [14].

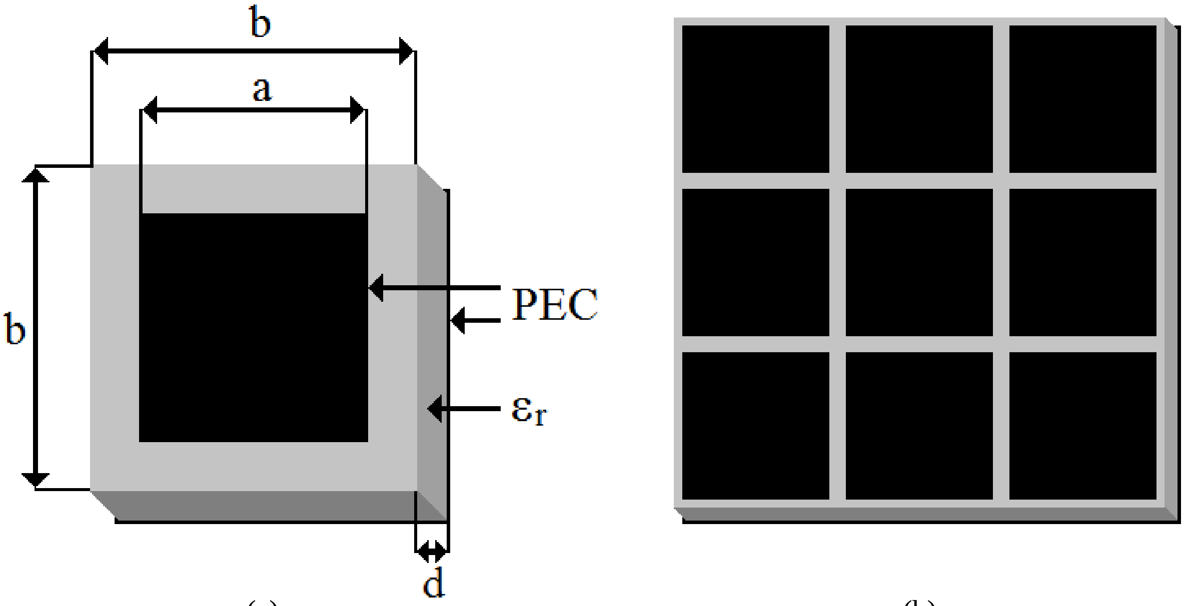

(a) (b)

Figure 2.3. (a) Square patch RIS unit cell. (b) Periodic structure on the right [14].

The impedance (η) of the RIS can be calculated from Equations (2.3) to (2.7) below, where X_L is inductive reactance, X_C is capacitive inductance, j is the imaginary number, and ω is the radian frequency [14].

$$\eta = j\frac{X_C X_L}{X_C - X_L} \tag{2.3}$$

$$Z_d = \frac{\eta_0}{\sqrt{\varepsilon_r}} \tag{2.4}$$

$$X_L = Z_d \tan kd \tag{2.5}$$

$$k = k_0\sqrt{\varepsilon_r} \tag{2.6}$$

$$X_C = \frac{1}{\omega C} \tag{2.7}$$

The capacitance in Equation (2.7) can be approximated through the use of Equation (2.8) and Equation (2.9), where Z_1 is half the distance between the parallel conductors, Z_2 is the width of the conductors plus Z_1, and K(z) is the complete elliptic integral, [14]. The capacitance calculated here is only an approximation due to edge effects changing the effective length of the patches in question.

$$C \approx \frac{a\varepsilon K\left(\sqrt{1-\left(\frac{z_1}{z_2}\right)^2}\right)}{K\left(\frac{z_1}{z_2}\right)} \tag{2.8}$$

$$\begin{aligned} K(z) &= \int_0^{\frac{\pi}{2}} \frac{d\phi}{\sqrt{(1-z^2\sin^2\phi)}} \\ &= \frac{\pi}{2}\left(1+\frac{z^2\cdot 1^2}{2^2}+\frac{z^4\cdot 1^2\cdot 3^2}{2^2\cdot 4^2}+\frac{z^6\cdot 1^2\cdot 3^2\cdot 5^2}{2^2\cdot 4^2\cdot 6^2}+\cdots\right) \end{aligned} \tag{2.9}$$

Although the use of Equations (2.3) to (2.9) will aid greatly in the design of an RIS, it should be noted that these equations assume an infinitely large array of square patches, and a practical error will occur for an RIS that consists of only a few patches. If the RIS can be kept sufficiently large, the practical results will differ from the ideal by a negligible amount. On the other hand, if a 2 by 2 or 2 by 1 patch array is used, the error may be considerable, which will result in the need for some modification.

2.4.3 Jerusalem Cross RIS

Another RIS that has been used with success is the Jerusalem Cross Frequency Selective Surface (JC-FSS). The JC-FSS based RIS was proved effective in applications where the antenna was illuminated obliquely due to its inherently high angular stability [53, 54]. Due to the complex nature of the interactions between the components of a JC-FSS, an effort has been made to improve the equivalent circuit model, and thereby improve the starting point for numerical optimisation [55].

The JC-FSS equivalent circuit discussed in [55] consists of an equivalent capacitance between neighbouring unit cells, and an equivalent series inductance that forms due to the length of a cross. Another inductance forms in parallel to the aforementioned series capacitance and inductance due to coupling between a cross and the PEC at the back of the

RIS. Multiple JC unit cells are required to form an RIS – at least two cells are required to create the capacitive interaction. In a typical case, more than two cells are used to ensure that the differences between the ideal and realised RISs are as small as possible [55, 56]. An example of a 2 by 2 JC-FSS is shown in Figure 2.4 below.

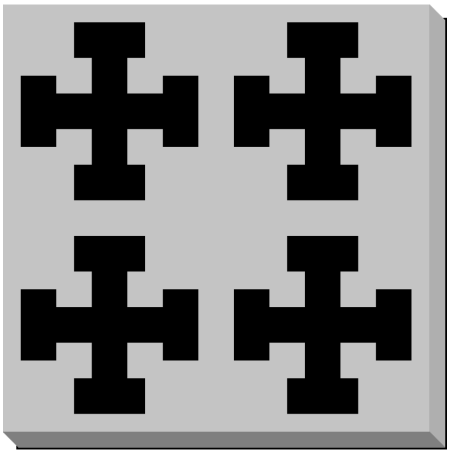

Figure 2.4. Example of a JC-FSS RIS.

2.4.4 Dog bone RIS (I-shape)

The structure of a dog bone (sometimes referred to as an I-shape) RIS unit cell is a simplified version of the Jerusalem Cross unit cell, as can be seen in Figure 2.5 [57]. This simplification can allow for a reduction in the width of the RIS, and decreases the antenna's linear cross polarization. Due to the effect on linear polarization the dog bone RIS is typically used with linearly polarised antennas that are placed above the RIS, parallel to the length of the dog bone shape. Because of the resemblance in form between a JC unit cell and a dog bone unit cell the equivalent circuit for the dog bone RIS is the same as that of a JC RIS [5, 55].

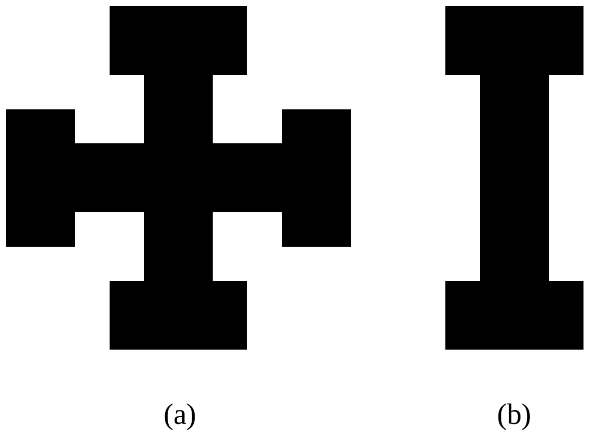

(a) (b)

Figure 2.5. (a) A JC unit cell, (b) A dogbone unit cell.

2.4.5 Crossed dipole with interdigitated capacitors RIS

A more uncommon RIS is the crossed dipole with interdigitated capacitors used in [15]. This RIS is similar to the JC-FSS based RIS, but with increased capacitance due to the configuration of the interdigitated capacitors on the ends of the traditional JC structure. The advantage of this structure is that the unit cells are smaller than in the case of the JC based RIS, which means that the total size of the RIS can be modified in smaller increments than for a JC RIS [15].

2.4.6 Dual-layer mushroom RIS

The dual-layer mushroom RIS consists of 2 layers of overlapping octagons, each of which is connected to the backing PEC plane through a via in the middle of the octagon. The vias improve the angular stability when the size of a unit cell is decreased, while the overlap between mushrooms allows the size of the RIS to be decreased more than if only one layer were to be used. The dual-layer mushroom RIS allows for a direct trade-off between the bandwidth and size of the RIS [58].

2.4.7 RIS applications

An RIS can be used instead of a PEC plane to increase an antenna’s operating bandwidth [14, 15, 54, 59], radiation efficiency [14, 56, 57, 59], angular stability [54, 58], and front to back ratio [5, 14, 56, 60]. An RIS can also be used to decrease an antenna’s size when used instead of a PEC plane [5, 14, 15, 54, 56, 57, 58, 60] and it has been shown that an RIS can decrease the effect of human loading on an antenna's performance [5].

The ability of an RIS to reduce an antenna's size, when used instead of a PEC plane, is typically used in applications where available size is limited, such as an integrated system, or where the antenna in question would be impractically large due to the antenna's radiating mechanism or operating frequency [5, 15, 56, 58, 59]. The improvement to radiation efficiency provided by an RIS is especially useful in applications that use dielectric materials with high dielectric constants, or with high dielectric losses [14, 20, 59].

As the use of an RIS can improve an antenna's front to back ratio it is very useful in wearable antennas, as it decreases the amount of radiated energy that is transferred to the human wearing the antenna. Additionally, the property of some RISs to reduce an antenna's sensitivity to human loading makes the use of an RIS favourable in wearable antennas and antennas that are to be handled by humans during operation [5, 60].

2.5 PLANAR MONOPOLE ANTENNA

A planar monopole antenna was chosen for this study as it has been shown to function well when integrated with an RIS [5]. A planar monopole antenna is a very basic antenna that is easy to modify and manufacture. The planar monopole antenna, as proposed in [61], uses a truncated ground plane to achieve a 2:1 VSWR impedance bandwidth of 60 %, as well as an omnidirectional radiation pattern. For this antenna, an RIS will be used as a planar reflector that will give the antenna a directional radiation pattern.

The design equations proposed in [61] can be seen below. In Equation (2.10) and Equation (2.11) λ_d is the wavelength in the dielectric, λ_0 is the wavelength in free space, ε_r is the dielectric constant of the dielectric medium, c is the speed of light, and f_c is the design centre frequency. L_m from Equation (2.12) is the length of the monopole strip. In Equations (2.13) and (2.14) L_g and W_g are respectively the length and width of the ground.

$$\lambda_0 = \frac{c}{f_c} \tag{2.10}$$

$$\lambda_d = \frac{\lambda_0}{\sqrt{\varepsilon_r}} \tag{2.11}$$

$$L_m = 0.154\,\lambda_d + 0.15\,\lambda_0 \tag{2.12}$$

$$L_g = 0.154\,\lambda_d \tag{2.13}$$

$$W_g = 0.34\,\lambda_d \tag{2.14}$$

2.6 MATERIAL SELECTION

As it was expected that the antenna designed in this study would be large, and therefore expensive to manufacture, it was decided to use a low-cost material that is readily available to keep costs as low as possible.

2.6.1 Flame Retardant 4 (FR-4)

Flame Retardant 4 (FR-4) is a low-cost composite material, consisting of glass fibres embedded in an epoxy resin, with a density of 1.87 g/cm^3 [62, 63]. The complex relative permittivity of FR-4 in the frequency domain (ε) is separated into a real part (ε') and an imaginary part (ε'') as shown in Equation (2.15) [64].

$$\varepsilon = \varepsilon' - j\varepsilon'' = \varepsilon'(1 - j\tan\delta) = \varepsilon_0\varepsilon_r(1 - j\tan\delta) \tag{2.15}$$

The ε_r of FR-4 typically ranges between 4.2 and 5.5, depending on frequency, although it can vary between manufacturers [65]. According to the empirical data provided by [65] the ε_r of FR-4 can be approximated as 4.6 in the region of 433 MHz. While the ε_r of FR-4 typically decreases with frequency, the tan δ of FR-4 is largely independent of frequency [65]. Based on the measured tan δ of FR-4, provided by [65], a worst-case tan δ of 0.02 was used for design purposes to account for possible material quality variation.

2.7 SUMMARY

In this chapter, a review was done on wearable antennas, i.e. what affects antenna wearability, and what are some common techniques to improve antenna wearability. The best techniques for improving antenna wearability include:

- to reduce near field interactions between the human wearing the antenna and the antenna itself,
- to optimise the antenna’s radiation pattern so as to minimise the amount of energy transferred to the human wearing it and thereby maximising the amount of energy radiated away from the human,
- to design the antenna to have a form that can be comfortably worn,
- to minimise the antenna’s size so as to be as light as possible and,

an investigation was also done into prevalent antenna miniaturisation techniques. This investigation was done to provide background knowledge of antenna miniaturisation techniques as an entry point for an investigation into reactive impedance surfaces (RISs), which were also investigated in greater detail. The fundamental operating principles of RISs were examined and the basic periodic square patch RIS was evaluated. A quick look was also taken into some other common RIS configurations.

Finally flame retardant 4 (FR-4) was investigated as the dielectric medium that will be used in this study. It was found that FR-4 has a density of 1.87 g/cm^3, and at 433 MHz it has a dielectric constant of 4.6 and a loss tangent of less than 0.02. It was also found that the material properties of FR-4 can vary between manufacturers, which needs to be accommodated during the design procedure.

CHAPTER 3 REACTIVE IMPEDANCE SURFACE

3.1 INTRODUCTION

In this chapter, the design procedures for a square patch RIS and an I-shape RIS are developed. Design equations will be derived for the two RISs, and these design equations will then be used to design a unit cell for each of the two RISs with a centre frequency of 433 MHz, and using the dielectric constant of 4.6 for FR-4. The designed unit cells will then be investigated through the use of parametric studies, where each of the parameters of the unit cells will be modified in turn to observe the effects that these modifications have on the reflection coefficient of the unit cells.

3.2 RIS UNIT CELL DESIGN

As design equations are not readily available for either the square patch RIS or the I-Shape RIS, the goal of this section was to derive such design equations. The design equations were found theoretically through the simulation of a single unit cell of each of the different RISs. The design parameters for the unit cells were expressed as functions of wavelength and dielectric constant and then adjusted until the resulting design gave results that were independent of dielectric constant and scaled well with frequency. The unit cells are then optimised to give a reflection coefficient phase of 0°, which is used as a starting point when the unit cell is used to form an RIS. When the resulting RIS is used as a reflector for an antenna the reflection coefficient phase of the RIS will be modified to optimise the performance of the integrated antenna.

3.2.1 Square patch RIS

The square patch RIS from [14] was recreated in CST Microwave Studio 2014, the 3D EM simulation software suite. The unit cell, shown in Figure 3.1, was simulated as an infinitely repeating structure by implementing perfect infinite magnetic boundaries in the YZ-plane, and perfect infinite electric boundaries in the XZ-plane. The unit cell's response was measured by illuminating the unit cell with a plane wave in the negative Z direction and measuring the reflected wave to find the reflection coefficient.

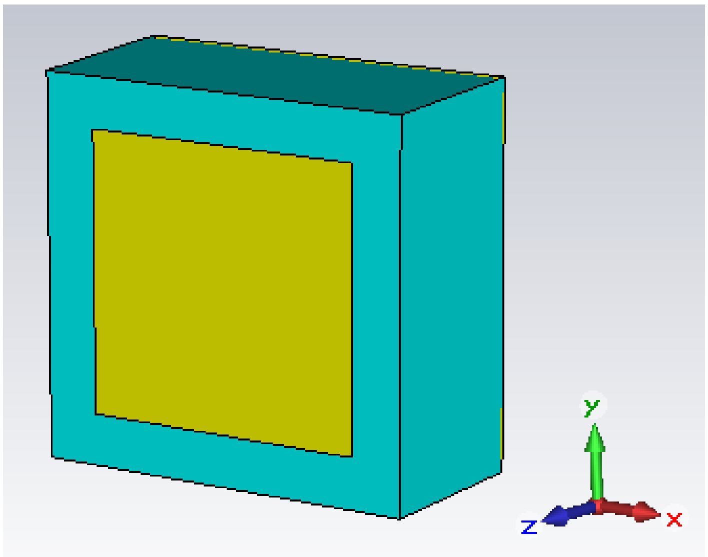

Figure 3.1. Square patch RIS unit cell.

The unit cell was then modified in such a way as to make it easily scalable for different frequencies and different dielectric constants. This was done by altering the design parameters until they can be defined as a fraction of the wavelength in the appropriate medium. Below Equation (3.1) is used to find the wavelength in free space (λ_0) and Equation (3.2) is used to find the wavelength in a medium (λ) [64]. Equations (3.3) to (3.6) below were derived through simulated investigation.

$$\lambda_0 = \frac{c}{f_c} \tag{3.1}$$

$$\lambda = \frac{\lambda_0}{\sqrt{\varepsilon_r}} \tag{3.2}$$

$$L = \frac{\lambda}{4} \tag{3.3}$$

$$g = \frac{\lambda}{11} \tag{3.4}$$

$$h = \frac{\lambda}{6} \tag{3.5}$$

$$d = \frac{\lambda_0}{50} \tag{3.6}$$

Equation (3.3) is used to calculate the length (L) of sides of the square patches. Equation (3.4) is used to calculate the spacing (g) between square patches. Equation (3.5) is used to calculate the height (h) of the RIS. Equation (3.6) is used to calculate the distance (d) between the top of the RIS and the bottom of the reference plane, which is where the antenna will be placed later. The variables used in the equations above are indicated in Figure 3.2 below.

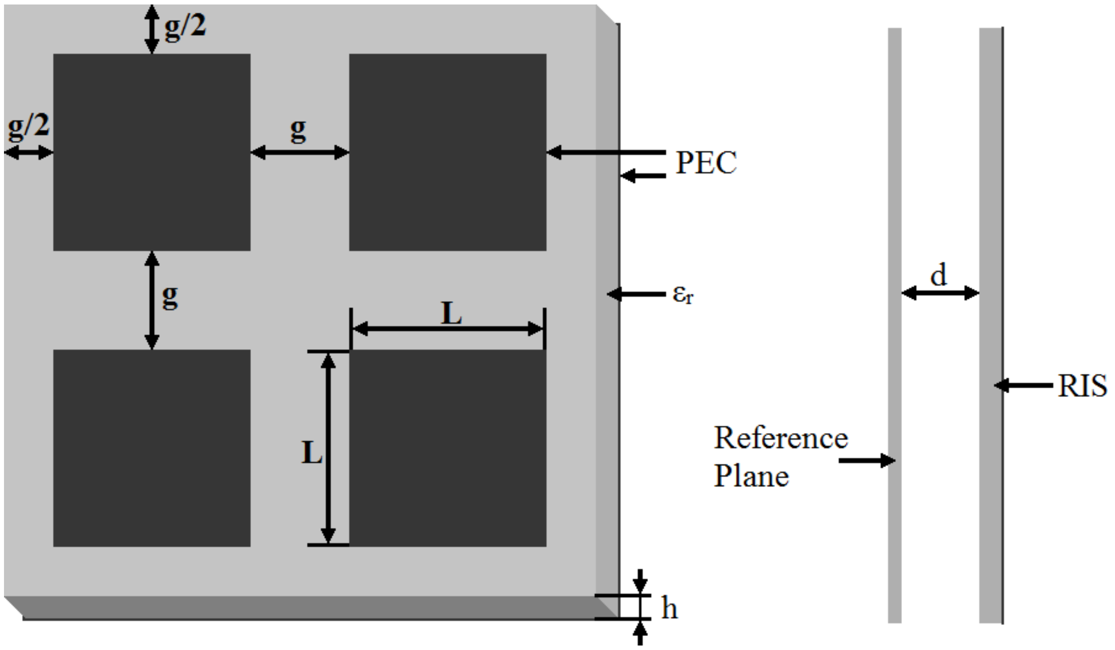

(a) (b)

Figure 3.2. Square patch RIS with design parameters indicated. (a) RIS alone. (b) Side view indicating the reference plane.

The model defined by Equations (3.1) to (3.6) was tested with a parametric sweep of the dielectric constant at a constant centre frequency of 2 GHz, based on the designs presented in [14], and the results are displayed in Figure 3.3. It can clearly be observed in Figure 3.3 that the centre frequency of the model remains constant when the dielectric constant changes, because even if the magnitude of the reflection coefficient changes, the centre of the dip in the reflection coefficient remains constant.

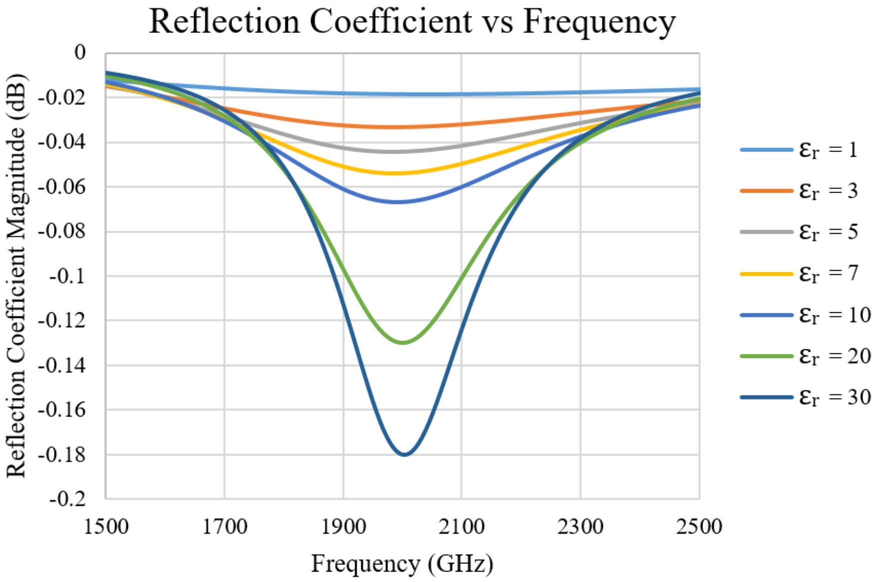

Figure 3.3. Dielectric constant parametric sweep.

The model was also tested against variations in the design centre frequency (f_c), this time with a constant dielectric constant of 50. A dielectric constant of 50 was chosen to ensure that the change in reflection coefficient magnitude can be seen for all of the plot lines. The results displayed in Figure 3.4 below, demonstrates clearly that the model can be accurately adjusted for different design frequencies within 5 % of the intended centre frequency.

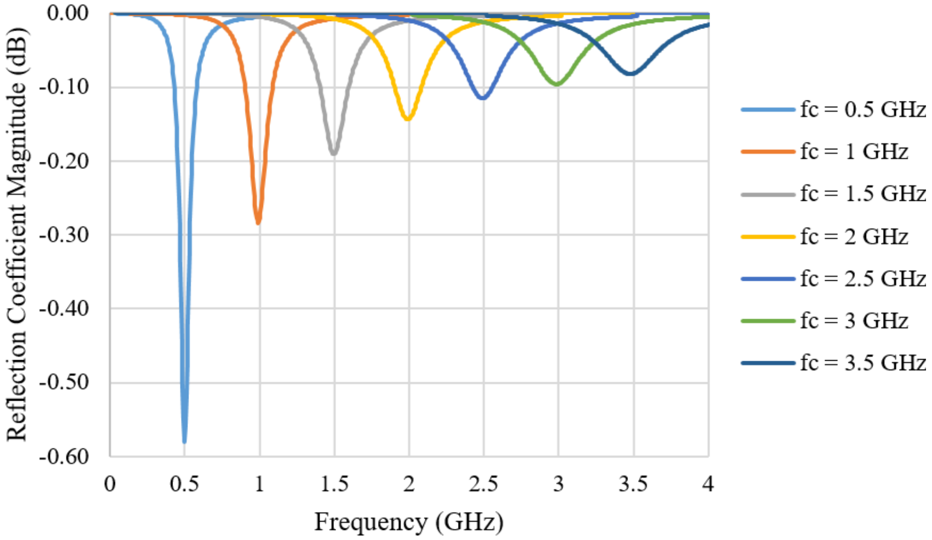

Figure 3.4. Centre frequency parametric sweep.

Finally, Equations (3.1) to (3.6) were used to design a square patch RIS model for 433 MHz with a dielectric constant of 4.6. The model was then optimised to have a reflection coefficient phase of 0° at 433 MHz, as shown in Figure 3.5 below. The optimised parameters are presented in Table 3.1.

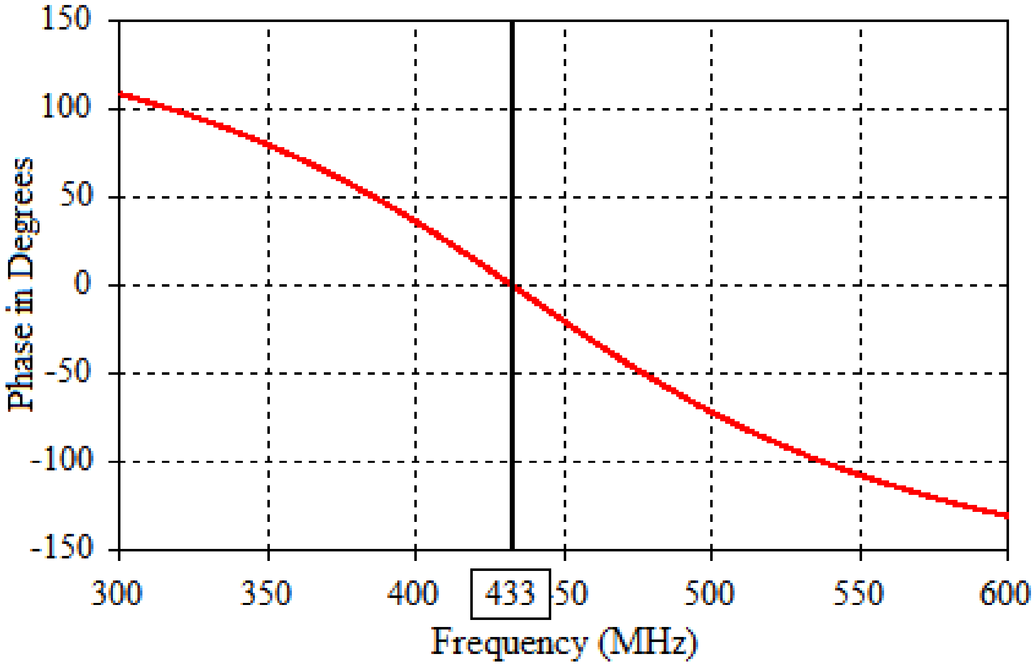

Figure 3.5. Reflection coefficient phase.

Table 3.1. Square patch RIS design parameter values at 433 MHz.

Parameter	Value	Electrical length
Centre frequency (f_c)	433 MHz	
Speed of light (c)	299792458 m/s	
Dielectric constant (ε_r)	4.6	
Wavelength in free space (λ_0)	692.36 mm	
Wavelength in dielectric (λ)	322.82 mm	
Square side length (L)	80.7 mm	0.250 λ
Space between squares (g)	41 mm	0.127 λ
Height of dielectric (h)	53.8 mm	0.167 λ
Distance to antenna (d)	13.85 mm	0.020 λ_0

3.2.2 I-shape RIS

The I-shape RIS, also known as the dog bone RIS, from [5] was recreated in CST Microwave Studio, the 3D EM simulation software suite. The unit cell, which is shown in Figure 3.6, was simulated as an infinitely repeating structure by implementing perfect infinite magnetic boundaries in the YZ-plane, and perfect infinite electric boundaries in the XZ-plane. The unit cell's response was measured by illuminating the unit cell with a plane wave in the negative Z direction and measuring the reflected wave to find the reflection coefficient.

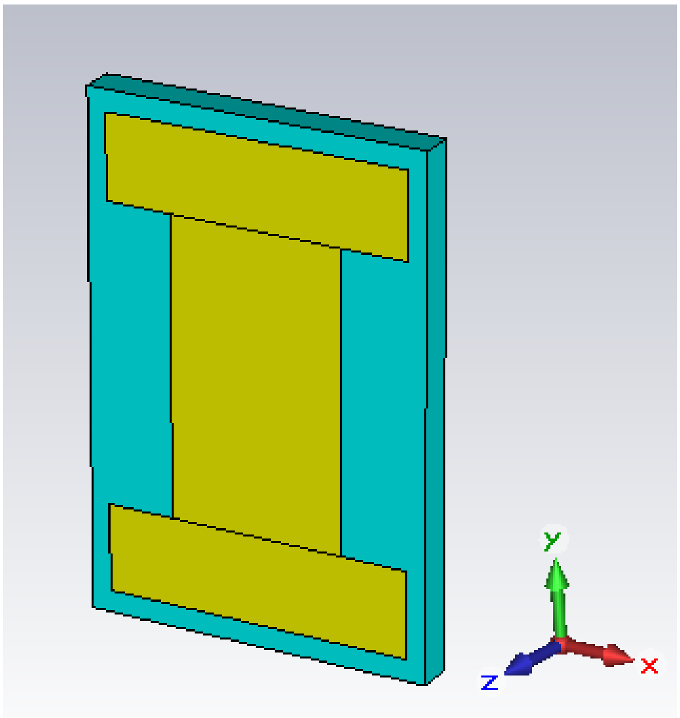

Figure 3.6. I-shape RIS unit cell.

The unit cell was then modified to make it easily scalable for different frequencies and different dielectric constants. This was done by altering the design parameters until they can be defined as a fraction of the wavelength in the appropriate medium. Below Equation (3.1) and Equation (3.2), which are given again for convenience, are used to find the wavelength in free space (λ_0) and the wavelength in a medium (λ) respectively [64]. Equation (3.7) to Equation (3.14) below were derived through simulated investigation, and the parameters used in these equations are indicated in Figure 3.7.

$$\lambda_0 = \frac{c}{f_c} \tag{3.1}$$

$$\lambda = \frac{\lambda_0}{\sqrt{\varepsilon_r}} \tag{3.2}$$

$$L1 = \frac{\lambda}{4} \tag{3.7}$$

$$L2 = \frac{\lambda}{14} \tag{3.8}$$

$$W1 = \frac{\lambda}{7} \tag{3.9}$$

$$W2 = \frac{\lambda}{4} \tag{3.10}$$

$$g1 = \frac{\lambda}{28} \tag{3.11}$$

$$g2 = \frac{\lambda}{32} \tag{3.12}$$

$$h = \frac{\lambda}{35} \tag{3.13}$$

$$d = \frac{\lambda_0}{240} \tag{3.14}$$

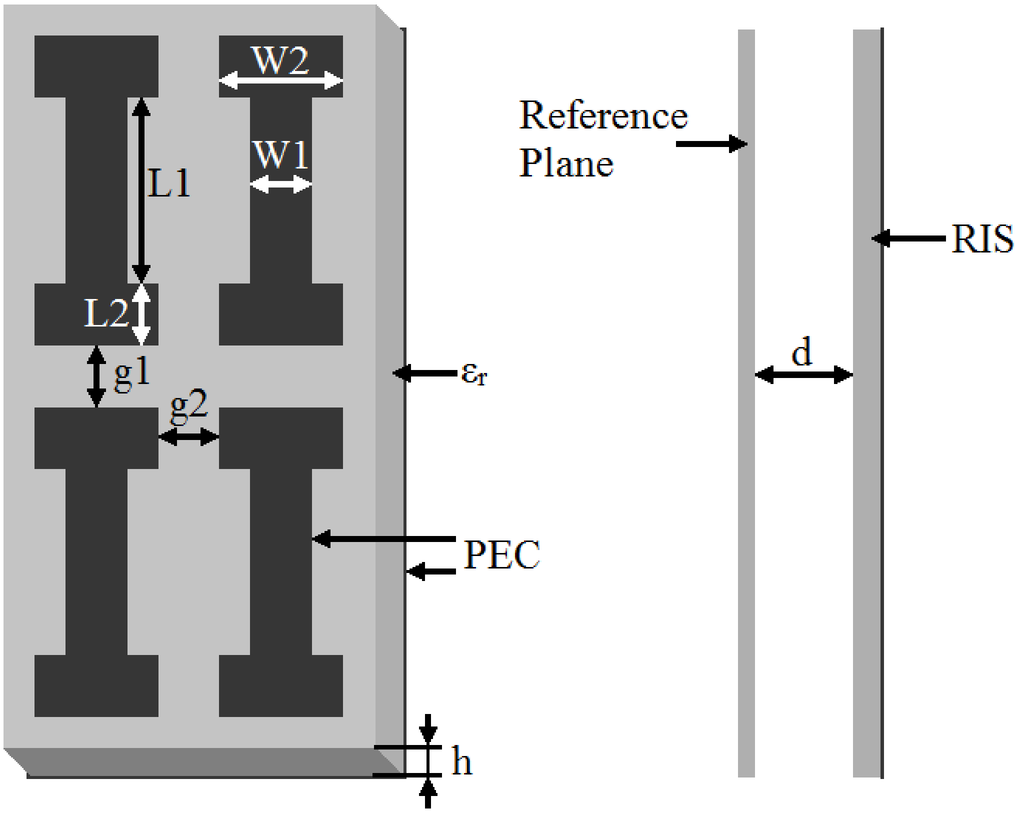

(a) (b)

Figure 3.7. I-shape RIS with design parameters indicated. (a) RIS alone. (b) Side view indicating the reference plane.

The model defined by Equations (3.7) to (3.14) was tested with a parametric sweep of the dielectric constant, at a constant centre frequency of 433 MHz, and the results are displayed in Figure 3.8. It is clearly demonstrated in Figure 3.8 that although the centre frequency of the model increases as the dielectric constant increases, the centre frequency does not vary as much as the dielectric constant. This means that the design equations given above can be used to establish a starting point for optimisation.

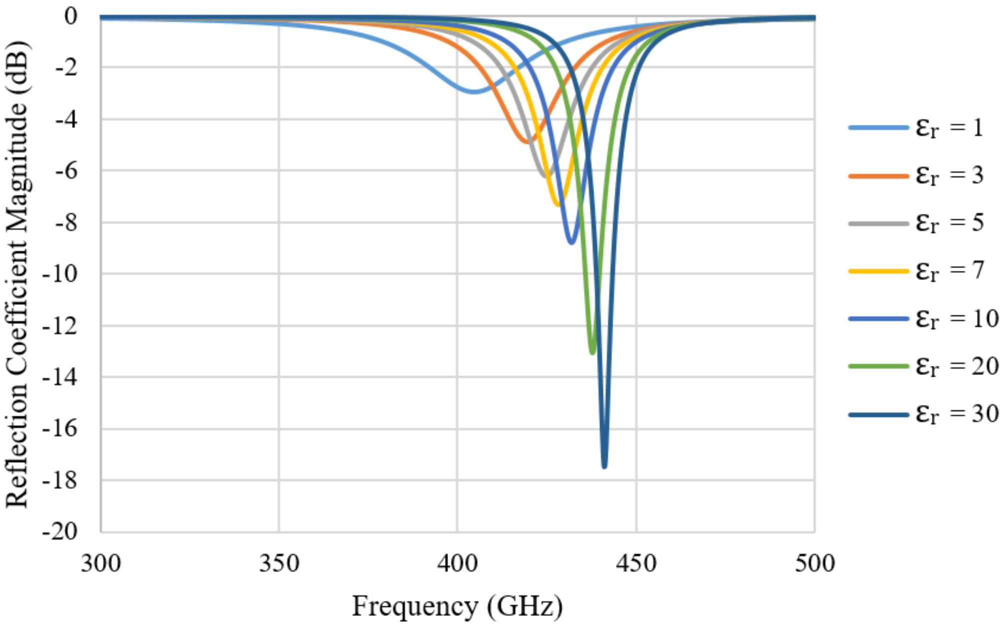

Figure 3.8. Dielectric constant parametric sweep.

The model was also tested against variations in the design centre frequency (f_c), this time with a constant dielectric constant of 50. A dielectric constant of 50 was chosen to ensure that the change in reflection coefficient magnitude can be seen for all of the plot lines. The results displayed in Figure 3.9 below, clearly demonstrate that the model can be accurately adjusted for different design frequencies within 5 % of the intended centre frequency.

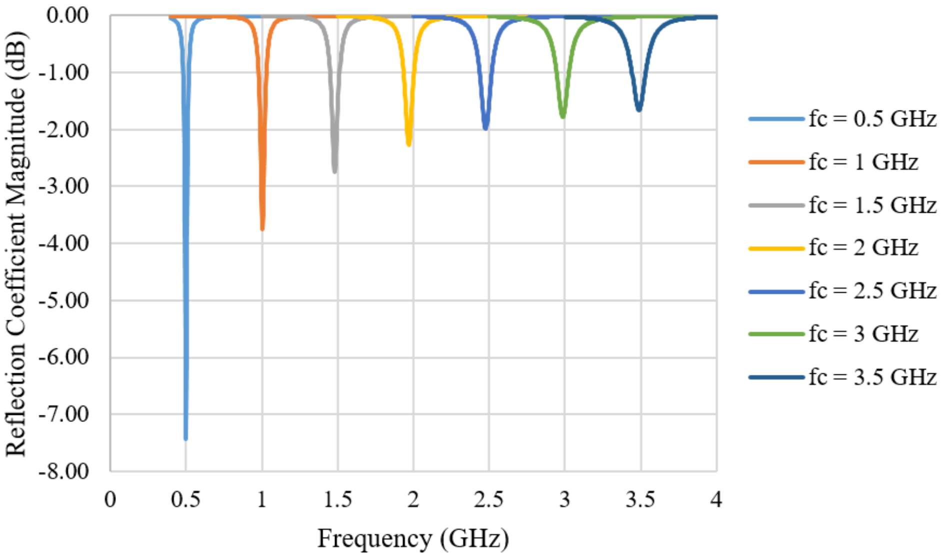

Figure 3.9. Centre frequency parametric sweep.

Finally, Equations (3.7) to (3.14) were used to design an I-shape RIS model with a dielectric constant of 4.6 and a centre frequency of 433 MHz. The optimised parameters are listed in Table 3.2. The model was then optimised to have a reflection coefficient phase of 0° at 433 MHz, as shown in Figure 3.10 below.

Table 3.2. I-shape RIS design parameter values at 433 MHz.

Parameter	Value	Electrical length
Centre frequency (f_c)	433 MHz	
Speed of light (c)	299792458 m/s	
Dielectric constant (ε_r)	4.6	
Wavelength in free space (λ_0)	692.36 mm	
Wavelength in dielectric (λ)	322.82 mm	
Middle length (L1)	79.5 mm	0.246 λ
Top and bottom length (L2)	23.06 mm	0.0714 λ
Middle width (W1)	46.12 mm	0.143 λ
Top and bottom width (W2)	80.7 mm	0.250 λ
Side by side spacing (g1)	11.53 mm	0.0357 λ
Lengthwise spacing (g2)	10.09 mm	0.0313 λ
Height of dielectric (h)	9.22 mm	0.0286 λ
Distance to antenna (d)	2.88 mm	0.00416 λ_0

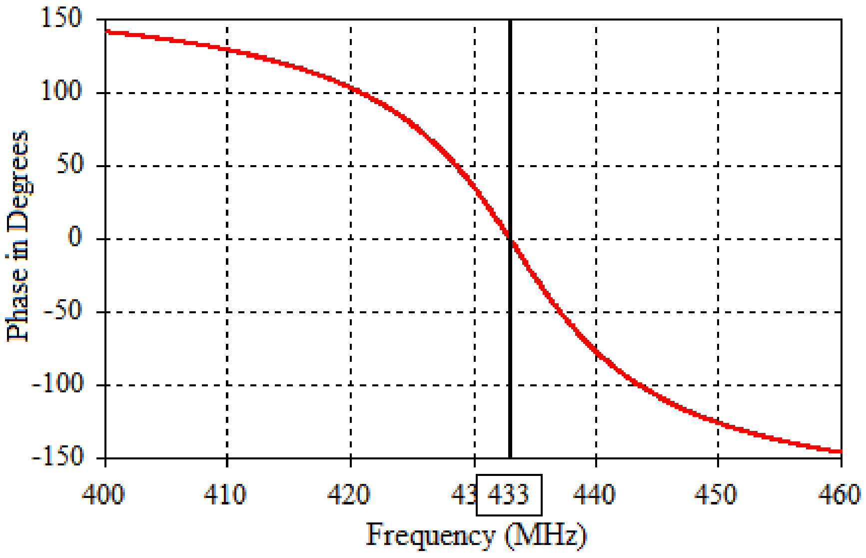

Figure 3.10. Reflection coefficient phase.

3.3 PARAMETRIC STUDY

The parametric studies done on each of the different RISs in this section was done by changing the different design parameters of the simulated unit cells and measuring the reflection coefficient. During the parametric studies the parameters that were not under investigation were kept at the values provided in Table 3.1 and Table 3.2 for the corresponding RIS. For both of the RISs the effect of modifications to the design parameters manifests as a change in the frequency where the phase of the reflection coefficient is 0°, and as a change in the fractional ±90° bandwidth ($FBW_{\pm 90°}$). The $FBW_{\pm 90°}$ is calculated according to Equation (3.15), where f_{-90} is the frequencies where the phase of the reflection coefficient is negative 90°, and f_{+90} is the frequency where the phase of the reflection coefficient is positive 90°. The $FBW_{\pm 90°}$ is used as a performance indicator for RISs as it can be used to gauge the useful bandwidth of an RIS [5].

$$FBW_{\pm 90°} = \frac{2(f_{-90°} - f_{+90°})}{f_{-90°} + f_{+90°}} \tag{3.15}$$

3.3.1 Square patch RIS

The square patch RIS unit cell is very basic as it only has four design parameters that can be used to optimise its performance, which are indicated in Figure 3.2. For a given design frequency, dielectric constant, and loss tangent the only parameters that can be modified are the length (L) of the sides of the squares, the size of the spacing (g) between squares, the height (h) of the dielectric, and the distance (d) between the top of the unit cell and the reference plane where the antenna will be placed.

The results of modifications to the size of the squares are presented in Table 3.3 and the phase of the reflection coefficients for the parameter sweep are displayed in Figure 3.11. From the results below it can be gathered that the centre frequency increases as the size of the square decreases, and that the fractional bandwidth increases with the centre frequency. It should also be noted that the square size should not be modified in isolation, as a 10 % variation in L causes less than a 5 % change in centre frequency.

Table 3.3. Effect of changes in square side length (L).

	Decremented	**Start Point**	**Incremented**
L (mm)	70.83	78.7	86.57
Change in L	-10 %		+10%
f_{+90} (MHz)	348.9	337.5	326.4
f_{-90} (MHz)	559.5	530.1	502.5
$FBW_{\pm 90°}$ (MHz)	46.4 %	44.4 %	42.5%
Change in $FBW_{\pm 90°}$	+4.4 %		-4.3%
f_0 (MHz)	459	438	418.2
f_0 shift	+4.8%		-4.5%

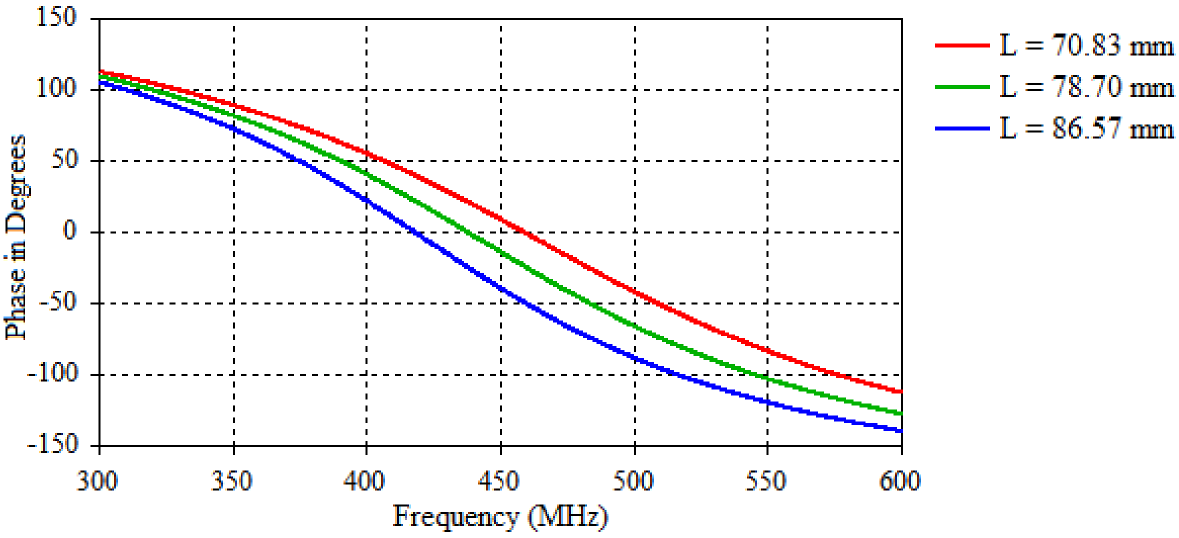

Figure 3.11. Square side length (L) parameter sweep in 10 % increments.

The results of changes in the distance between squares are presented in Table 3.4 and the phase of the reflection coefficients for the parameter sweep are displayed in Figure 3.12. From the results below it can be determined that the centre frequency increases with the distance between squares. In this case the fractional bandwidth also increases with the centre frequency. The distance between squares is not very effective in modifying the centre frequency as a 20 % variation in distance only causes a frequency shift of 4 % or less.

Table 3.4. Effect of changes in distance between squares (g).

	Decremented	Start Point	Incremented
g (mm)	33.6	42	50.4
Change in g	-20 %		+20%
f_{+90} (MHz)	325.2	335.7	344.4
f_{-90} (MHz)	503.4	525	542.4
$FBW_{\pm 90^\circ}$ (MHz)	43.0 %	44.0 %	44.7 %
Change in $FBW_{\pm 90^\circ}$	-2.2 %		+1.5 %
f_0 (MHz)	417.3	434.7	448.8
f_0 shift	-4.0 %		+3.2 %

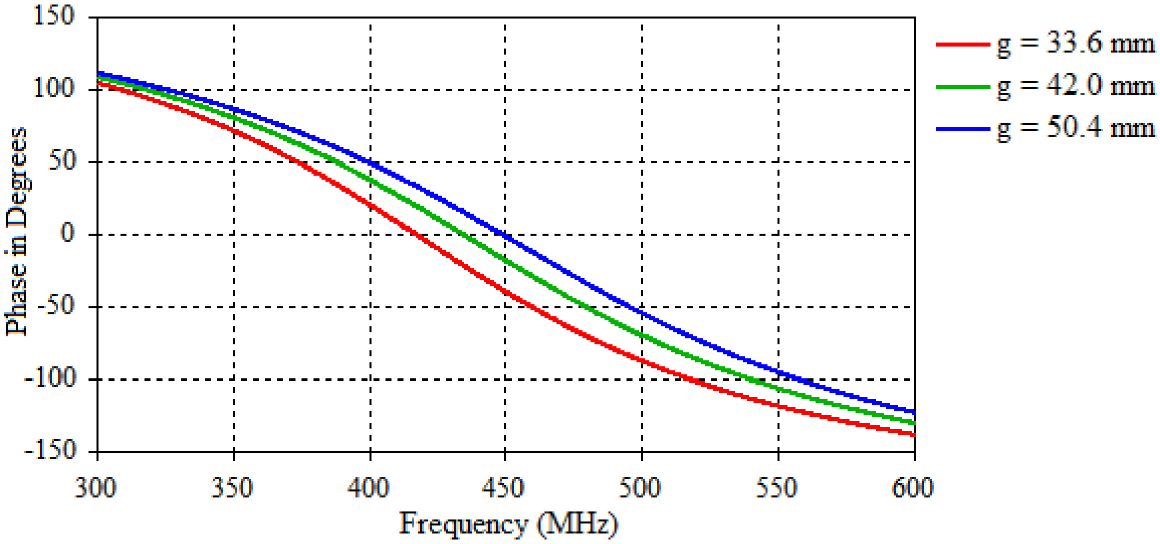

Figure 3.12. Distance (g) between squares parameter sweep in 20 % increments.

The effects of changes to the height of the RIS are presented in Table 3.5 and the phase of the reflection coefficients for the parameter sweep are displayed in Figure 3.13. From the results below it can be seen that increasing the height of the RIS increases the fractional bandwidth, but decreases the centre frequency. For a 10 % variation in height the centre frequency of the RIS shifts by more than 6 %, but the bandwidth only changes by less than 4 %.

Table 3.5. Effect of changes in distance between squares (h).

	Decremented	Start Point	Incremented
h (mm)	48.42	53.8	59.18
Change in h	-10 %		+10%
f_{+90} (MHz)	360.9	334.8	312
f_{-90} (MHz)	553.8	522.9	494.4
$\text{FBW}_{\pm 90^\circ}$ (MHz)	42.2 %	43.9 %	45.2 %
Change in $\text{FBW}_{\pm 90^\circ}$	-3.8 %		+3.1 %
f_0 (MHz)	462.9	432.9	405.9
f_0 shift	+6.9 %		-6.2 %

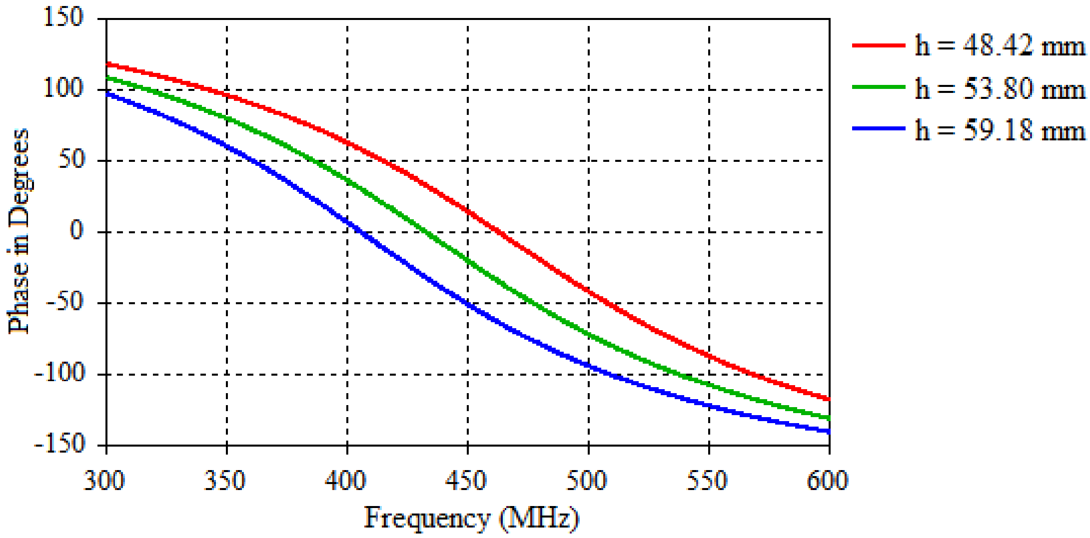

Figure 3.13. RIS height (h) parameter sweep in 10 % increments.

The effects of changes in the distance between the RIS and the reference plane are presented in Table 3.6 and the phase of the reflection coefficients for the parameter sweep are displayed in Figure 3.14. The distance to the reference plane is the distance that the reflected wave travels from the face of the RIS before being measured, which means that the reference plane is at the same distance from the RIS as an antenna would be when used with the RIS. From the results below it can be seen that the distance to the reference plane has a very small effect on the performance of the RIS – a 50 % change had to be made just to cause a noticeable difference. Table 3.6 does however show that increasing the distance to the reference plane does cause an increase in bandwidth, and decreases the centre frequency.

Table 3.6. Effect of changes in distance to the reference plane (d).

	Decremented	**Start Point**	**Incremented**
d (mm)	6.9	13.8	20.7
Change in d	-50 %		+50%
f_{+90} (MHz)	346.5	334.8	324.3
f_{-90} (MHz)	540.9	522.9	508.8
$FBW_{\pm 90^\circ}$ (MHz)	43.8 %	43.9 %	44.3 %
Change in $FBW_{\pm 90^\circ}$	-0.1 %		+0.4 %
f_0 (MHz)	443.4	432.9	424.5
f_0 shift	+2.4 %		-1.9 %

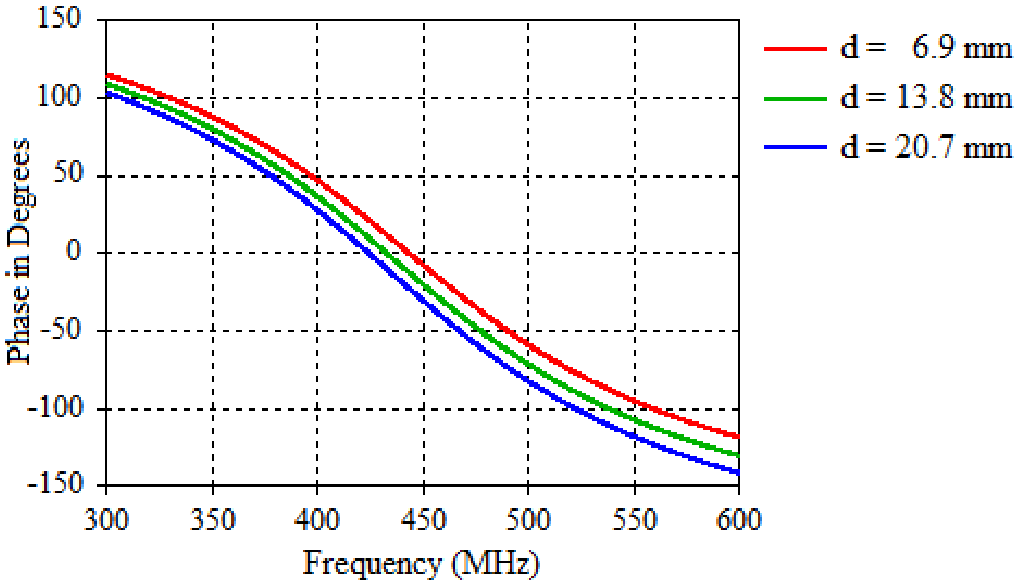

Figure 3.14. Distance to the reference plane (d) parameter sweep in 50 % increments.

The effects of changes in the dielectric constant of the RIS are given in Table 3.7 and the phase of the reflection coefficients for the parameter sweep are displayed in Figure 3.15. The results below show that varying the dielectric constant inversely shifts the centre frequency by almost the same percentage, i.e. a 5 % increase in dielectric constant causes the centre frequency to shift 4.4 % lower. Table 3.7 shows that varying the dielectric constant does not have a pronounced effect on bandwidth, although a 1 % increase in bandwidth could be expected with a 5 % decrease in dielectric constant, and vice versa.

Table 3.7. Effect of changes in dielectric constant (ε_r).

	Decremented	**Start Point**	**Incremented**
ε_r	4.37	4.6	4.83
Change in ε_r	-5 %		+5%
f_{+90} (MHz)	348.5	334.8	323.1
f_{-90} (MHz)	550.8	522.9	499.6
$FBW_{\pm 90°}$ (MHz)	45.0 %	43.9 %	42.9 %
Change in $FBW_{\pm 90°}$	+1.1 %		-1.0 %
f_0 (MHz)	451.9	432.9	413.1
f_0 shift	+4.4 %		-4.6 %

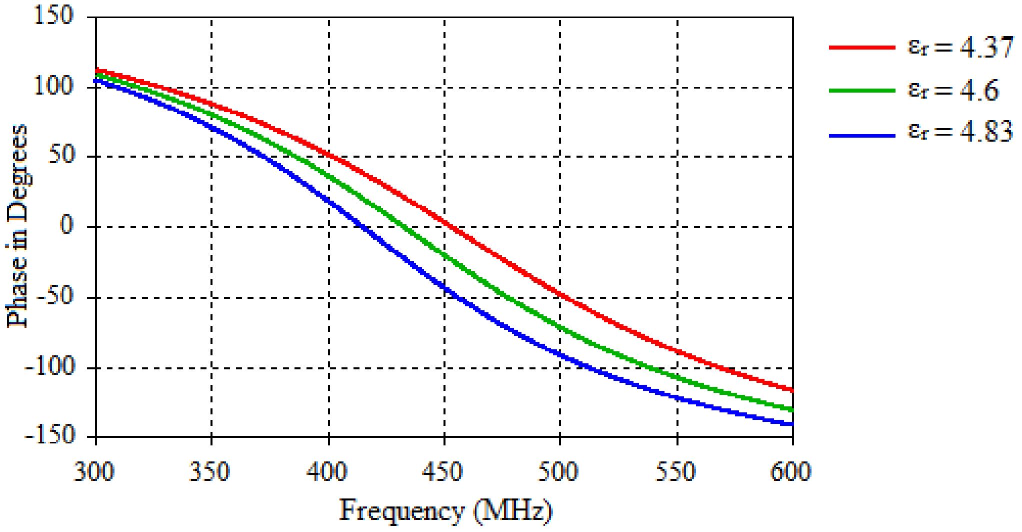

Figure 3.15. Dielectric constant (ε_r) parameter sweep in 50 % increments.

Finally, and most importantly, the effect of losses on the performance of the square patch RIS was investigated. In Figure 3.16 below it is shown that increasing the loss tangent (tan δ in Figure 3.16) decreases the bandwidth of the RIS until a loss tangent of 0.5 is reached, then the RIS becomes unusable. This is desirable because the material that the final antenna will be manufactured from is FR-4, which has a rather high loss tangent. Fortunately, the loss tangent of FR-4 will typically be less than 0.02 over the intended frequency band, which falls into the safe region for the square patch RIS.

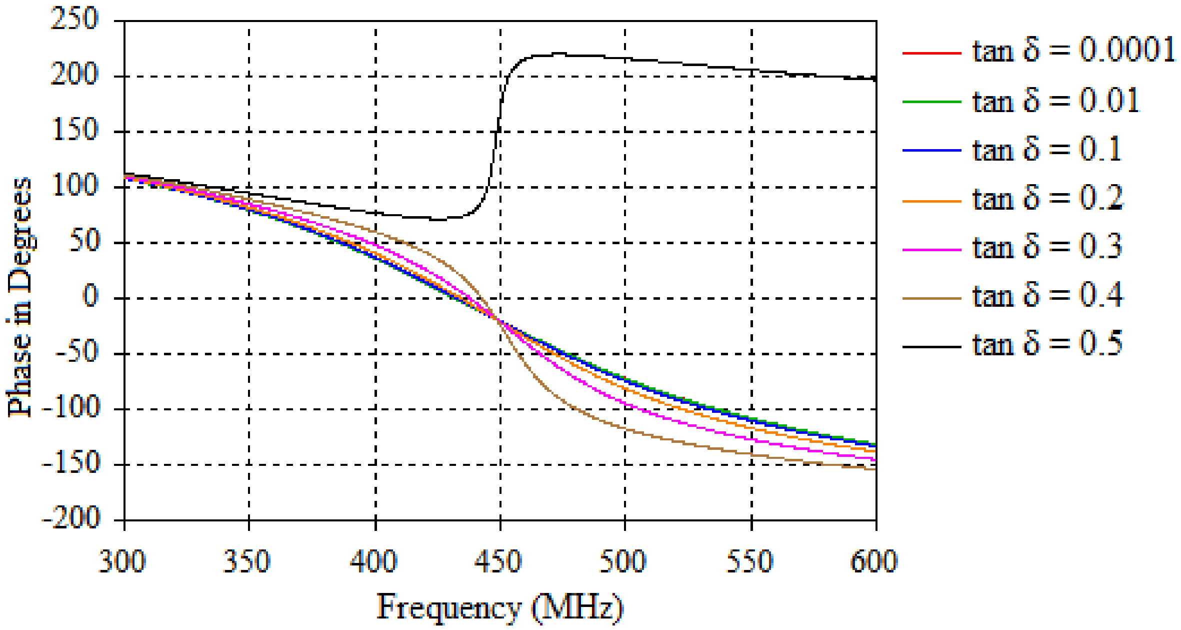

Figure 3.16. Loss tangent (tan δ) parameter sweep.

3.3.2 I-shape RIS

The I-shape RIS is more complex than the square patch RIS inasmuch as it has eight design parameters as opposed to the four design parameters of the square patch RIS. This can complicate the process of tuning the I-shape RIS because modifications in some of the parameters could affect the effectiveness of prior modifications to other parameters. The design parameters of the I-shaped RIS are presented in Figure 3.7.

The most noteworthy of the I-shape RISs design parameters is h, the height of the RIS. The effect of a 10 % modification in height is displayed in Figure 3.17 below. This 10 % modification did not have a large impact on the centre frequency; it caused less than 1 % shift, but it did have a significant impact on the bandwidth which would increase or decrease by more than 13 % if the height of the RIS increased or decreased.

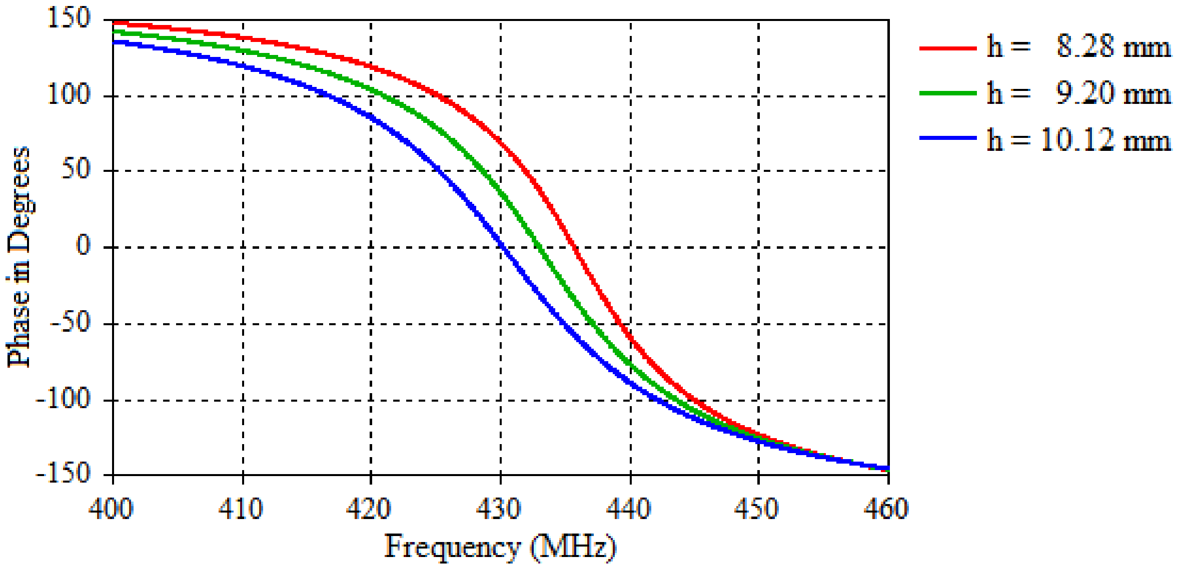

Figure 3.17. RIS height (h) parametric sweep in 10 % increments.

The distance (d) between the I-shape RIS and the reference plane did not have as large an effect as the height of the RIS. The reference plane is where the magnitude and phase of the reflected plane wave is measured with the ultimate goal of placing an antenna at the same distance from the RIS. As shown in Figure 3.18 the effects, resulting from modifications to the height, will decrease as the height increases, up to the point where the reflection coefficient remains relatively constant as the height increases above 6 mm.

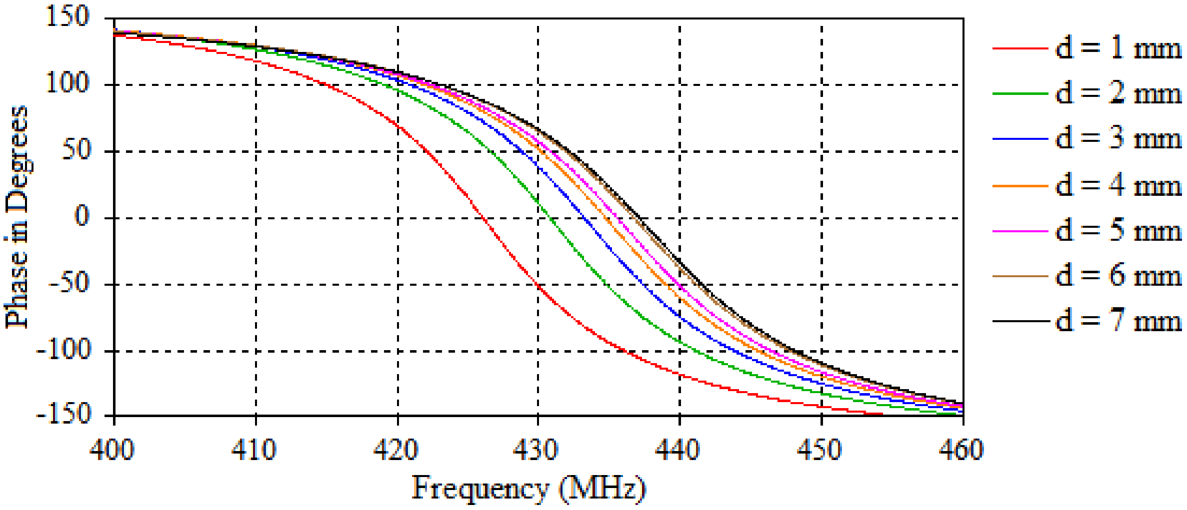

Figure 3.18. Distance to reference plane (d) parameter sweep.

The vertical (g1) and horizontal distance (g2) between the I-shapes also did not have a significant impact on the performance of the RIS. Figure 3.19 shows the effects of a 20 % change in g1. Figure 3.20 shows the effects of a 50 % change in g2. Although a change in performance can be observed, the size of the increments causes it to border on impractical.

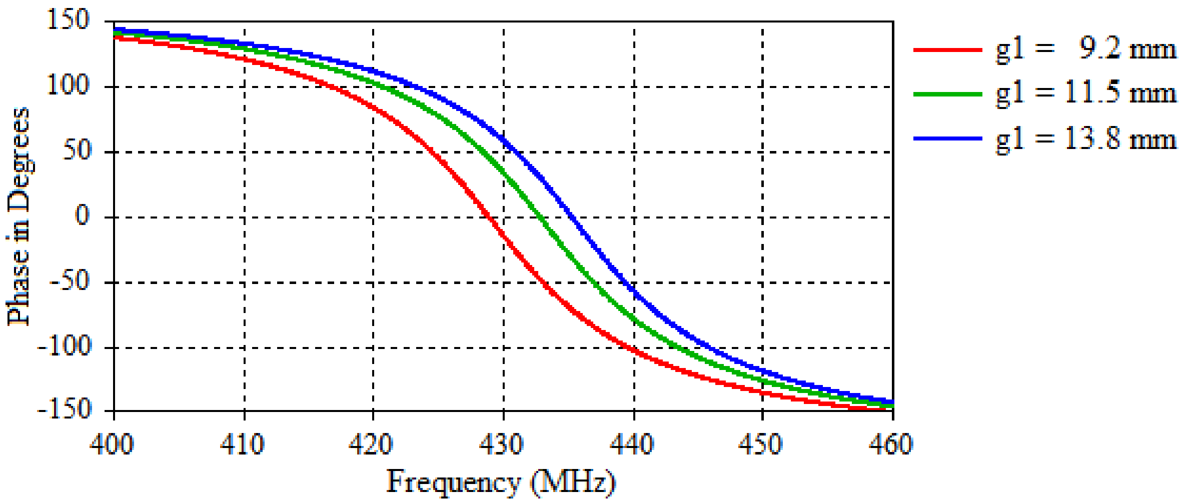

Figure 3.19. Vertical distance between I-shapes (g1) parameter sweep in 20 % increments.

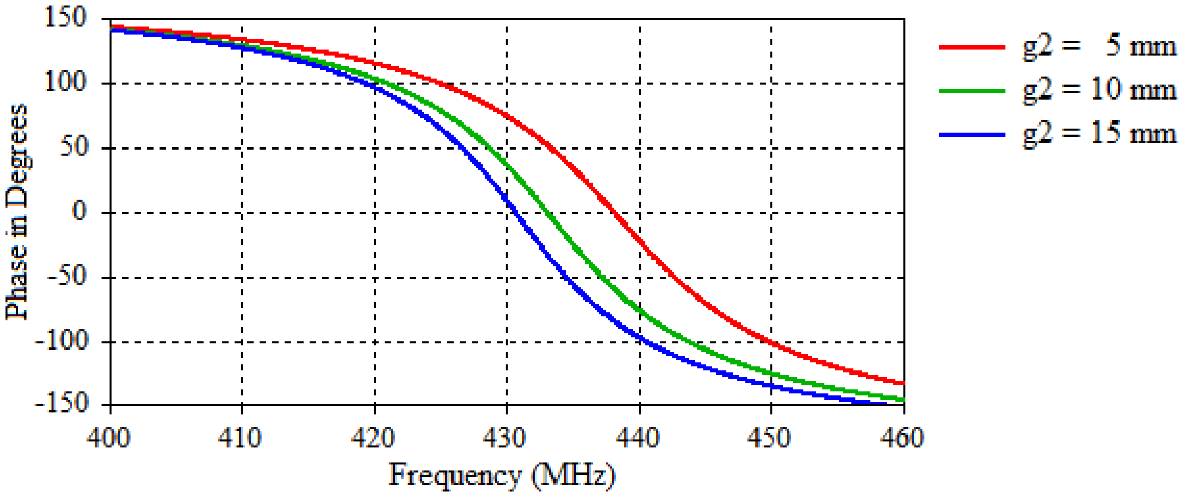

Figure 3.20. Horizontal distance between I-shapes (g2) parameter sweep in 50 % increments.

The width of the I-shape, on the other hand, had a significant impact on the performance of the RIS. A 5 % alteration in either W1 and W2 caused more than a 6 % change in bandwidth, and a change of roughly 2 % in centre frequency. It should be noted that the bandwidth and centre frequency increased as W1 and decreased as W1 decreased. Conversely, the bandwidth and centre frequency decreased as W2 increased, and increased as W2 decreased. The resultant curves from incrementing W1 and W2 are shown below in Figure 3.21 and Figure 3.22 respectively.

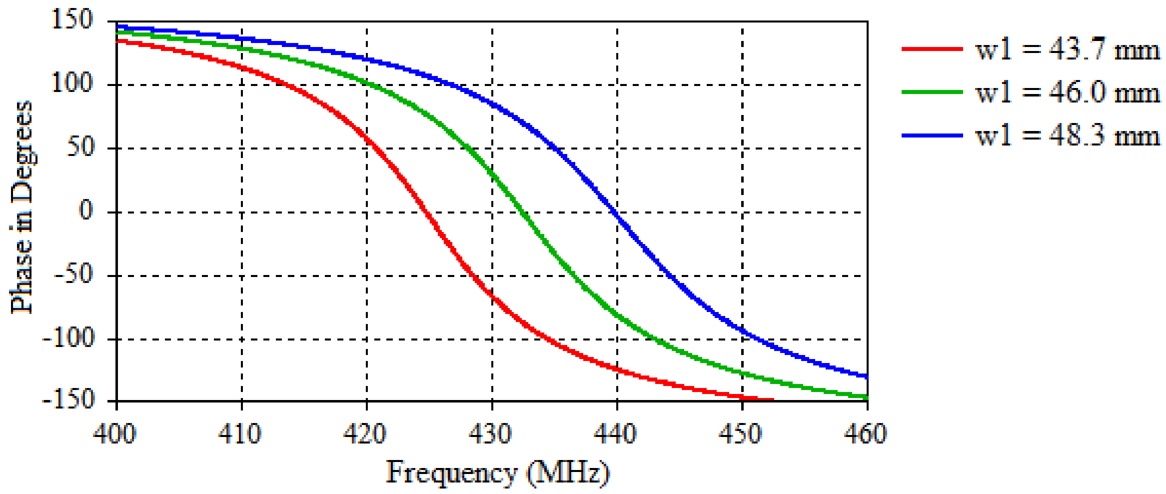

Figure 3.21. W1 parameter sweep in 5 % increments.

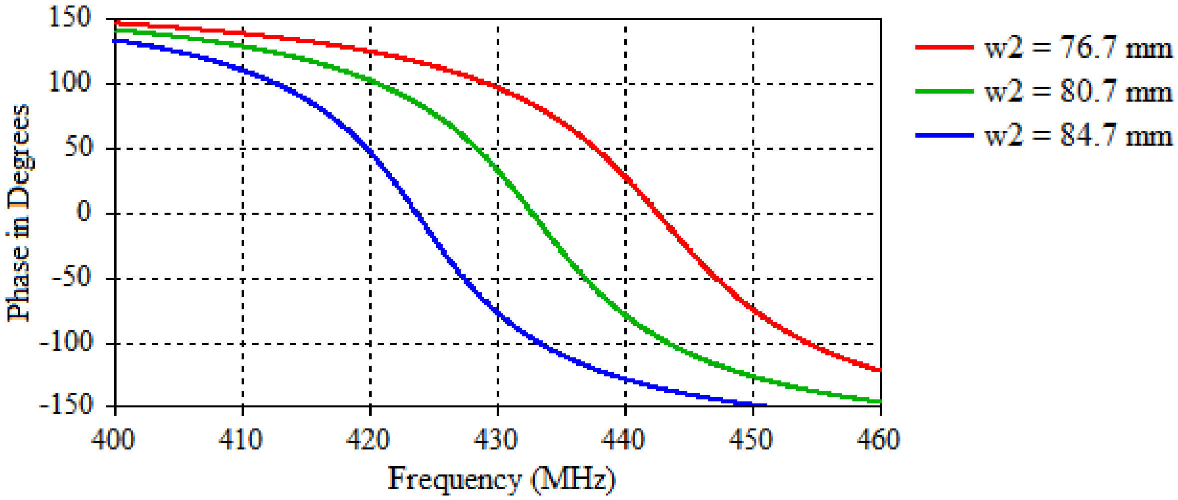

Figure 3.22. W2 parameter sweep in 5 % increments.

Modifications to the length of the I-shape also had a notable effect on the performance of the RIS, but less so than modifications to the width of the I-shape. Increases in either L1 or L2 produced decreases in both bandwidth and centre frequency, as can be seen in Figure

3.23 and Figure 3.24 below. It can also be observed in Figure 3.23 and Figure 3.24 that alterations to L1 have a larger effect than alterations to L2, which is due to the fact that both L1 and L2 contribute to the total length of the I-shape, but as L1 is more than twice as large as L2 this is to be expected.

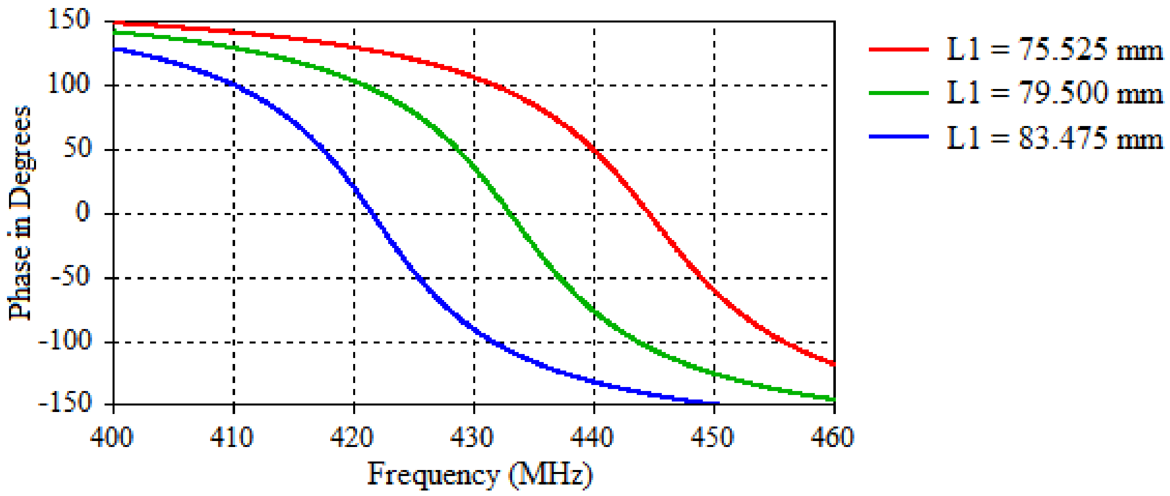

Figure 3.23. L1 parameter sweep in 5 % increments.

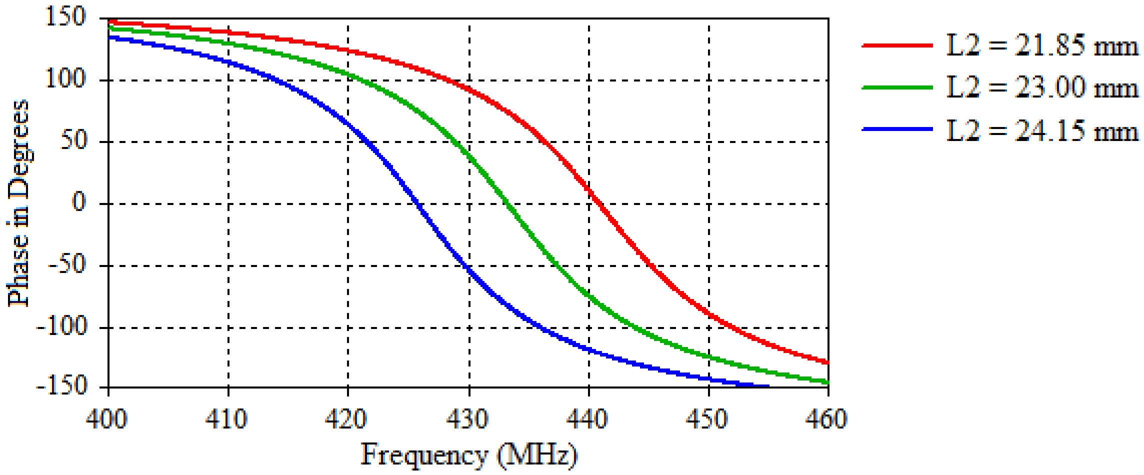

Figure 3.24. L2 parameter sweep in 5 % increments.

Dielectric constant (ε_r) had a pronounced effect on the centre frequency of the I-shape RIS, with a 5 % increase in dielectric constant causing a 2.5 % decrease in centre frequency, and vice versa. Changes in dielectric constant however, effected the I-shape RIS to a lesser extent that the square patch RIS. A 5 % change in dielectric constant caused less than 1 % change in the bandwidth of the I-shape RIS. The dielectric constant parametric sweep for the I-shape RIS is shown in Figure 3.25.

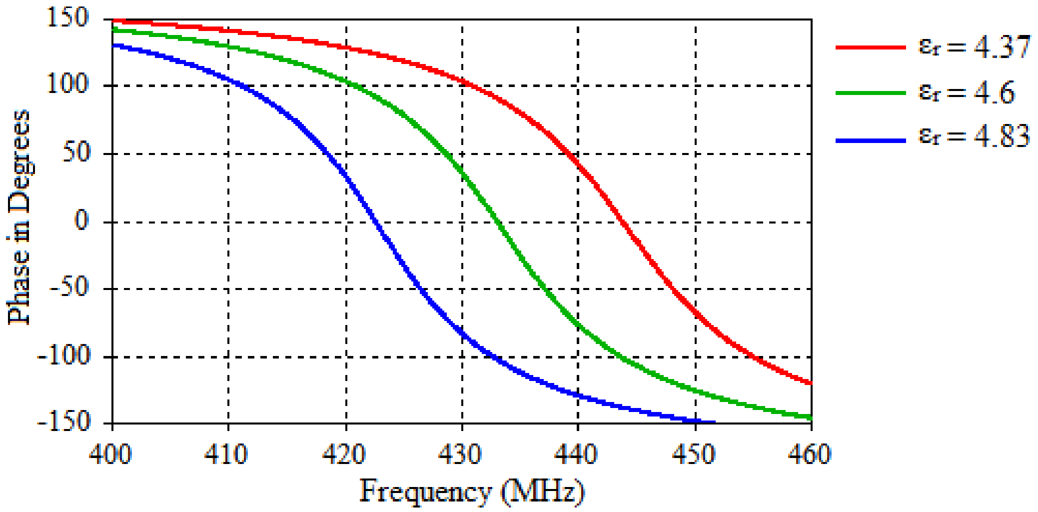

Figure 3.25. Distance to reference plane (ε_r) parameter sweep

Finally, the effect of losses on the performance of the I-shape RIS was investigated. In Figure 3.26 below it is shown that increasing the loss tangent (“tan δ” in Figure 3.26) decreases the bandwidth of the RIS until a loss tangent of 0.004 is reached, then the RIS becomes unusable. This is troubling because the material that the final antenna will be manufactured from is FR-4, which has a loss tangent that is larger than 0.01 at the design frequency.

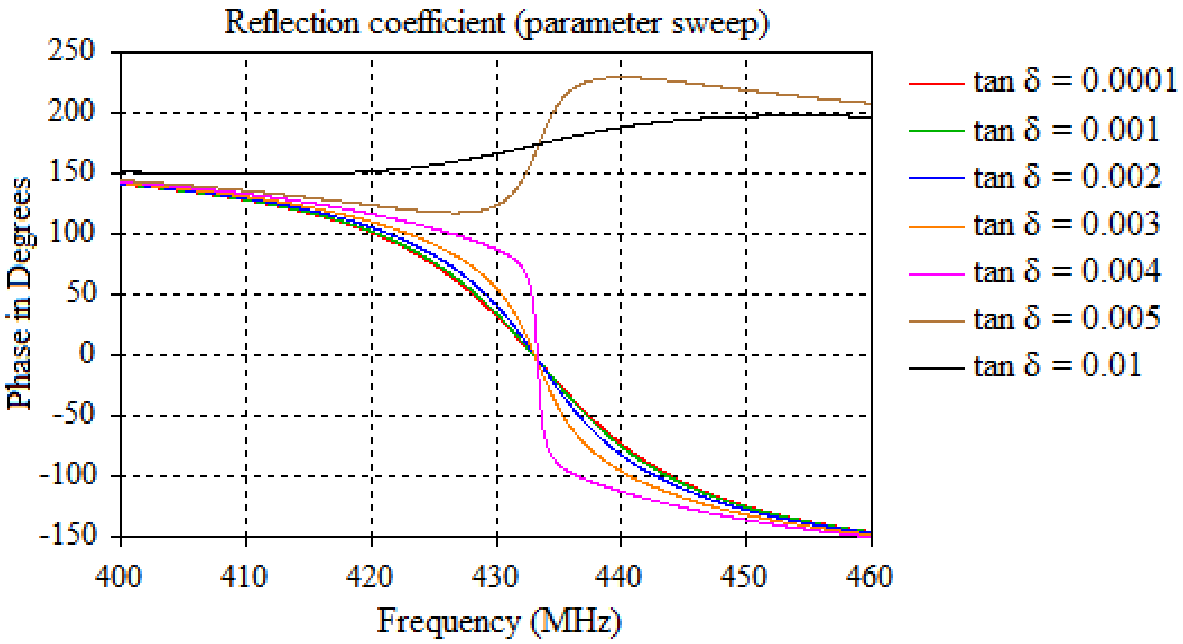

Figure 3.26. Loss tangent (tan δ) parameter sweep.

3.4 RIS UNIT CELL COMPARISON

The fundamental difference between the square patch RIS and the I-shape RIS is that the latter has a slightly more complex design, with more degrees of freedom, than the former. In and of itself the increase in degrees of freedom that the I-shape RIS supplies does not make a significant difference in this application. The more basic design of the square patch RIS has the benefit of being easier to work with. It would be easier to customise the square patch RIS than the I-shape RIS, as it has fewer variables that need to be varied to optimize a design.

The big difference between that was found between the square patch RIS and the I-shape RIS was that the former was less sensitive than the latter to the loss tangent of the dielectric medium that was used. There could be various reasons for this, and it could be possible to optimise the I-shape RIS to perform better in lossy materials, but the square patch RIS was found to have sufficient performance for this application as is. The acceptable performance and low complexity lead to the square patch RIS being chosen above the I-shape RIS for this application.

3.5 SUMMARY

An investigation was done into the design of the square patch RIS and I-shape RIS unit cells. Design equations were derived and used to design unit cells that operate at 433 MHz using a dielectric medium with a dielectric constant of 4.6. The two unit cells were optimised to have a 0° reflection coefficient phase at 433 MHz. The optimised unit cells were then investigated through parametric studies to find the degree to which each of the RISs are customisable.

The square patch RIS is less complex than the I-shape RIS with only four design parameters as opposed to the eight design parameters of the I-shape RIS. It was found that even though the I-shape RIS has more degrees of freedom than the square patch RIS, the square patch RIS was sufficiently customisable for the intended application. The added complexity of the I-shape RIS did not provide the required increase in performance for it to be chosen above the square patch RIS. The I-shape RIS also proved to be more sensitive to changes in material loss tangent than the square patch RIS. In the end the square patch RIS was chosen as the RIS that was used in this study due to its lower sensitivity to changes in material loss tangent, acceptable performance, and low complexity.

CHAPTER 4 INTEGRATED ANTENNA AND RIS

4.1 INTRODUCTION

In this chapter, a planar monopole antenna was designed and integrated with a 2 by 2 RIS based on the square patch RIS unit cell developed in Chapter 3. The antenna was then first optimised to be as compact as possible, whilst maintaining passable performance, and then it was optimised for performance. Investigation was also done into the effects of the material loss tangent, and human loading on antenna performance.

4.2 PLANAR MONOPOLE ANTENNA DESIGN

The planar monopole antenna was designed according to Equations (4.1) to (4.3) from [61], where Wg is the width of the ground, Lg is the length of the ground, and La is the length of the antenna, as can be seen in Figure 4.1. λ and λ_0 were defined in Equations (3.1) and (3.2).

$$W_g = 0.34\lambda \tag{4.1}$$

$$L_g = 0.154\lambda \tag{4.2}$$

$$L_a = 0.15\lambda_0 + L_g \tag{4.3}$$

The antenna was then optimised to resonate at 433 MHz on FR-4, using a dielectric constant of 4.6 and a loss tangent of 0.02 as found in [65]. The optimised design values are listed in Table 4.1, and the optimised antenna is shown in Figure 4.1.

Table 4.1. Planar monopole design parameter values at 433 MHz.

Parameter	**Value**
Centre frequency (f_c)	433 MHz
Loss tangent (tan δ)	0.02
Dielectric constant (ε_r)	4.6
Wavelength in free space (λ_0)	692.36 mm
Wavelength in dielectric (λ)	322.82 mm
Antenna length (La)	212.9 mm
Antenna width (Wa)	3 mm
Ground length (Lg)	45 mm
Ground width / Substrate width (Wg)	109.76 mm
Substrate length (Ls)	250 mm
Substrate thickness	1.6 mm

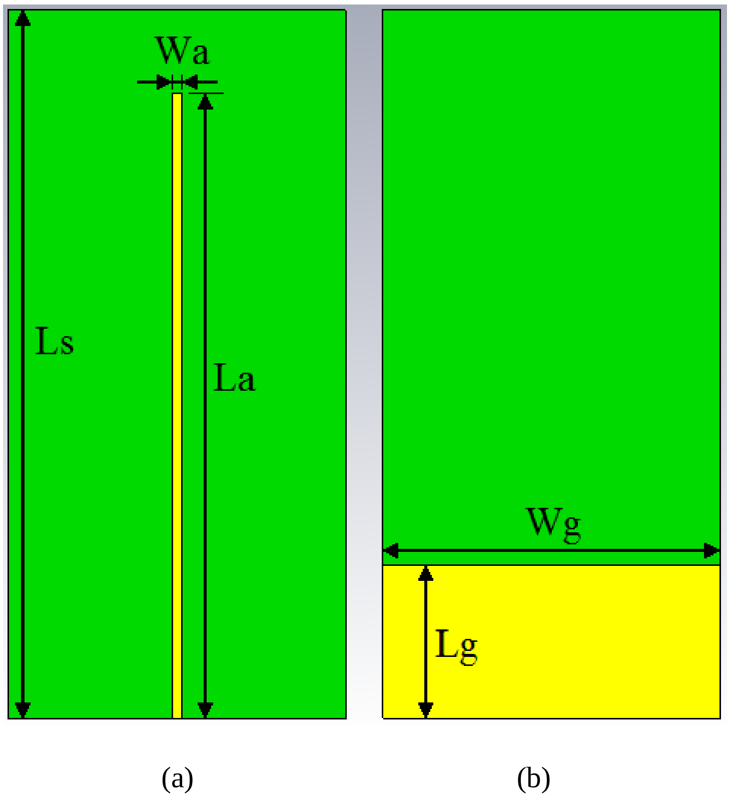

Figure 4.1. Planar monopole antenna. (a) Top view. (b) Bottom view.

The impedance bandwidth of the optimised planar monopole antenna was 9.2 %, based on the reflection coefficient shown in Figure 4.2.

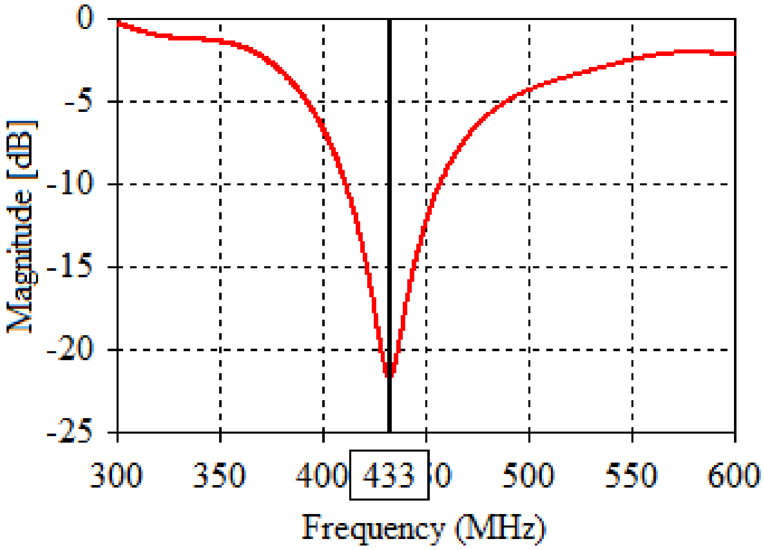

Figure 4.2. Optimised planar monopole reflection coefficient.

The E- and H-plane co-polarization far field patterns of the optimised planar monopole antenna are shown in Figure 4.3 below, where it can be seen that the H-plane far field pattern is omnidirectional, and the E-plane far field pattern bidirectional. The maximum realised gain for this antenna is 1.8 dBi, the H-plane pattern has a ripple that is smaller than 0.2 dB, and in the E-plane the 3 dB beamwidth in both the 0° and 180° directions is in excess of 80°.

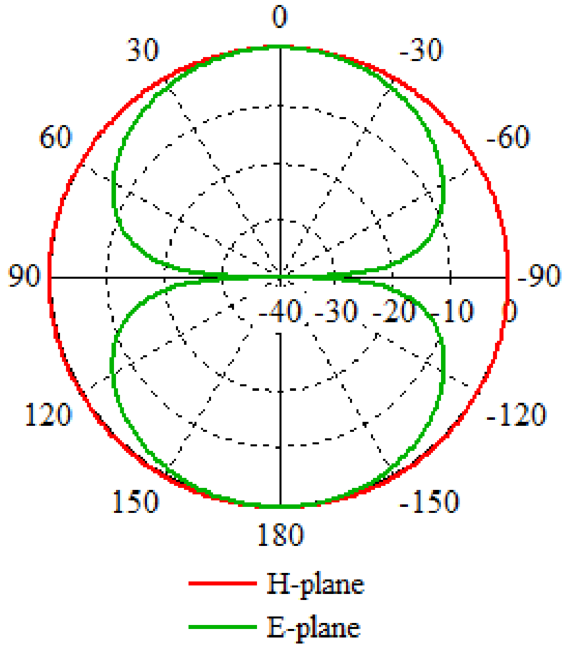

Figure 4.3. Planar monopole antenna normalised E- and H-plane farfield patterns.

4.3 INTEGRATED ANTENNA DESIGN

The planar monopole antenna was integrated with a 2 by 2 square patch RIS with the parameters developed in chapter 3. The integrated antenna is displayed in Figure 4.4 below. The change to the radiation pattern due to the addition of the RIS is shown in Figure 4.5, where it can be observed that the addition of the RIS has transformed the farfield pattern from bidirectional to directional. Due to the addition of the RIS the gain of the antenna has increased from 1.8 dBi to 3.9 dBi.

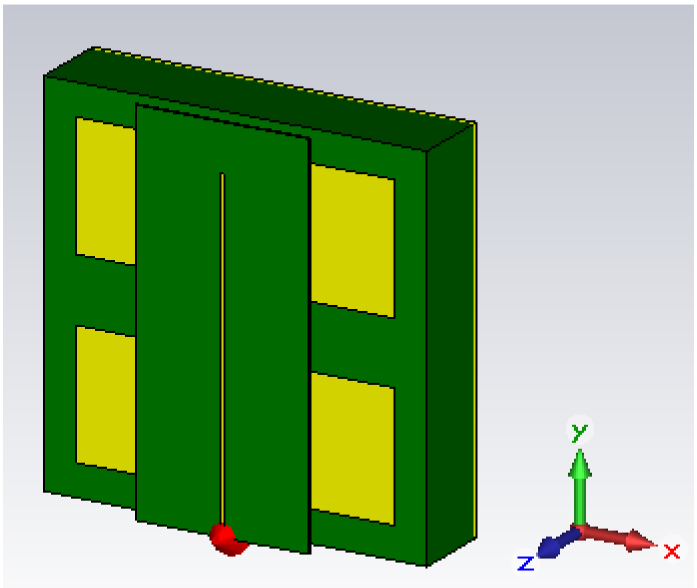

Figure 4.4. Initial simulation model for the integrated planar monopole and RIS.

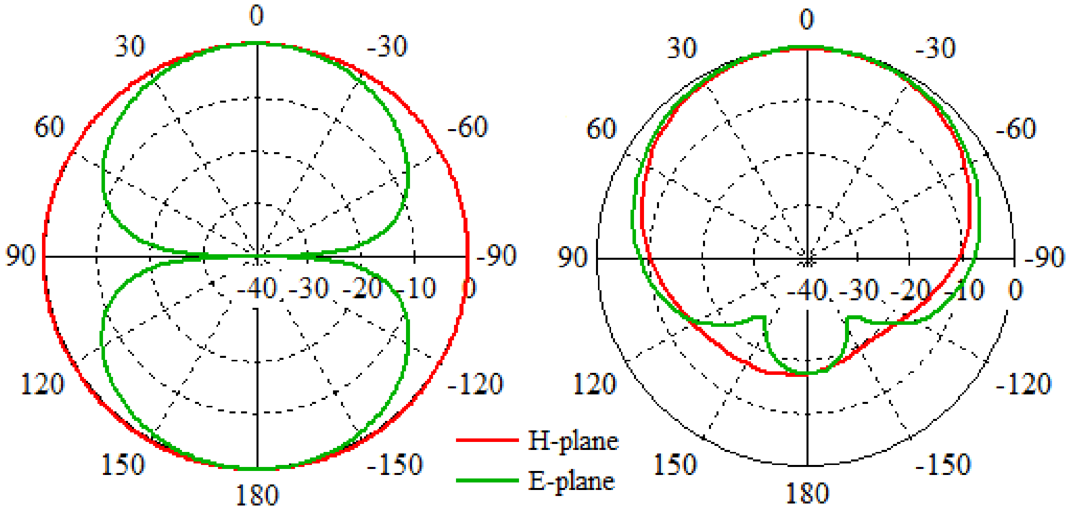

(a) (b)

Figure 4.5. Normalised E- and H-plane far field radiation patterns of (a) the planar monopole antenna, and (b) the integrated planar monopole and RIS.

Various performance indicators for the integrated antenna are presented in Figure 4.6 below. Figure 4.6 (a) shows that the reflection coefficient is above -10 dB in the operating band, but can be improved through optimisation. Figure 4.6 (b) shows a wide band where more than 3.5 dBi gain is achieved, and Figure 4.6 (c) and Figure 4.6(d) show that the antenna's radiation pattern is directional over a relatively wide band.

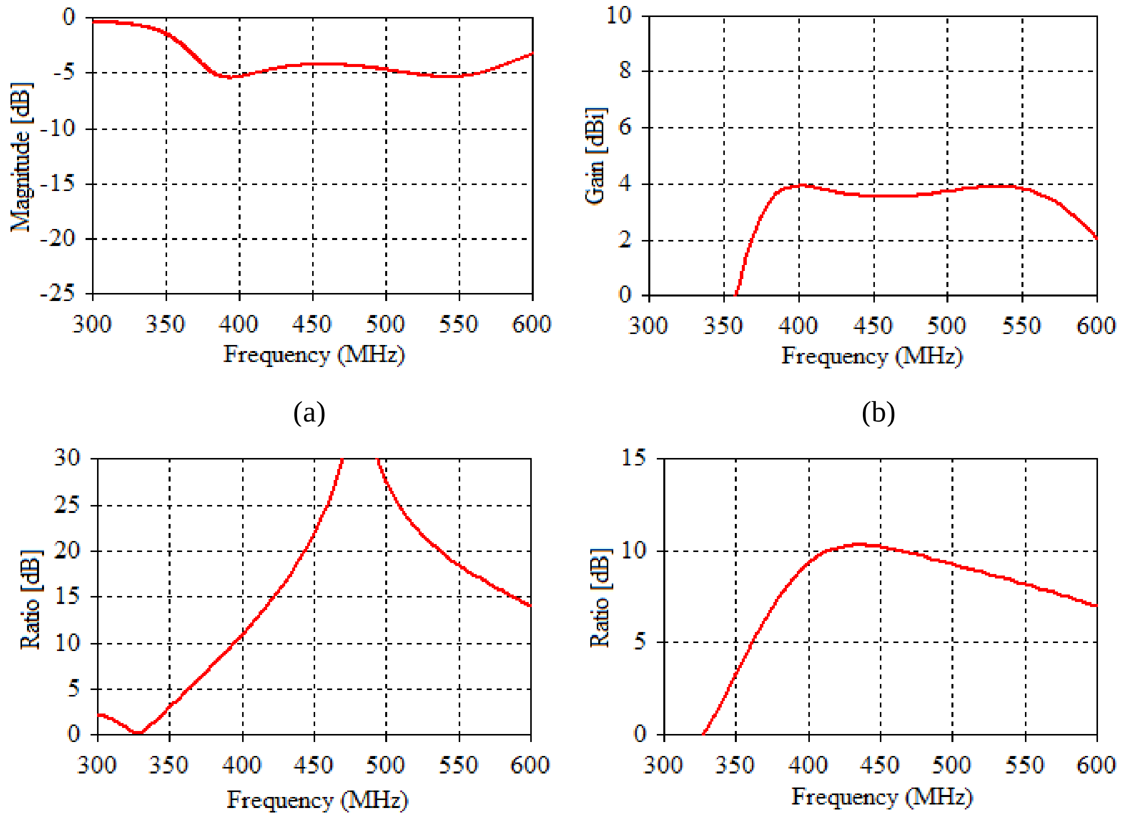

(a) (b)

(c) (d)

Figure 4.6. Integrated antenna performance. (a) Reflection coefficient. (b) Realised gain. (c) Front to back ratio. (d) Front hemisphere to rear hemisphere radiated power ratio.

4.4 OPTIMISE FOR PERFORMANCE

The antenna was first optimised for optimal performance. For this stage of the investigation, very lenient width and length goals were specified. In this section the design goals are given for an antenna with optimal performance, and the final design is discussed.

4.4.1 Design goals

For this stage of the investigation the optimal performance for a planar monopole with a 2 by 2 square RIS reflector was found. The design goals that were used are listed in Table 4.2. Due to the fact that the antenna design process was part of an investigation into what is achievable with inexpensive high loss materials, a set of design goals were followed instead of design specifications. An RIS thickness of 38.4 mm, and an antenna substrate thickness of 1.6 mm was used to minimise costs.

Table 4.2. Design goals for the standard planar monopole antenna.

Goal Title	Goal Description
Integrated antenna width and length	Smaller than 0.5 λ
Integrated antenna height	Smaller than 0.25 λ
Integrated antenna substrate	FR-4
Antenna substrate height	1.6 mm
RIS height	38.4 mm
Input impedance	50 Ω
Centre frequency	433 MHz
Impedance bandwidth	A reflection coefficient of -10 dB over a bandwidth of least 20 %.
Gain	At least 5 dBi over at least 75 % of the impedance bandwidth
Front to back ratio	20 dB over at least 50 % of the impedance bandwidth
Ratio between power radiated in the front and rear hemispheres	At least 6 dB over the 90 % of the impedance bandwidth.
Radiation efficiency	At least 80 % over the entire impedance bandwidth.

4.4.2 Design procedure

The simulation model of the standard planar monopole antenna is shown in Figure 4.7. The design procedure for the standard planar monopole antenna was developed based on the parametric studies done in Chapter 3, and during the process of designing the standard planar monopole antenna for 433 MHz. The design procedure that was developed for maximum performance is as follows:

- Design the RIS unit cell according to Equations (3.3) to (3.6).
- Design a planar monopole antenna according to Equations (4.1) to (4.3).
- Integrate the planar monopole and a two by two unit cell RIS, by placing the monopole at the RIS reference plane calculated with Equation (3.6).
- Reduce the thickness of the RIS by 30 %.
- Reduce the distance between square RIS patches by 50 %.
- Increase the size of the square RIS patches by 50 %
- Change the length of the antenna ground plane to be 25 % of length of the RIS.
- Optimise to further improve the reflection coefficient, gain, and front to back ratio as needed.

The design parameter values for the standard planar monopole antenna, according to the design procedure, are listed in Table 4.3, and design parameters are indicated in Figure 4.8. This design should be used as a starting point before optimising the antenna to fine tune performance.

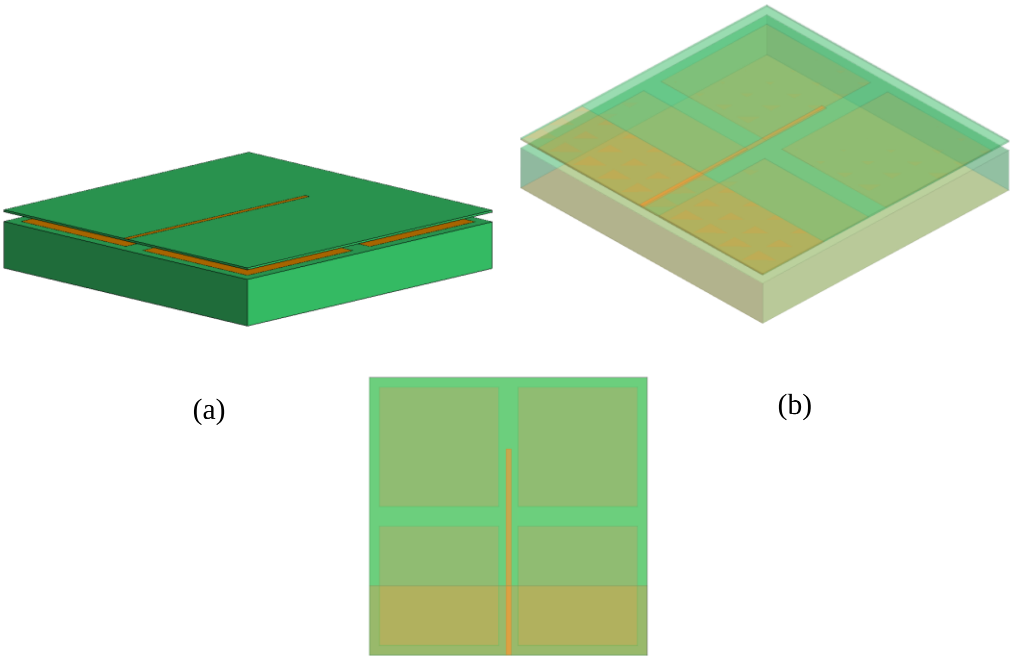

(a) (b)

(c)

Figure 4.7. Standard planar monopole simulation model. (a) Isometric view. (b) Transparent isometric view. (c) Transparent top view.

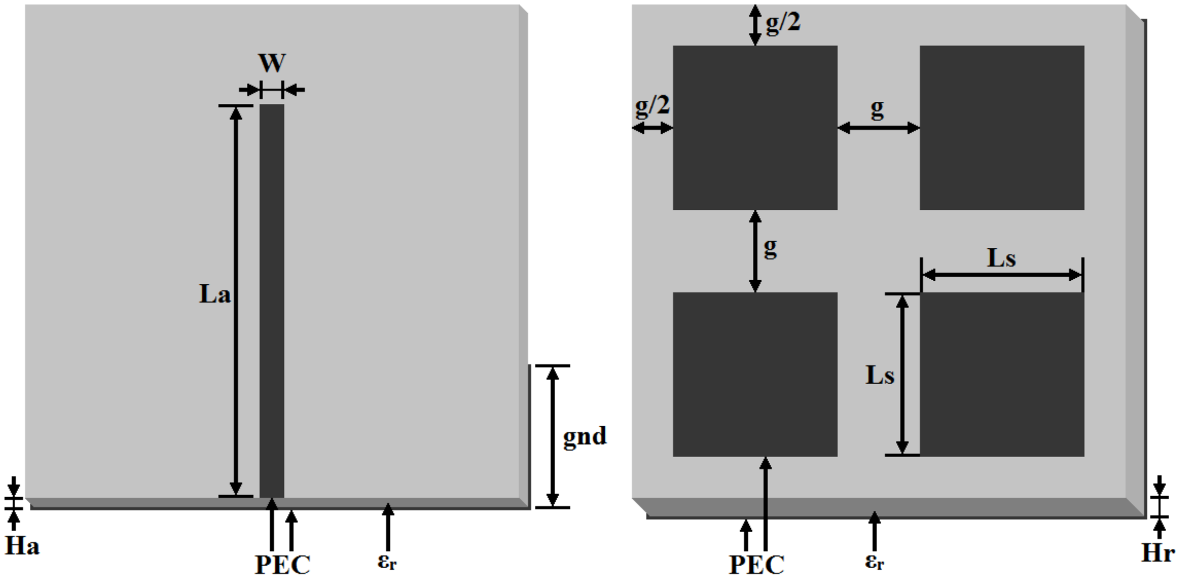

(a) (b)

Figure 4.8. Standard planar monopole design parameters.

Table 4.3. Design parameters for the standard planar monopole antenna.

Parameter	**Value**
Centre frequency (f_c)	433 MHz
Wavelength in free space (λ_0)	692.36 mm
Wavelength in dielectric (λ)	322.82 mm
Loss tangent (tan δ)	0.02
ε_r	4.6
Ha	1.6 mm
La	212.9 mm
W	3 mm
Gnd	70.8 mm
G	20.5 mm
Ls	121.1 mm
Hr	38.4 mm
Distance between antenna and RIS	13.85 mm
Total length and width	283.2 mm
Total height	53.85 mm

Figure 4.9 shows that by only modifying the length of the antenna ground, the size of the RIS squares, and the distance between RIS squares, the SMP antenna’s performance is greatly improved over that of the initially integrated antenna. Although the performance of the standard planar monopole antenna is already very good, with a wide -10 dB reflection coefficient bandwidth and high gain, it can be improved. The improved design is given in 4.4.3 below.

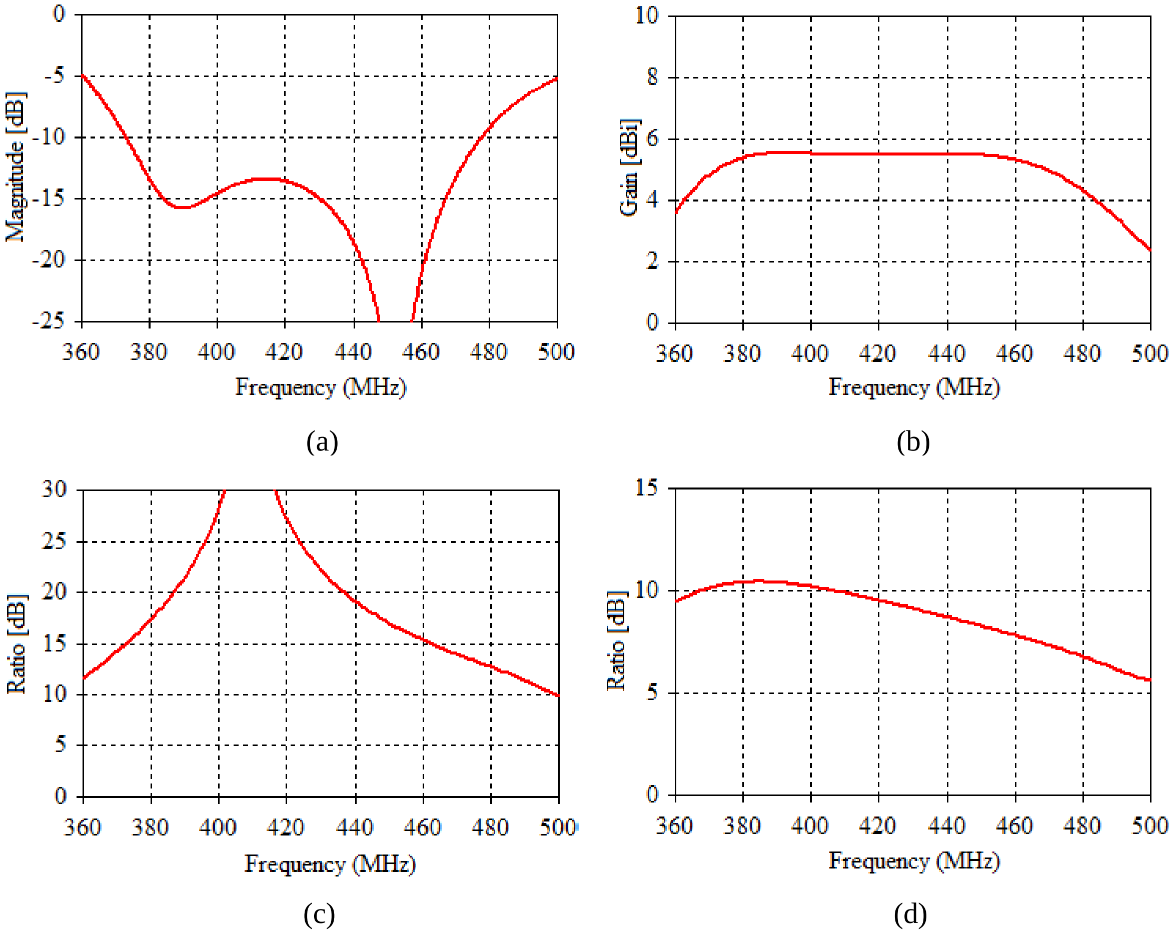

(a) (b)

(c) (d)

Figure 4.9. (a) Reflection coefficient. (b) Realised gain. (c) Front to back ratio. (d) Ratio of the radiated power in the forward hemisphere to that of the rear hemisphere.

4.4.3 Final design

The optimised design parameter values for the standard planar monopole antenna are listed in Table 4.4, with the total size of the antenna given as 277.29 mm by 277.29 mm by 48 mm, or 0.4 λ_0 by 0.4 λ_0 by 0.069 λ_0 where λ_0 is the wavelength in free space at 433 MHz.

Table 4.4. Design parameters for the standard planar monopole antenna.

Parameter	Value	Expression
Centre frequency (f_c)	433 MHz	
Wavelength in free space (λ_0)	692.36 mm	
Wavelength in dielectric (λ)	322.82 mm	
Loss tangent (tan δ)	0.02	
ε_r	4.6	
Ha	1.6 mm	0.005 λ
La	205.65 mm	0.637 λ
W	3 mm	0.009 λ
Gnd	69.33 mm	0.215 λ
G	19.45 mm	0.060 λ
Ls	119.2 mm	0.369 λ
Hr	38.4 mm	0.119 λ
Distance between antenna and RIS	8 mm	0.012 λ_0
Total length and width	277.29 mm	0.400 λ_0
Total height	48 mm	0.069 λ_0

The simulated radiation patterns for the standard planar monopole antenna can be seen in Figure 4.10 below. In simulation, the H-plane 3 dB beam width was found to be 98.9° wide, and the E-plane 3 dB beam width was found to be 91.2° wide. The maximum gain was found to be 5.63 dBi, and the cross polarization rejection was 20 dB or more in the aforementioned 3 dB main beam.

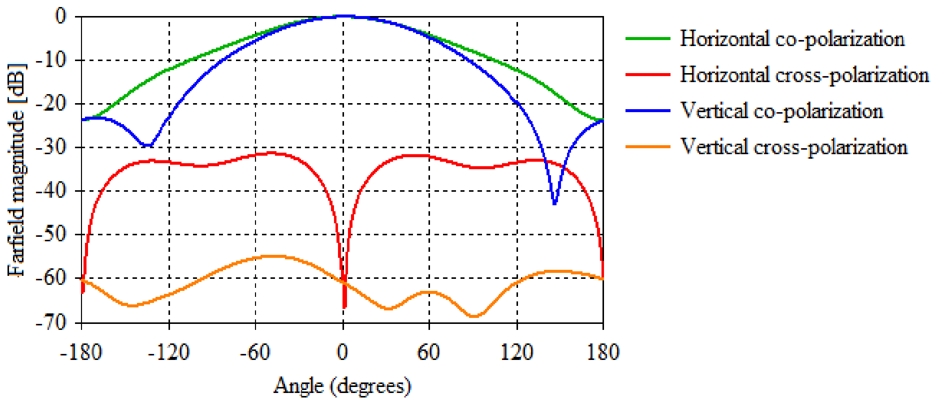

Figure 4.10. Normalised radiation patterns of the standard planar monopole.

Figure 4.11 gives the simulated reflection coefficient magnitude, boresight gain, and front to back ratio as a function of frequency, with the bandwidths indicated where the optimisation goals were achieved. The ratio of the average power radiated in the front hemisphere to the average power radiated in the rear hemisphere is given in Figure 4.11 (d), which is a better indication of how much the wearer is radiated than the front to back ratio. The simulated impedance bandwidth, indicated in Figure 4.11 (a), for the standard planar monopole antenna was 24.2 %. The bandwidth where the boresight gain was at least 5 dBi was slightly lower than the impedance bandwidth at 23.4 %, as indicated in Figure 4.11 (b). The front to back ratio in Figure 4.11 (c) was much smaller than the impedance and gain bandwidths, but as shown in Figure 4.11 (d) the vast majority of the radiated power is radiated away from the wearer over almost the entire -10 dB impedance bandwidth.

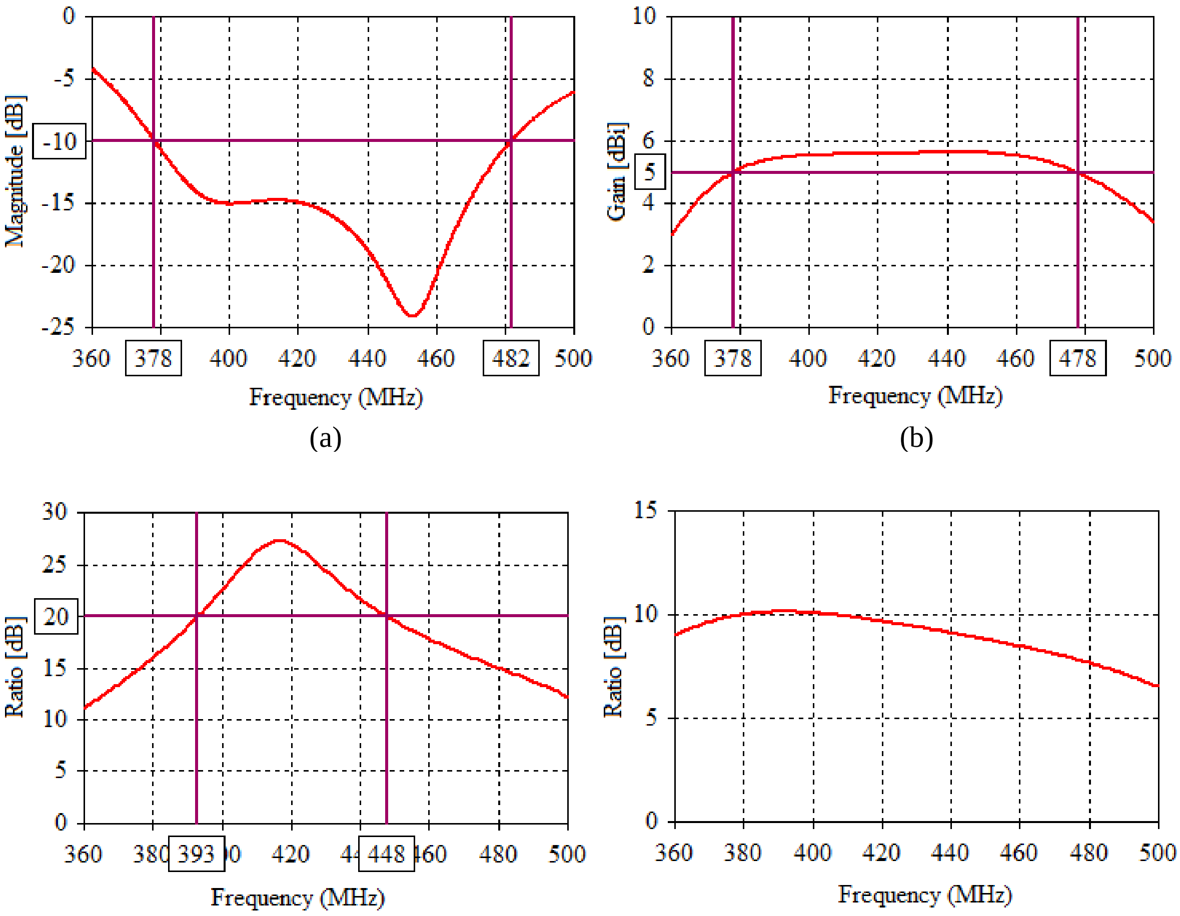

(a) (b)

(c) (d)

Figure 4.11. (a) Reflection coefficient. (b) Realised gain. (c) Front to back ratio. (d) Ratio of the radiated power in the forward hemisphere to that of the rear hemisphere.

As shown in Figure 4.12 the maximum radiation efficiency is not achieved at the same frequency as the maximum ratio between forward and backward radiated power. This indicates a trade-off between directivity and efficiency. It should be noted that the radiation efficiency is in excess of 80 % over the entire impedance bandwidth.

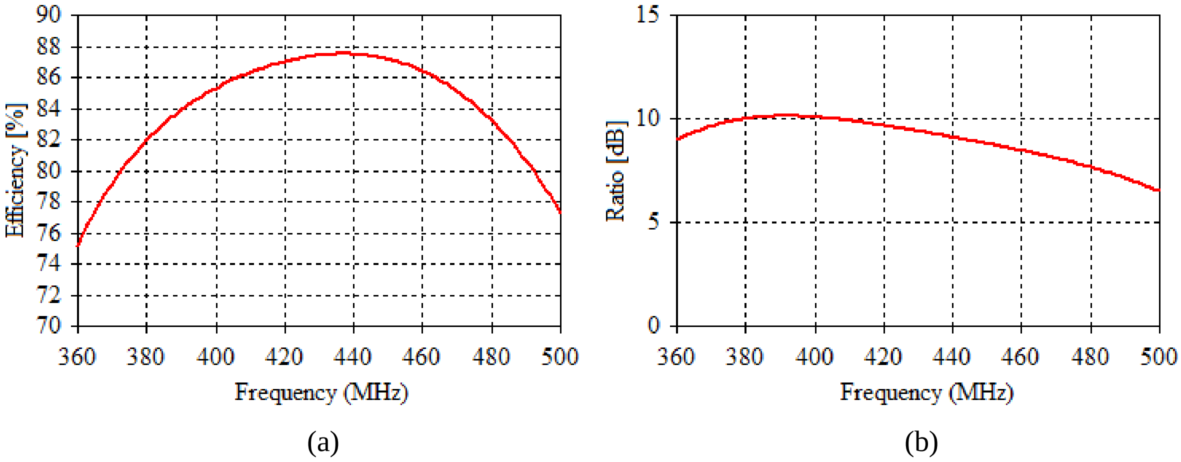

(a) (b)

Figure 4.12. (a) Antenna radiation efficiency. (b) Ratio of the power radiated in the front hemisphere to the power radiated in the rear hemisphere.

4.5 OPTIMISE FOR COMPACT SIZE

The final design of the standard planar monopole antenna was taken as a starting point to design an antenna that is as compact as possible. While optimising for compact size the width and length of the antenna were also considered in addition to the variables considered thus far, thereby making it a loaded planar monopole antenna. In this section the design goals are given for an antenna that is as compact as possible, and the final design is discussed.

4.5.1 Design goals

The design goals that were used are listed in Table 4.5. The RIS and antenna substrate heights were specified as 38.4 mm and 1.6 mm, as was the case for the standard planar monopole antenna, and an impedance bandwidth of at least 5 % was chosen to allow for manufacturing tolerances. With the aforementioned limitations the antenna was optimised to be as compact as possible.

Table 4.5. Design goals for the loaded planar monopole antenna.

Goal Title	Goal Description
Integrated antenna width and length	As small as possible
Integrated antenna height	Smaller than 0.25 λ
Integrated antenna substrate	FR-4
Antenna substrate height	1.6 mm
RIS height	38.4 mm
Input impedance	50 Ω
Centre frequency	433 MHz
Impedance bandwidth	A reflection coefficient of -10 dB over a bandwidth of least 5 %.
Gain	At least 5 dBi over at least 50 % of the impedance bandwidth
Front to back ratio	20 dB over at least 50 % of the impedance bandwidth
Ratio between power radiated in the front and rear hemispheres	At least 6 dB over the entire impedance bandwidth.
Radiation efficiency	At least 80 % over the entire impedance bandwidth.

4.5.2 Design procedure

The simulation model of the loaded planar monopole antenna is shown in Figure 4.13. Figure 4.13 shows that the antenna component of the loaded planar monopole antenna consists of two parts: a feed line and a square radiating element. A design procedure was developed based on the parametric studies conducted in Chapter 3, as well as the information gleaned through the design of the final antenna. The design procedure for the antenna that was designed to be as compact as possible is as follows:

- Design the RIS unit cell according to Equations (3.3) to (3.6).
- Design a planar monopole antenna according to Equations (4.1) to (4.3).
- Integrate the planar monopole and a two by two unit cell RIS, by placing the monopole at the RIS reference plane calculated with Equation (3.6).
- Reduce the thickness of the RIS by 30 %.
- Reduce the distance between square RIS patches by 80 %.
- Reduce the length of the antenna ground plane by 20 %.
- Increase the distance between the RIS and the antenna by 100 %.
- Increase the size of the square RIS patches by 40 %.
- Split the monopole into two parts, a square radiating element and a feed.
- Set the length and width of the square radiating element to 50 % of the original antenna length.
- Set the length of the antenna feed to 30 % of the original antenna length.
- Optimise to further reduce size while keeping the reflection coefficient, gain, and front to back ratio of the antenna at acceptable levels.

The design parameter values for the standard planar monopole antenna that are indicated in Figure 4.14, are listed in Table 4.6. This design can be optimised to further reduce the size of the integrated antenna, as well as to fine tune performance.

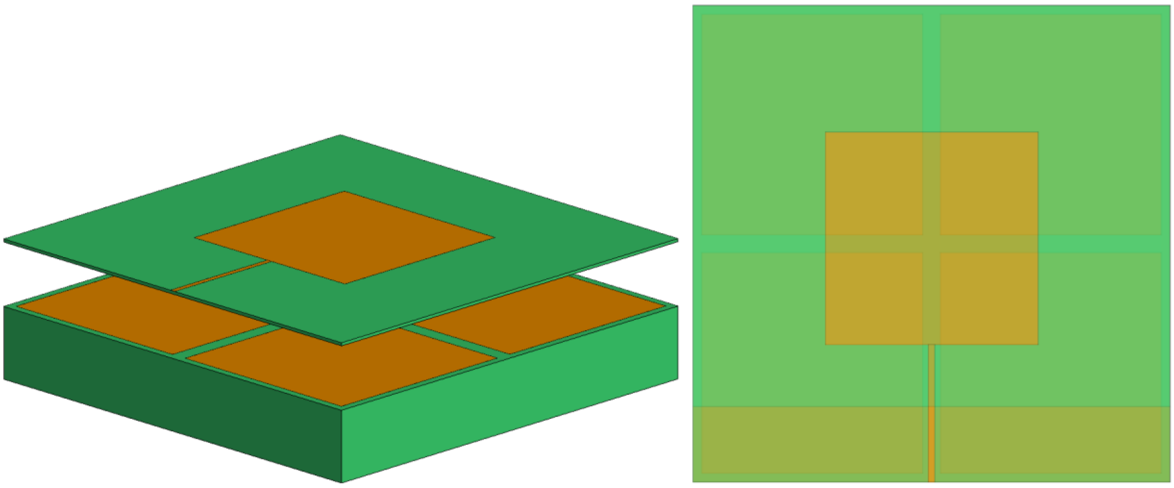

(a) (b)

Figure 4.13. Loaded planar monopole antenna. (a) Isometric view. (b) Transparent top view.

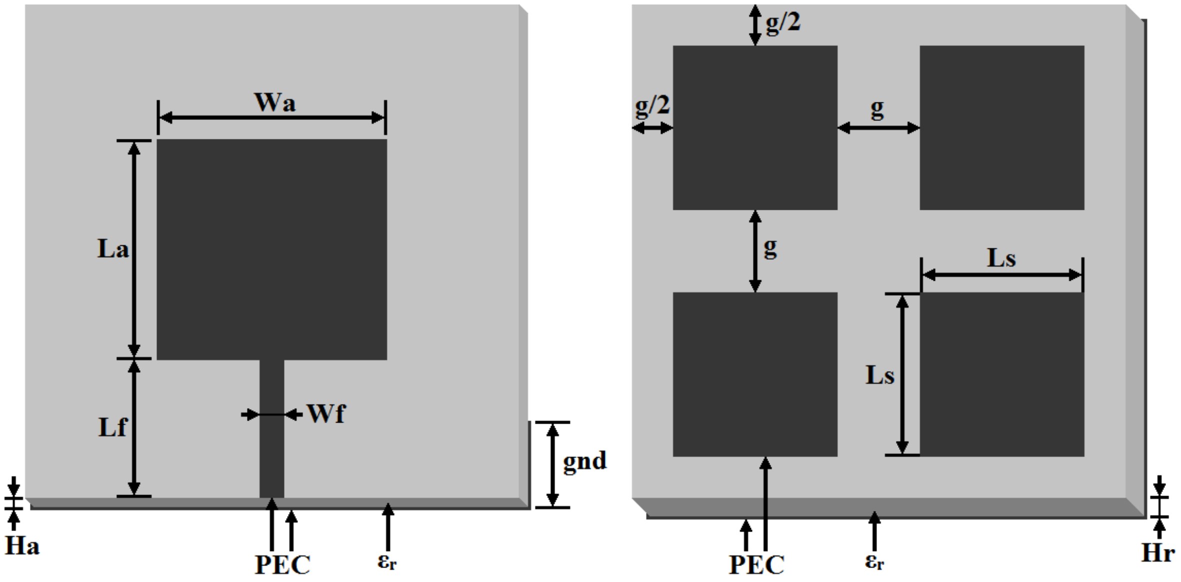

(a) (b)

Figure 4.14. Loaded planar monopole antenna model with design parameters indicated.

Table 4.6. Design parameters for the loaded planar monopole antenna.

Parameter	**Value**
Centre frequency (f_c)	433 MHz
Wavelength in free space (λ_0)	692.36 mm
Wavelength in dielectric (λ)	322.82 mm
Loss tangent (tan δ)	0.02
ε_r	4.6
Ha	1.6 mm
La	106.45 mm
Wa	106.45 mm
Lf	70.97 mm
Wf	3 mm
gnd	6 mm
g	8.2 mm
Ls	112.98 mm
Hr	38.4 mm
Distance between antenna and RIS	27.7 mm
Total length and width	242.36 mm
Total height	67.7 mm

When comparing the loaded planar monopole design parameters to that of the standard planar monopole antenna, it can be observed that the loaded planar monopole antenna is more than 10 % more compact in both width and length than the standard planar monopole antenna. Figure 4.15 shows that through the aforementioned modifications the loaded planar monopole antenna’s performance has improved over that of the initially integrated antenna. Although the performance of the loaded planar monopole antenna is not as good as that of the standard planar monopole antenna, it still has an acceptable -10 dB reflection coefficient bandwidth and an acceptably high gain. Both the performance, and the compact size, of the loaded planar monopole antenna can be further improved. The improved design is given in 4.5.3 below.

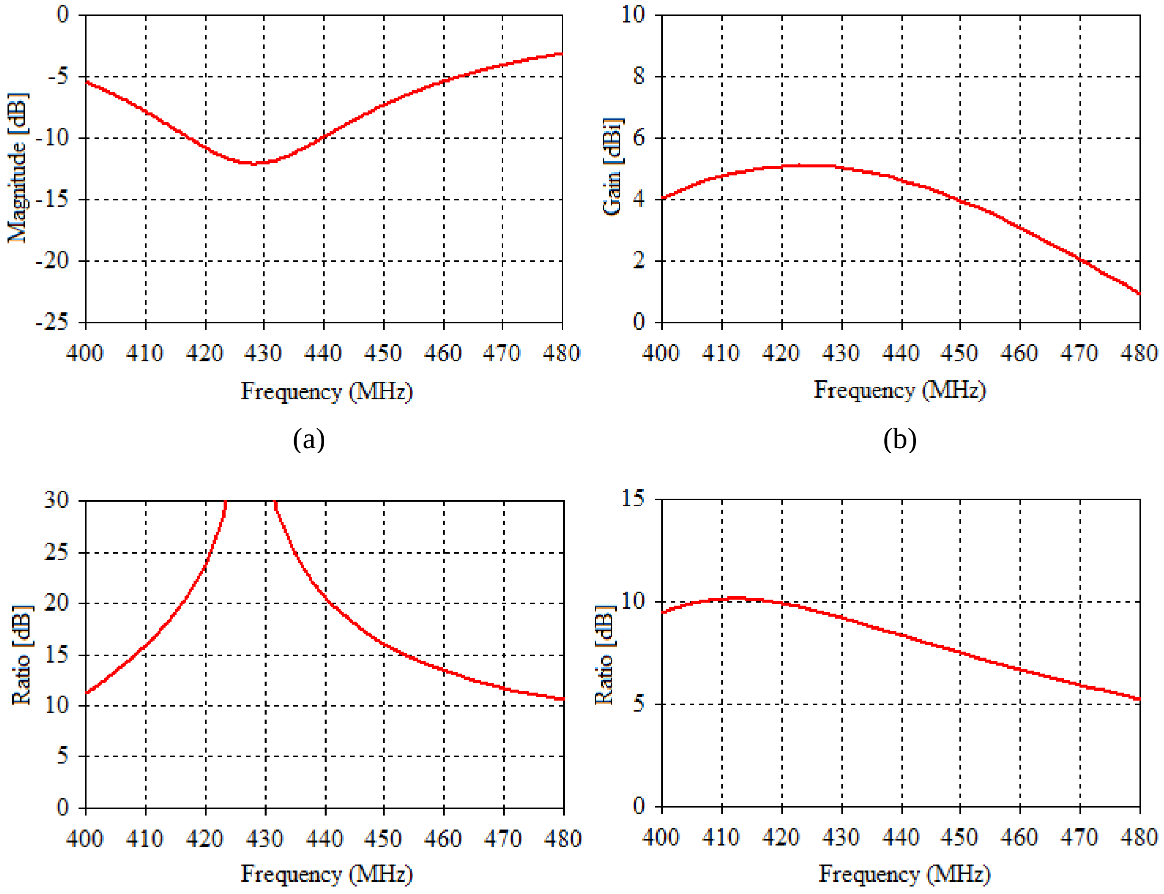

(a) (b)

(c) (d)

Figure 4.15. (a) Reflection coefficient. (b) Realised gain. (c) Front to back ratio. (d) Ratio of the radiated power in the forward hemisphere to that of the rear hemisphere.

4.5.3 Final design

The optimised design parameter values for the loaded planar monopole antenna are listed in Table 4.7 based on which the total size of the antenna can be found as 239.385 mm by 239.385 mm by 74 mm, or 0.346 λ_0 by 0.346 λ_0 by 0.107 λ_0 where λ_0 is the wavelength in free space at 433 MHz.

Table 4.7. Design parameters for the loaded planar monopole antenna.

Parameter	**Value**	**Expression**
Centre frequency (f_c)	433 MHz	
Wavelength in free space (λ_0)	692.36 mm	
Wavelength in dielectric (λ)	322.82 mm	
Loss tangent (tan δ)	0.02	
ε_r	4.6	
Ha	1.6 mm	0.005 λ
La	106.83 mm	0.331 λ
Wa	106.83 mm	0.331 λ
Lf	68.95 mm	0.214 λ
Wf	3 mm	0.009 λ
gnd	37.77 mm	0.117 λ
g	8.8 mm	0.027 λ
Ls	110.89 mm	0.343 λ
Hr	38.4 mm	0.119 λ
Distance between antenna and RIS	34 mm	0.049 λ_0
Total length and width	239.39 mm	0.346 λ_0
Total height	74 mm	0.107 λ_0

The simulated radiation patterns at 433 MHz for the antenna can be seen in Figure 4.16. The 3 dB beam width was 94.4° in the E-plane, and 109.8° in the H-plane, and the maximum gain was 5.2 dBi. Both the E- and H-plane cross polarization rejection was in excess of 30 dB at an angle smaller than 30° from boresight.

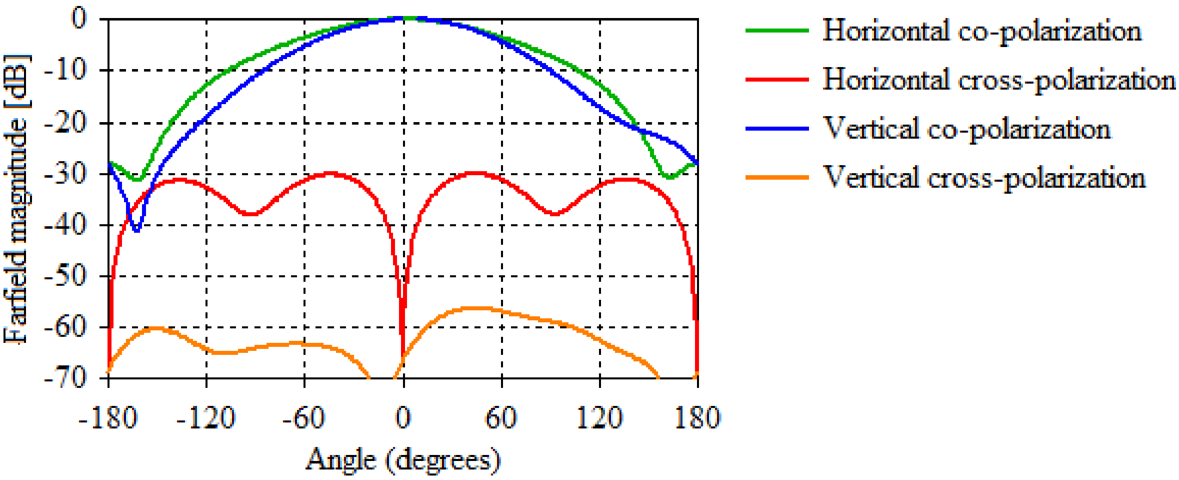

Figure 4.16. Radiation patterns: E- and H-plane co- and cross-polarization.

Figure 4.17 shows the reflection coefficient, boresight gain, and front to back ratio of the antenna, with the bandwidth where the design goal achieved was indicated in each graph. In a 50 Ω system the antenna achieved an impedance bandwidth of 6.29 %, which provides some tolerance for manufacturing errors. The 5 dBi gain bandwidth is 4.88 %, and the 20 dB front to back ratio bandwidth is 5.16 %. Combining the three performance indicators in Figure 4.17 the bandwidth can be found where the antenna performs optimally, i.e. where the antenna has a reflection coefficient of less than -10 dB, a gain of more than 5 dBi, and a front to back ratio of more than 20 dB. This optimal bandwidth is 3.81 % and ranges from 423.5 MHz to 441 MHz, with the design centre frequency of 433 MHz very nearly in the middle of the band.

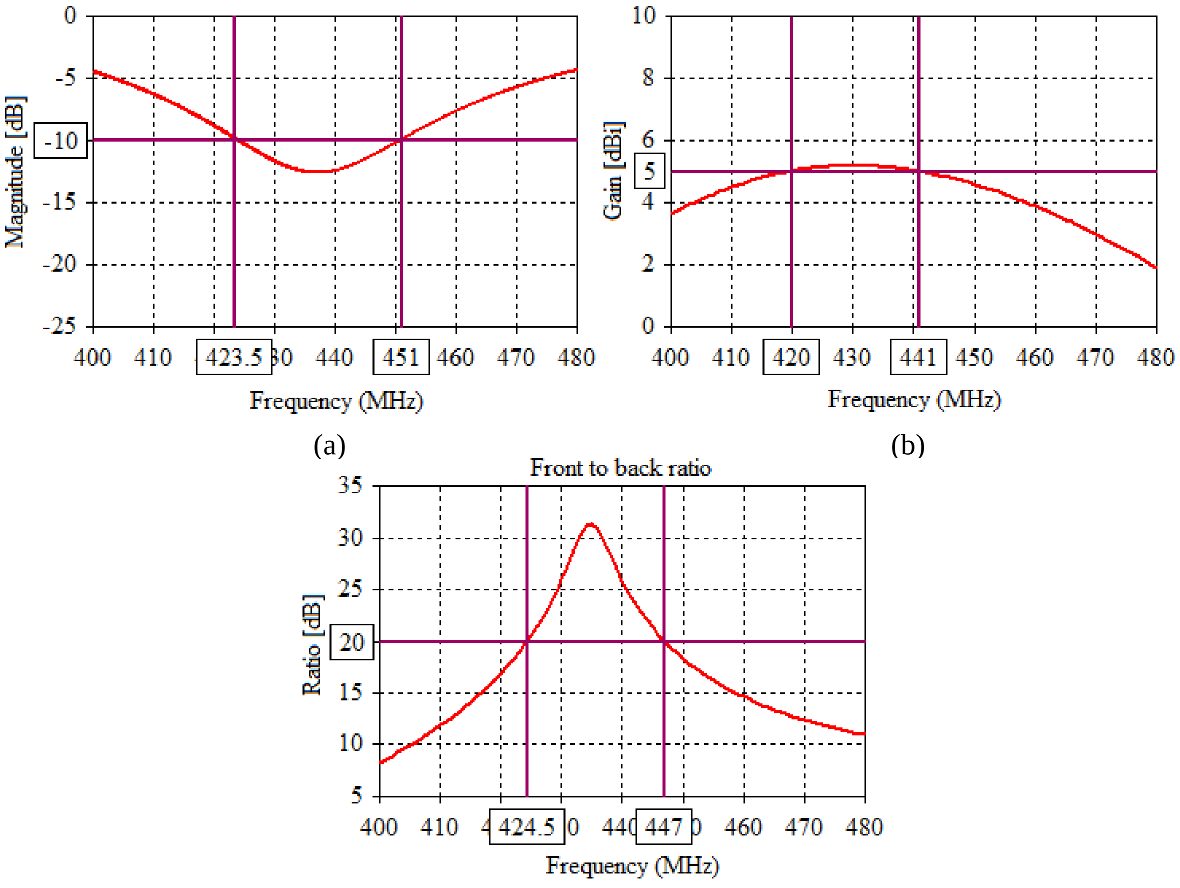

(a) (b)

(c)

Figure 4.17. (a) Reflection coefficient. (b) Realised gain. (c) Front to back ratio.

The total efficiency of the antenna is shown in Figure 4.18 (a), where it is clear that less than 15 % of the power fed into the antenna input is not radiated over the operating band, due to reflections and power dissipated in the antenna. Figure 4.18 (b) gives the ratio of the average power radiated in the front hemisphere to the average power radiated in the rear hemisphere. In Figure 4.18 (b) it can be seen that, for at least 5 MHz around the centre frequency of 433 MHz, 9 dB more power is radiated into the front hemisphere than into the rear hemisphere. It is worth noting that the form of Figure 4.18 (b) does not follow Figure 4.17 (c) closely, and therefore the front to back ratio can only be used as an indicator of wearability, whereas the ratio between the power radiated into the forward hemisphere and the power radiated into the rear hemisphere is a much more definitive measure of wearability.

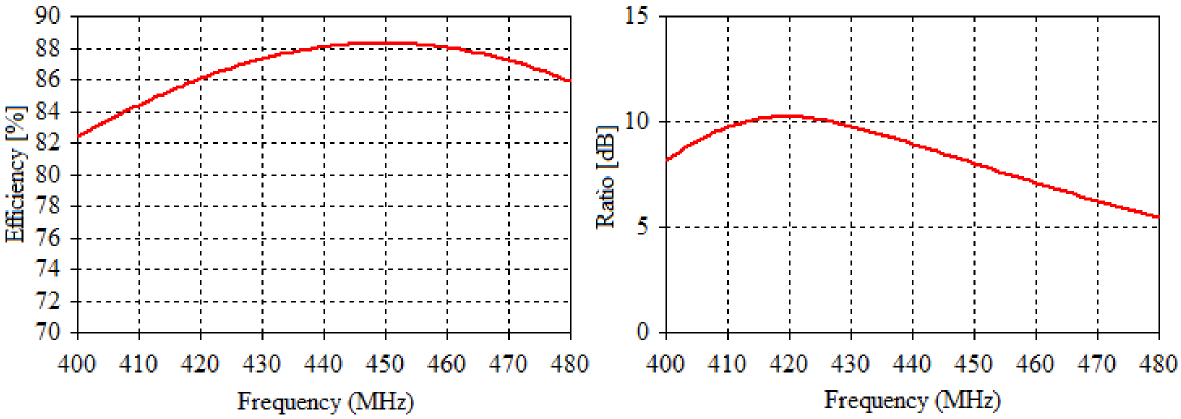

(a) (b)

Figure 4.18. (a) Antenna radiation efficiency. (b) Ratio of the power radiated in the front hemisphere to the power radiated in the rear hemisphere.

4.6 LOSS TANGENT PARAMETRIC SWEEP

The effects of changes to the loss tangent of the antenna and RIS materials on the antenna's performance were also investigated. This was necessary due to the fact that the loss tangent of FR-4 can vary between manufacturers, and by investigating the effects of changes in loss tangent manufacturing discrepancies can be anticipated and prevented if necessary. This investigation also shows the trade-offs between antenna performance and the material's loss tangent, which could allow for future designs to use even cheaper materials.

4.6.1 Standard planar monopole antenna

Figure 4.19 shows that increasing the loss tangent actually increases the standard planar monopole antenna's impedance bandwidth, but this increase comes at the cost of decreasing the antenna's radiation efficiency, which in turn decreases the maximum realised gain. Figure 4.19 (b) shows that changes to the loss tangent of the material does not have a significant effect on the ratio between the power radiated in the front and rear hemispheres, which means that the loss tangent of the material does not have an effect on wearability.

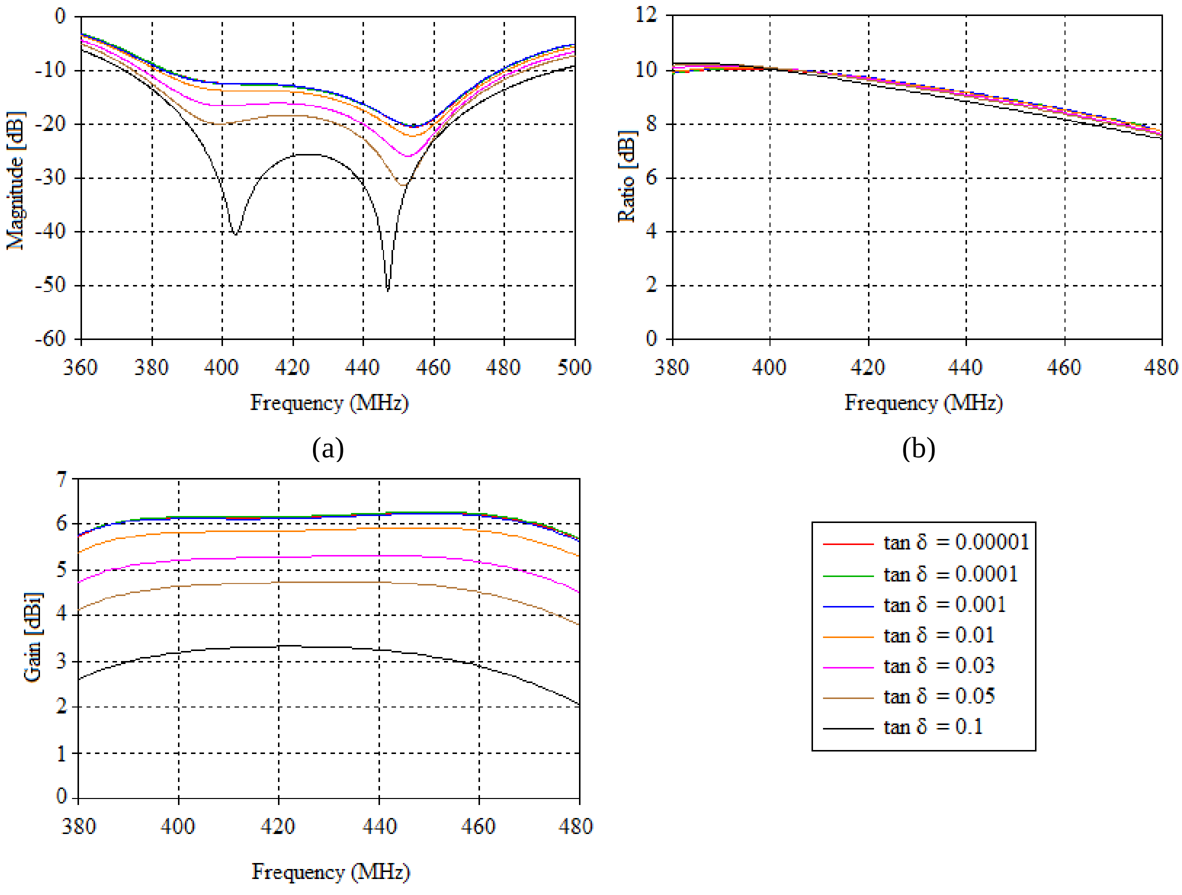

(a) (b)

(c)

Figure 4.19. Loss tangent (tan δ) parameter sweep. (a) Reflection coefficient. (b) Front hemisphere to rear hemisphere radiated power ratio. (c) Realised boresight gain.

4.6.2 Loaded planar monopole antenna

Figure 4.20 (a) shows that increasing the loss tangent decreased the antenna's impedance bandwidth, which is the opposite of what happened for the standard planar monopole antenna. This is most likely due to the fact that the bandwidth of the RIS decreases as the loss tangent of the RIS increases. Figure 4.20 (b) shows that the ratio between the power radiated in the front and rear hemispheres also decreases as the loss tangent increases. This was not the case for the standard planar monopole antenna. Finally, Figure 4.20 (c) shows that the maximum boresight gain of the antenna also decreases as the loss tangent is increased, due to the fact that the radiation efficiency of the antenna is decreased.

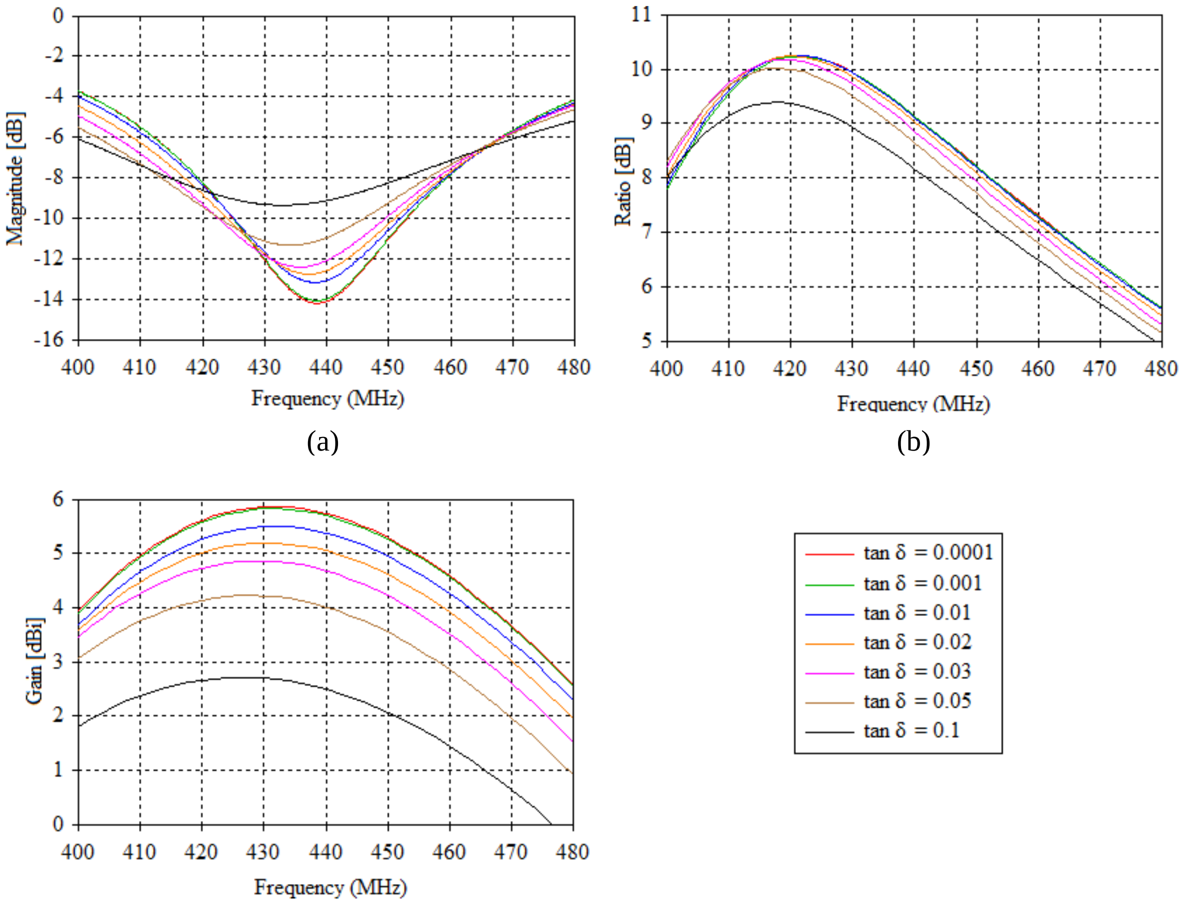

(a) (b)

(c)

Figure 4.20. Loss tangent (tan δ) parameter sweep. (a) Reflection coefficient. (b) Front hemisphere to rear hemisphere radiated power ratio. (c) Realised boresight gain.

4.7 THE EFFECTS OF HUMAN LOADING

The effects of human loading on antenna performance were investigated through simulation, based on the model in [5]. The model for human tissue was simulated with the properties listed in Table 4.8, and in the configuration shown in Figure 4.21. Simulations were done with a distance of 0.1 mm and 20 mm between the antenna and the human tissue. The width and length of the human tissue model was kept at double the width and length of the antenna.

Table 4.8. Human tissue model properties.

Layer	Dielectric constant	Conductivity (S/m)	Density (kg/m^3)	Layer thickness (mm)
Skin	37.95	1.49	1001	2
Fat	5.27	0.11	900	10
Muscle layer 1	52.67	1.77	1006	30
Bone	18.49	0.82	1008	20
Muscle layer 2	52.67	1.77	1006	60

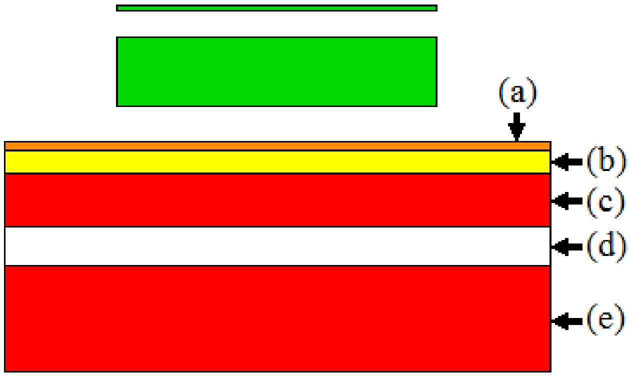

Figure 4.21. Human loading simulation model (the image is not to scale), based on the model from **[5]**. The antenna is at the top and the simulated human is at the bottom. The width and length of the human tissue model was kept at double that of the antenna. (a) Skin. (b) Fat. (c) Muscle layer 1. (d) Bone. (e) Muscle layer 2.

4.7.1 Standard planar monopole antenna

The effects of human loading on the standard planar monopole antenna's boresight gain and reflection coefficient is shown in Figure 4.22 below, where the simulated results without human tissue present was compared with the simulated results with human tissue at 0.1 mm, 20 mm and 40 mm away from the back of the antenna. From the simulated results it can be observed that both the 5 dBi gain bandwidth and the -10 dB impedance bandwidth decreased slightly, and that the 5 dBi gain bandwidth shifted to a slightly higher frequency range. For both the gain and the reflection coefficient however, the presence of the human tissue did not cause the performance to decay enough to render it less useful. On the contrary the bandwidths achieved in the design without the human tissue allowed the antenna to retain acceptable performance even though the performance did decrease slightly.

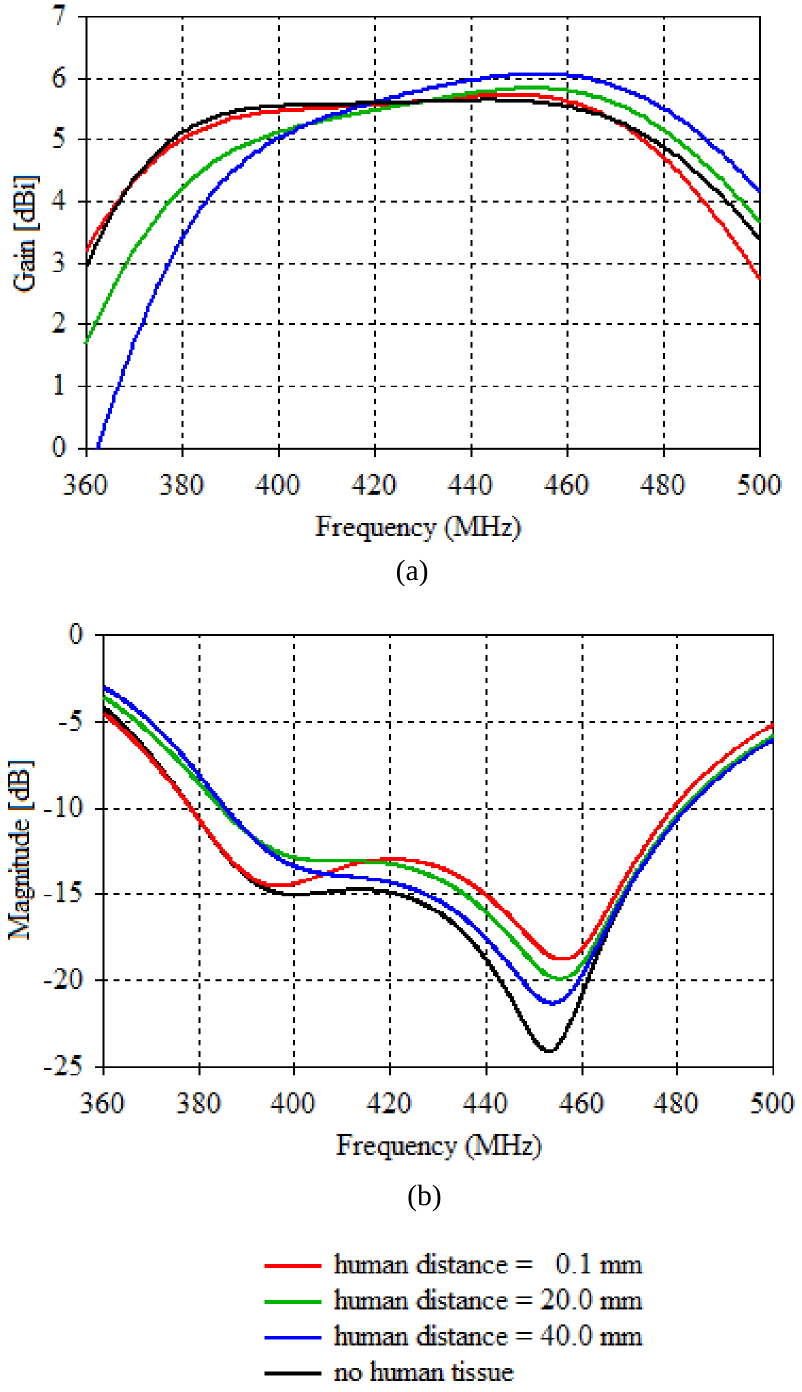

(a)

(b)

(c)

Figure 4.22. The effects of human loading on the standard planar monopole antenna. (a) Boresight gain. (b) Reflection coefficient. (c) Legend for the graph in (a) and the graph in (b).

4.7.2 Loaded planar monopole antenna

Figure 4.23 shows the effects of human loading on the boresight gain and reflection coefficient of the loaded planar monopole antenna. As was the case for the standard planar monopole antenna, the 5 dBi gain bandwidth decreased, and shifted to a slightly higher frequency range. For the loaded planar monopole antenna these changes were slightly more troublesome, as this antenna had less tolerance than the standard planar monopole antenna, but the 5 dBi gain bandwidth remained large enough to be practical. On the other hand, the reflection coefficient in Figure 4.23 (b) for the most part increased in bandwidth. When the human tissue was simulated 20 mm away from the antenna, the -10 dB impedance bandwidth did shift slightly higher, but not high enough to cause a problem, as the 433 MHz centre frequency remained comfortably in the -10 dB impedance bandwidth.

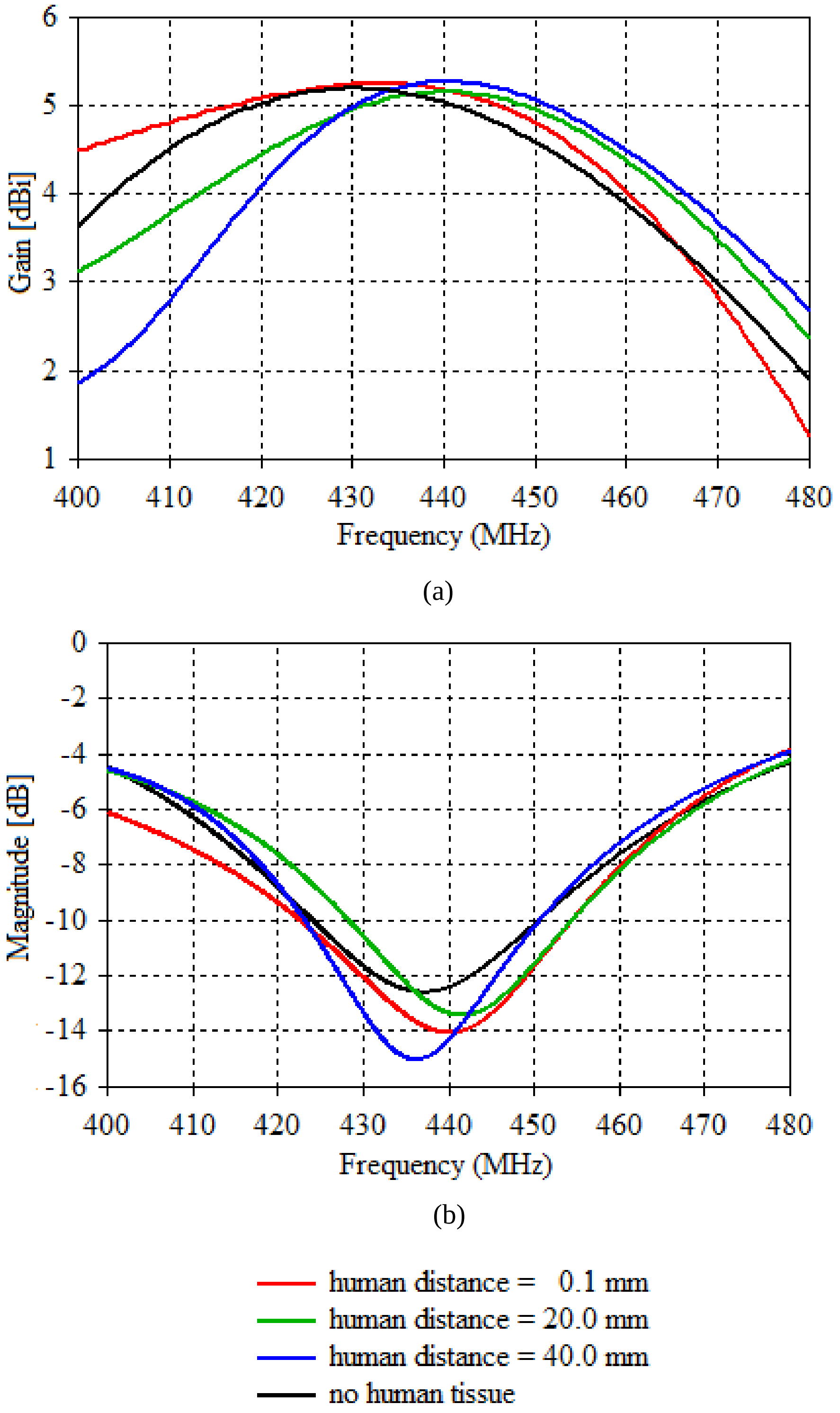

(a)

(b)

(c)

Figure 4.23. The effects of human loading on the loaded planar monopole antenna. (a) Boresight gain. (b) Reflection coefficient. (c) Legend for the graph in (a) and the graph in (b).

4.8 SUMMARY

In this chapter a planar monopole antenna was designed, based on the design equations from [61], to resonate at 433 MHz. On its own the antenna had a bidirectional radiation pattern with a maximum gain of 1.8 dBi, and an impedance bandwidth of 9.2 %. The square patch RIS unit cell was modified to have a 0° phase reflection, and four of these unit cells were used in a 2 by 2 configuration as the final RIS. The planar monopole antenna and the RIS were then integrated and simulated. Initially the integration of the planar monopole and the RIS was not completely successful. As intended the antenna’s radiation pattern became much more directional, and because of this the antenna’s maximum gain increased by 1.2 dBi to 4 dBi, but the antenna’s reflection coefficient was degraded so as to be larger than -10 dB at 433 MHz.

After identifying the physical limitations of using a 38.4 mm thick RIS the planar monopole antenna, backed by a 2 by 2 square patch RIS, was optimised for performance. This integrated antenna is referred to here as the standard planar monopole antenna. In this case it was possible to improve both the impedance bandwidth as well as the maximum gain over the original planar monopole antenna without an RIS. The impedance bandwidth was improved from 9.2 % to 24.2 %, which is more than double the original bandwidth, and the maximum gain was improved by 3.83 dB, from 1.8 dBi to 5.63 dBi.

The standard planar monopole antenna was then used as a starting point before being optimised to be as small as possible. This antenna is referred to here as the loaded planar monopole antenna. The loaded planar monopole antenna had a maximum gain of 5.2 dBi, which is an improvement of 3.4 dB over the original planar monopole antenna without an RIS. The impedance bandwidth of the integrated loaded planar monopole antenna was 6.29 %, which is slightly narrower than the 9.2 % impedance bandwidth of the original planar monopole antenna without an RIS. This impedance bandwidth does, however, comply with the requirement of designing for an impedance bandwidth that is larger than 5 %, which will allow for manufacturing tolerances.

It was also found that even though the standard planar monopole antenna was slightly more impervious to increases in material loss tangent, both antennas maintained acceptable performance as the loss tangent increased. With regards to antenna gain, both antennas provided an acceptable trade-off between achieving relatively high gain and using a material with a relatively high loss tangent. This could allow for these antennas to be redesigned for cheaper, and more lossy materials in the future.

While investigating the effects of human loading on the antennas' performance, it was found that although both antennas were affected by the presence of human tissue, the negative effects were not enough to degrade the antennas' performance to below acceptable levels. In simulation both antennas proved resistive to the effects of human loading, which means that both antennas should remain effective whilst being worn.

CHAPTER 5 PERFORMANCE EVALUATION

5.1 INTRODUCTION

In this chapter, the measurement results for both the standard planar monopole antenna, as well as the loaded planar monopole antenna, are presented and compared with simulated results. For both antennas, the impedance characteristics were measured at the compact antenna measurement range at the University of Pretoria, and the radiation characteristics were measured at the premises of SAAB Grintek Defence in Centurion, South Africa (typical setup shown in Figure 5.1), and verified at the Paardefontein National Antenna Measurement Range in Pretoria, South Africa.

Due to high ambient noise in the RFID frequency bands between 400 MHz and 500 MHz, the radiation patterns measured at SAAB Grintek Defence were preferred over the same measurements at Paardefontein. The magnitude of gain measurements on the other hand, had great uncertainty at SAAB Grintek Defence, mainly due to the size of their measurement facilities, and therefore the gain magnitude measurements at Paardefontein would take precedence. All measurements from Paardefontein and SAAB Grintek defence were compared and filtered before being presented here.

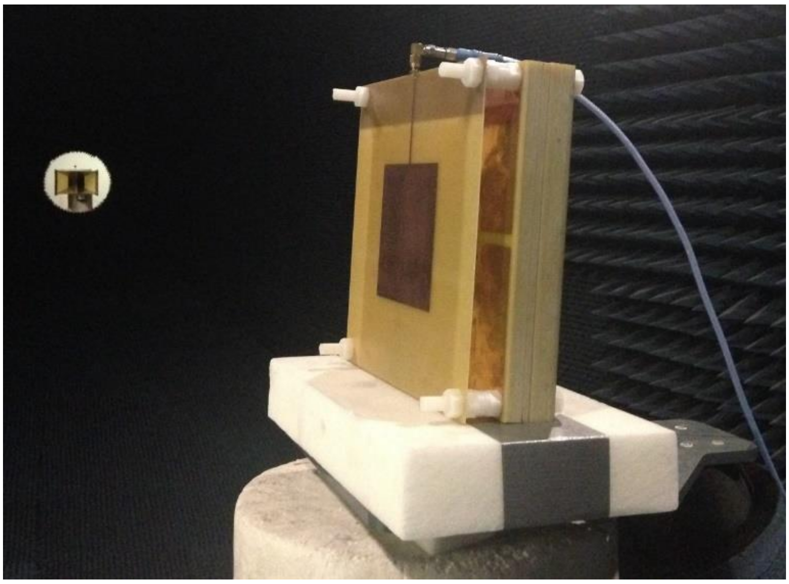

Figure 5.1. Antenna measurement setup at SAAB Grintek Defence.

5.2 STANDARD PLANAR MONOPOLE ANTENNA

The standard planar monopole antenna was designed for optimal performance, and therefore was allowed to be as large as needed. The manufactured prototype, shown in Figure 5.2, was constructed by fixing twelve layers of 3.2 mm thick FR-4 together with nylon screws to create the RIS, and suspending the 1.6 mm antenna layer above the RIS with the same screws.

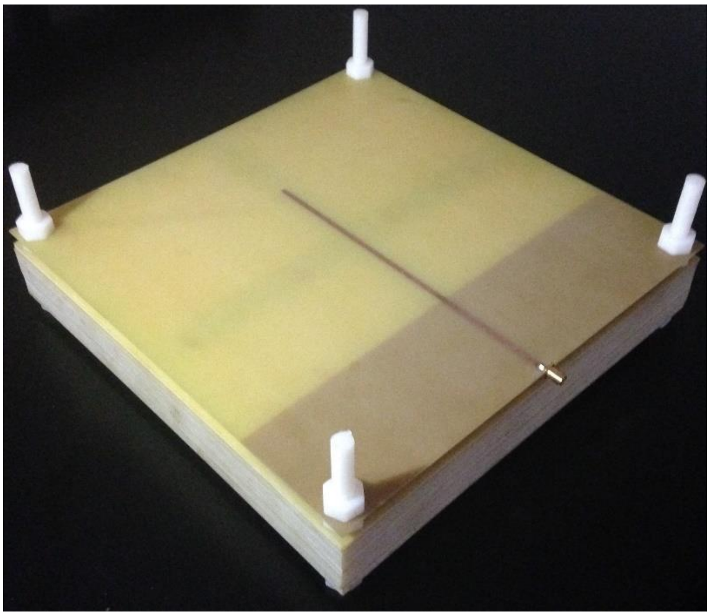

Figure 5.2. Manufactured standard planar monopole antenna.

5.2.1 Impedance characteristics

The impedance characteristics were measured over a 300 MHz frequency range, from 300 MHz to 600 MHz, with a Hewlett Packard 8753C vector network analyser. The reflection coefficient was first measured with the antenna isolated from interference and compared with the simulated results. Then, to measure the effects of human loading, a human held the antenna, initially without any separation between the antenna and said human, and finally with 20 mm separation between the antenna and the human. The effects of human loading were also compared with simulation.

5.2.1.1 Reflection coefficient

The measured and simulated reflection coefficients were compared in Figure 5.3. Due to differences between the simulated model and the manufactured prototype, caused by manufacturing tolerances or otherwise, the -10 dB impedance bandwidth of the manufactured antenna shifted to a slightly higher frequency range than in simulation. The bandwidth did not change all that much, increasing from 24.2 % to 25.1 %, the centre frequency however, did shift up by about 20 MHz to roughly 450 MHz. This difference is most likely due to variations between dielectric constants and loss tangents of the simulated and measured antennas. The design frequency of 433 MHz fell comfortably into the measured -10 dB impedance bandwidth.

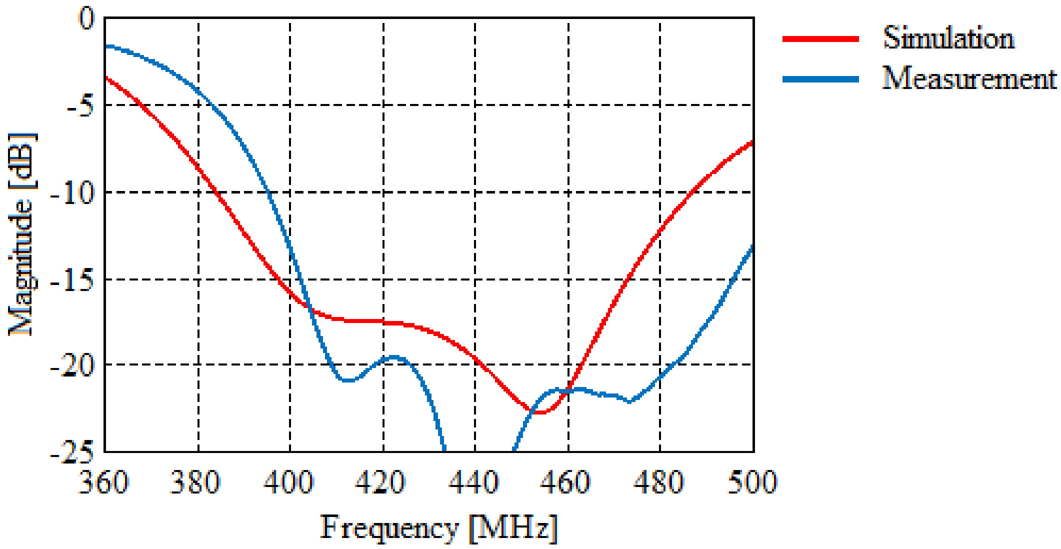

Figure 5.3. Measured (blue) and simulated (red) reflection coefficient for the standard planar monopole antenna.

5.2.1.2 Effect of human loading

The effect of human loading on the standard planar monopole antenna's reflection coefficient can be seen in Figure 5.4, where the simulated results in (a) are compared with the measured results in (b). In Figure 5.4 (b) it is clear that human loading caused the standard planar monopole antenna's impedance bandwidth to increase. Although the standard planar monopole antenna's -10 dB impedance bandwidth was increased through human loading, it should be noted that in the centre of the bandwidth the reflection coefficient decreased, although it was still below -10 dB. While comparing Figure 5.4 (a) and (b) it can be observed that even though the simulated and measured results are very similar, there were still some differences. These differences were most likely due to inaccuracies in the simulated model of human tissue.

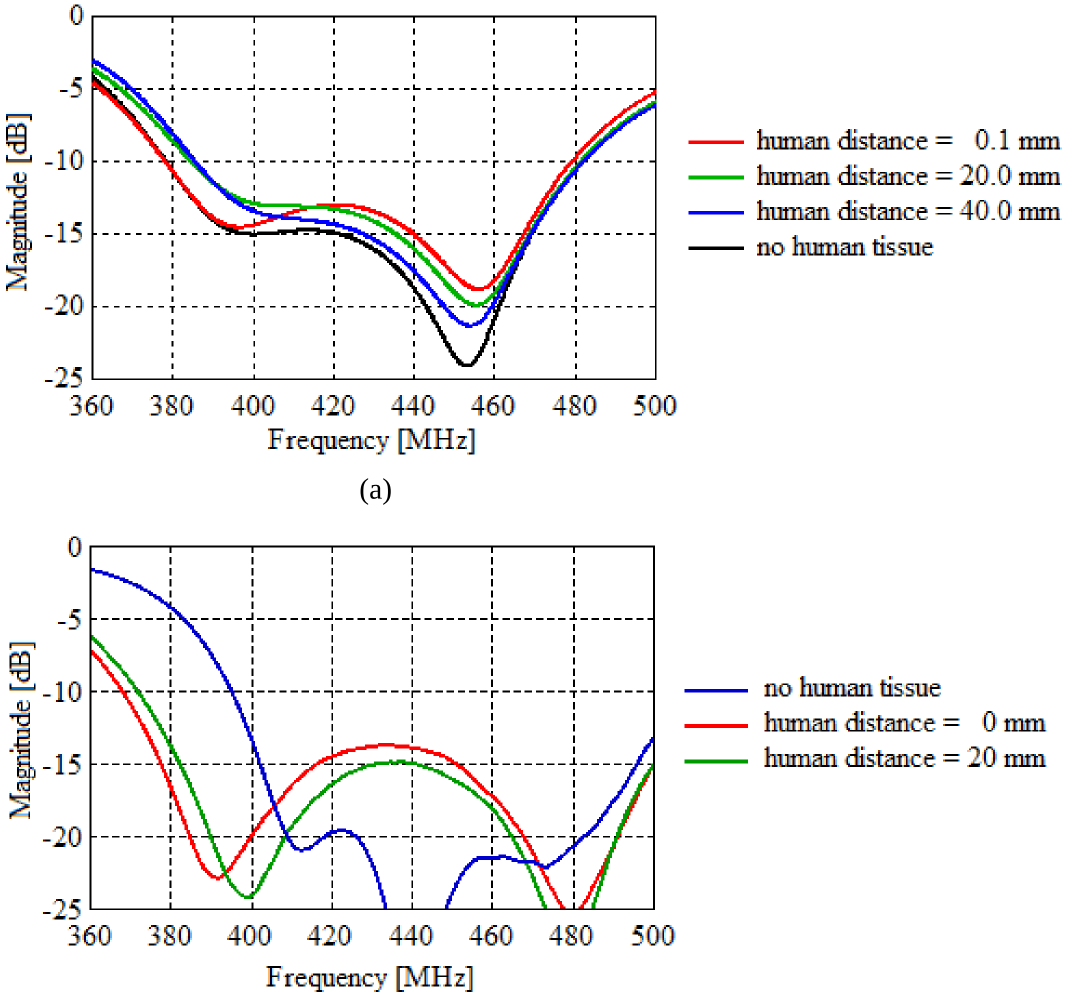

(a)

(b)

Figure 5.4. The effect of human loading on the standard planar monopole antenna's reflection coefficient. (a) Simulated results. (b) Measured results.

5.2.2 Radiation characteristics

Radiation pattern measurements were conducted in the large tapered chamber at SAAB Grintek Defence South Africa. Measurement were recorded with an Anritsu 37269D vector network analyser and calibrated based on measurements of the CBL6143A bilog antenna from Teseq. Results were processed and graphed using the MATLAB software package.

5.2.2.1 Gain

The boresight gain was measured from 400 MHz to 500 MHz, where the standard planar monopole antenna has a reflection coefficient of -10 dB or less. In Figure 5.5 it can be observed that for the most part the measured results were slightly lower than the simulated results. Nevertheless, the simulated results were very close to the measured results, with less than 1 dB difference between the two up to 480 MHz. The measured gain was higher than the simulated gain between 480 MHz and 500 MHz due to the frequency shift that occurred in the standard planar monopole antenna's reflection coefficient from simulation to practice.

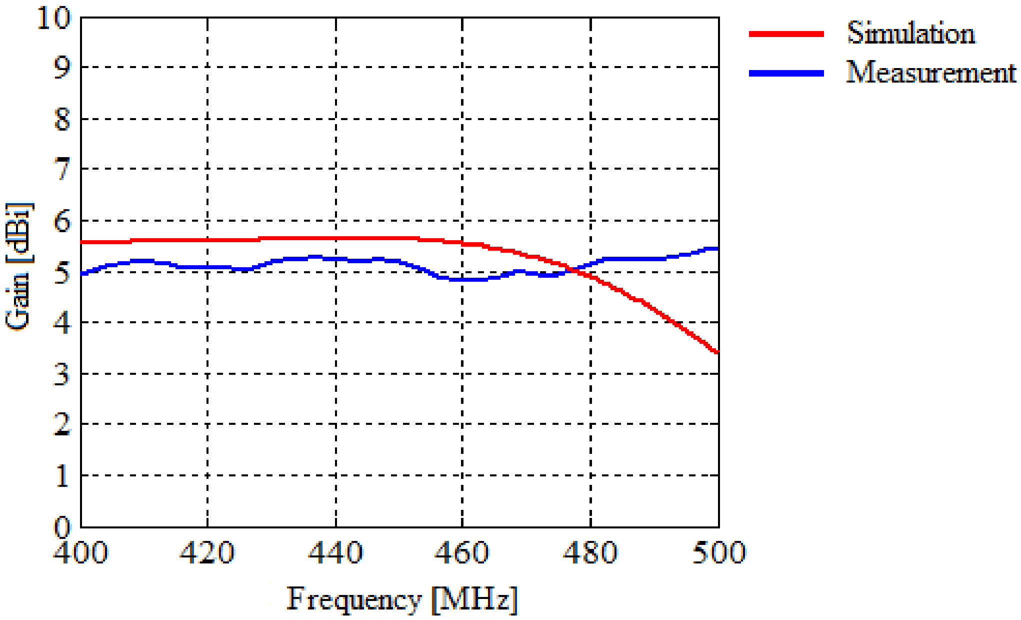

Figure 5.5. Simulated and measured gain as a function of frequency for the standard planar monopole antenna.

5.2.2.2 Radiation patterns

A comparison between simulated and measured radiation patterns is given in Figure 5.6, where it can be observed that the simulated and measured co-polarization patterns are very similar. The measured H-plane 3 dB beam width was 87.97°, compared to a simulated beam width of 98.9°, and the measured E-plane 3 dB beam width was 80.58°, compared to the 91.2° achieved in simulation. Both the E- and H-plane 3 dB beam widths were narrower in practice than in simulation, though still wide as both were wider than 80°. The measured cross-polarization was not as good as was achieved in simulation, although it is still acceptable with a cross-polarization rejection level of 19 dB at boresight.

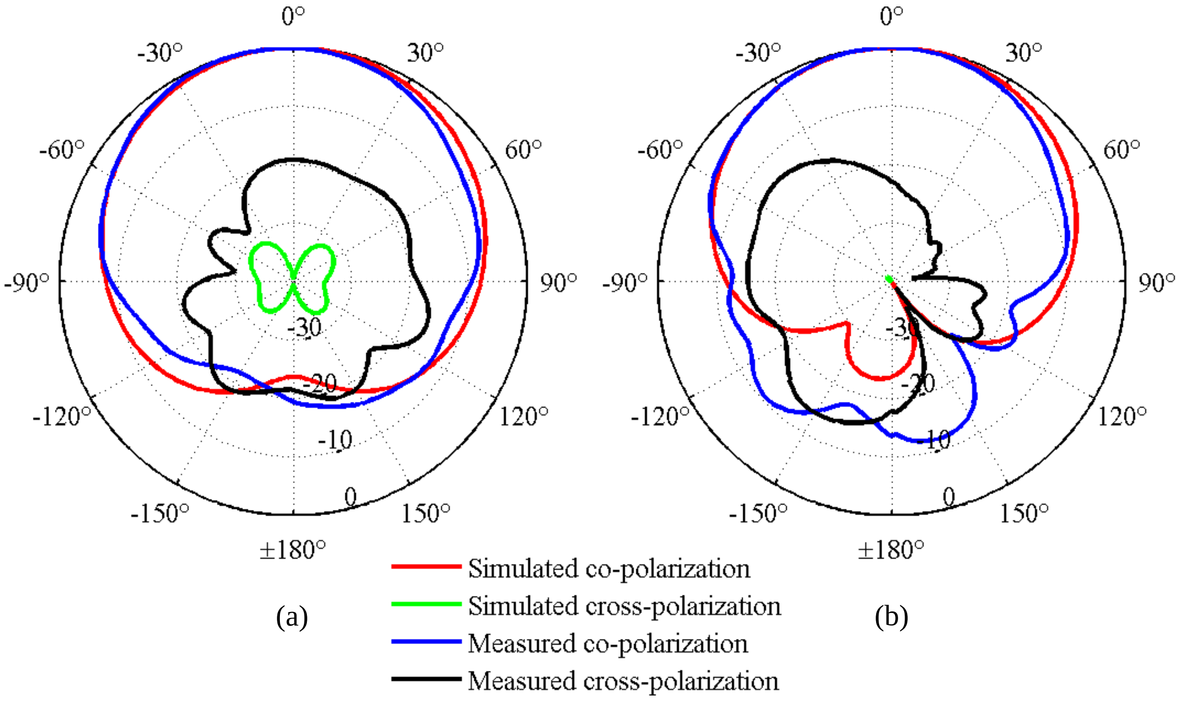

(a) (b)

Figure 5.6. The standard planar monopole antenna’s normalised simulated and measured far field radiation patterns. (a) H-plane co- and cross-polarization. (b) E-plane co- and cross-polarization.

The H-plane co-polarization far field magnitude is given in Figure 5.7 below as a function of both horizontal (azimuth) angle, and frequency. In Figure 5.7 it can be seen that the H-plane 3 dB beam width, as well as the maximum gain direction, remains largely constant. It can also be observed that the majority of the radiated power is being radiated into the front hemisphere.

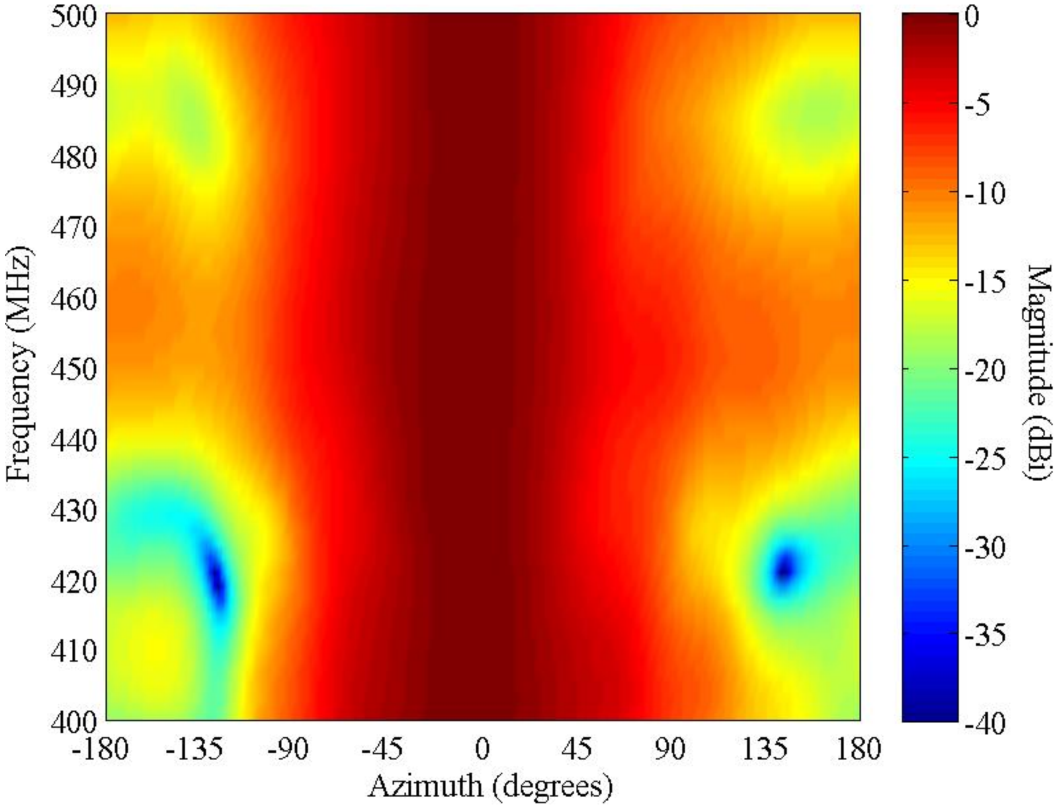

Figure 5.7. Colour plot of the manufactured standard planar monopole antenna's normalised H-plane co-polarization, with the horizontal (azimuth) angle on the x-axis, the frequency on the y-axis, and the far field magnitude indicated with a colour scale.

The E-plane co-polarization far field magnitude is shown in Figure 5.8 below as a function of both vertical (elevation) angle, and frequency. In Figure 5.8 it can be observed that the majority of energy is being radiated in the front hemisphere, and that the front hemisphere in general remains largely constant over the entire measured frequency range.

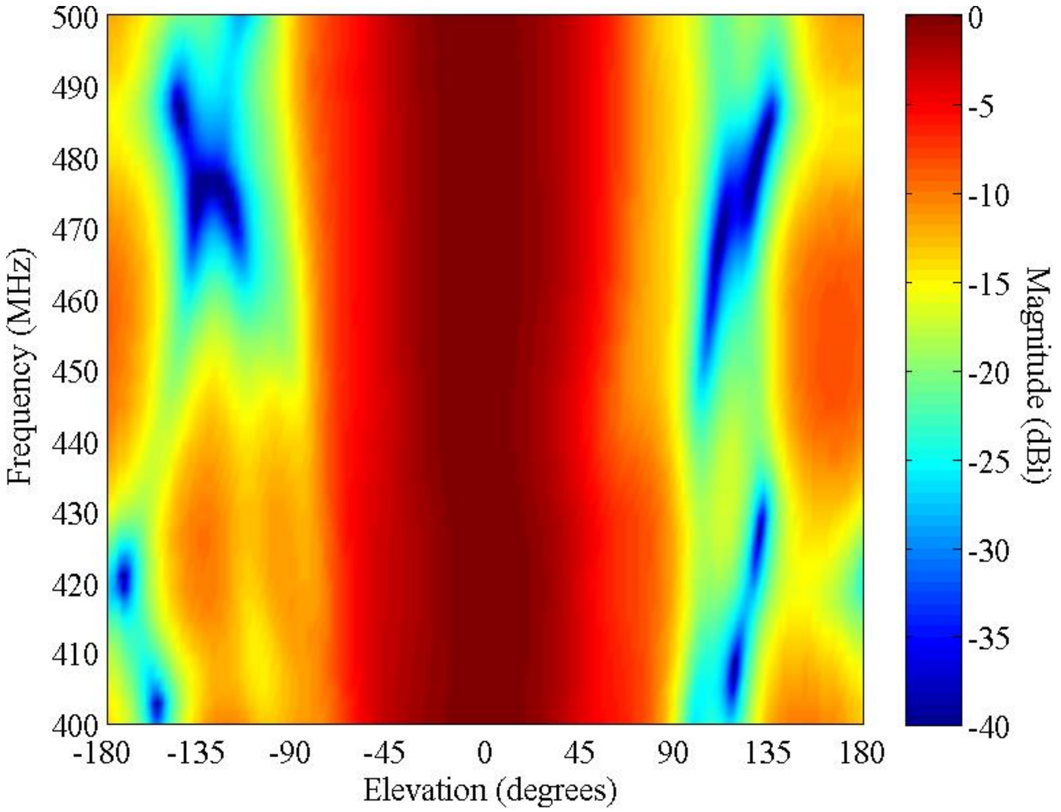

Figure 5.8. Colour plot of the manufactured standard planar monopole antenna's E-plane co-polarization, with the horizontal (azimuth) angle on the x-axis, the frequency on the y-axis, and the far field magnitude indicated with a colour scale.

Figure 5.9, Figure 5.10, and Figure 5.11 show the measured radiation patterns, i.e. both E- and H-plane co- and cross-polarization, in 20 MHz increments, from 400 MHz to 500 MHz. Figure 5.9, Figure 5.10, and Figure 5.11 give an indication of how the standard planar monopole antenna's radiation patterns change over frequency.

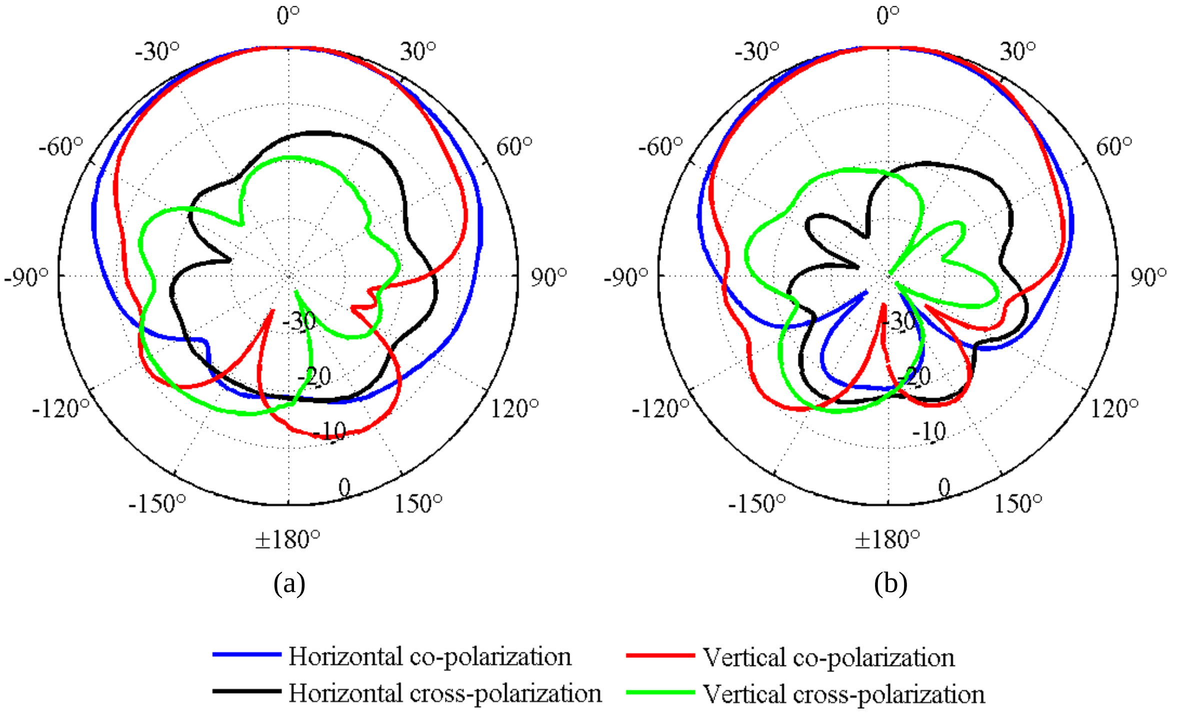

(a) (b)

Figure 5.9. Normalised measured radiation patterns. (a) 400 MHz. (b) 420 MHz.

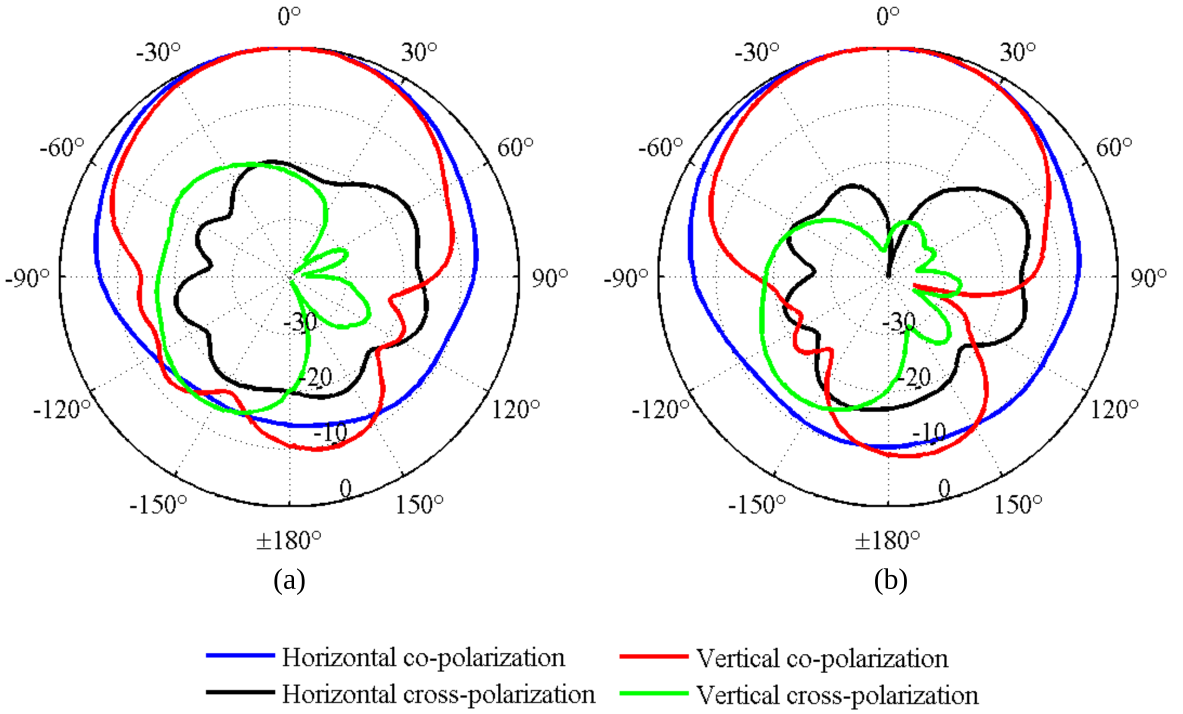

(a) (b)

Figure 5.10. Normalised measured radiation patterns. (a) 440 MHz. (b) 460 MHz..

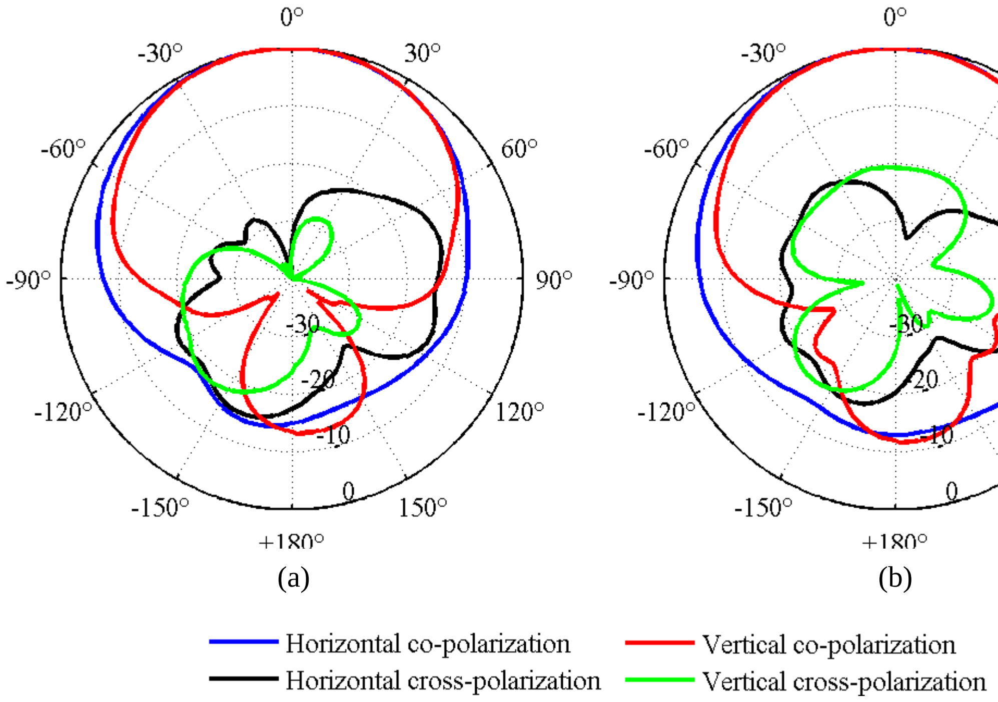

Figure 5.11. Normalised measured radiation patterns. (a) 480 MHz. (b) 500 MHz.

5.2.2.3 Power radiated forward

The power radiated forward is indicated by the ratio between the average power radiated in the front hemisphere to the average power radiated in the rear hemisphere, referred to below as the front to back power ratio. Figure 5.12 shows that the measured front to back power ratio was slightly worse than the simulated result at 433 MHz, with a rather large ripple in the measured plot line. The differences here are, for the most part, due to differences between the measured and simulated radiation patterns. The differences in the patterns can be due to inaccuracies in present in simulation, such as the fact that ambient noise is not present in simulation. The differences can also be due to manufacturing variance and measurement tolerances. The most important observation that can be made based on this result is that at least 6 dB more power radiates forwards than backwards, which means that most of the power is radiated away from the wearer.

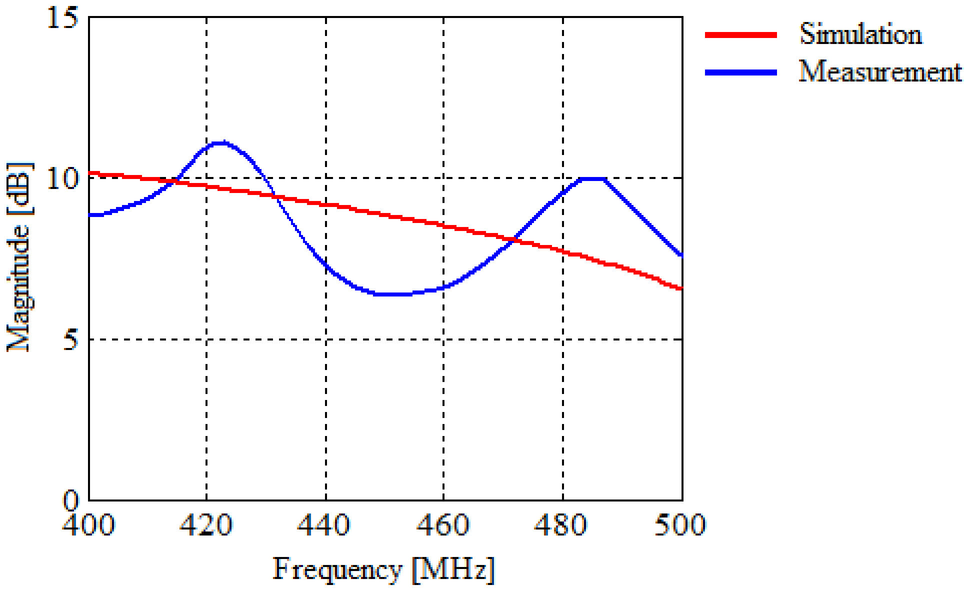

Figure 5.12. Simulated and measured front to back power ratio for the standard planar monopole antenna. The front to back power ratio is the ratio between the average power radiated in the front hemisphere to the average power radiated in the rear hemisphere.

5.3 LOADED PLANAR MONOPOLE ANTENNA

The loaded planar monopole antenna was optimised for compact and therefore it was much smaller than the standard planar monopole antenna. The manufactured prototype that can be seen in Figure 5.13, was constructed by fixing twelve layers of 3.2 mm thick FR-4 together with nylon screws to create the RIS, and suspending the 1.6 mm antenna layer above the RIS with the same screws – in other words, in the same manner as was the case for the standard planar monopole antenna.

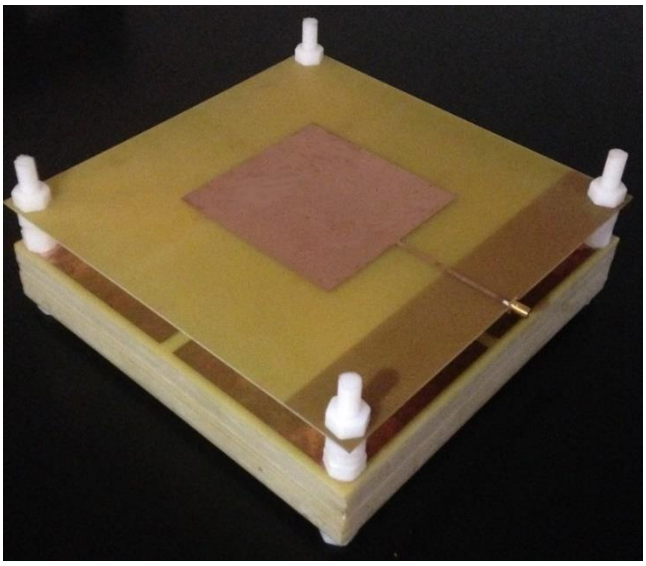

Figure 5.13. Manufactured loaded planar monopole antenna.

5.3.1 Impedance characteristics

The impedance characteristics were measured over a 300 MHz frequency range, from 300 MHz to 600 MHz, with a Hewlett Packard 8753C vector network analyser. The reflection coefficient was first measured with the antenna isolated from interference and compared with the simulated results. Then, to measure the effects of human loading, a human held the antenna, initially without any separation between the antenna and said human, and finally with 20 mm separation between the antenna and the human. The effects of human loading were also compared with simulation.

5.3.1.1 Reflection coefficient

The measured and simulated reflection coefficients were compared in Figure 5.14. Due to manufacturing tolerances or otherwise, the -10 dB impedance bandwidth of the manufactured loaded planar monopole antenna was slightly smaller than was achieved in simulation, although the centre frequency remained constant. This difference in bandwidth is not large enough to cause a problem, as the simulated antenna was designed to have a wide enough impedance bandwidth to allow for irregularities due to manufacturing. The manufactured antenna had a -10 dB impedance bandwidth of 5.28 %, compared to the simulated 6.29 % bandwidth, which is higher than the required design minimum of 5 %.

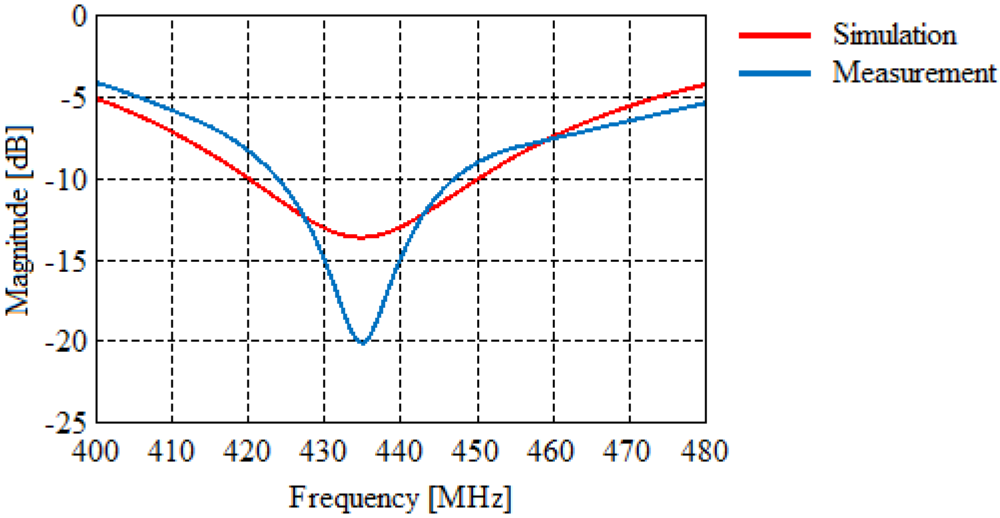

Figure 5.14. Measured (blue) and simulated (red) reflection coefficient for the loaded planar monopole Antenna.

5.3.1.2 Effect of human loading

The effect of human loading on the loaded planar monopole antenna’s reflection coefficient is displayed in Figure 5.15, where the simulated results in (a) are compared with the measured results in (b). As was the case for the standard planar monopole antenna, human loading caused the loaded planar monopole antenna’s reflection coefficient to increase in bandwidth, especially towards the lower frequencies. Although the maximum frequency of the loaded planar monopole antenna’s impedance bandwidth was shifted slightly lower in frequency, it should be noted that the design centre frequency of 433 MHz was still well within the -10 dB reflection coefficient band. While comparing Figure 5.15 (a) and (b) it can be observed that even though the simulated and measured results are very similar, there were still some differences. As was the case for the standard planar monopole antenna, these differences are most likely due to inaccuracies in the simulated model of human tissue, although they did give a fair indication of what would happen in practice.

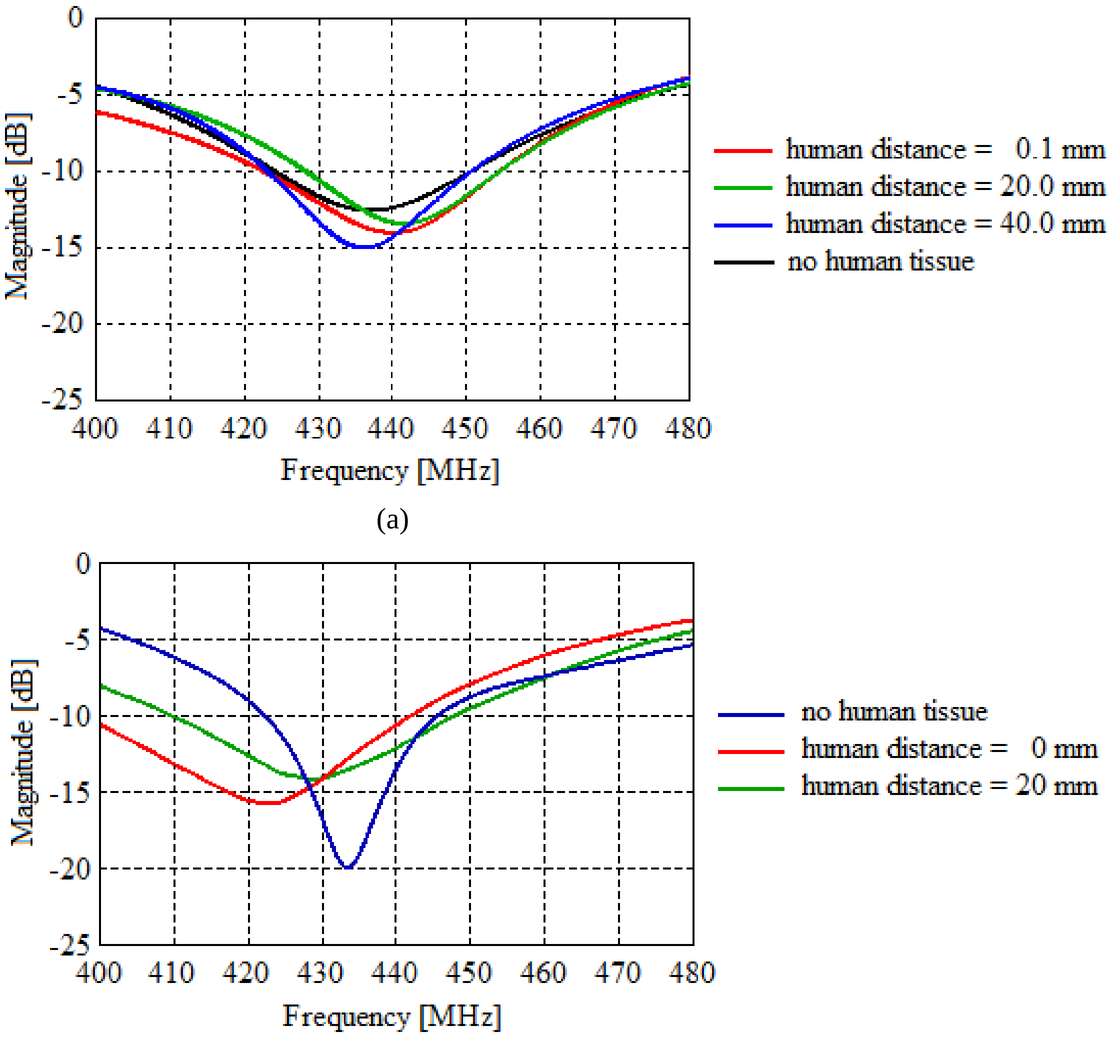

(a)

(b)

Figure 5.15. The effect of human loading on the loaded planar monopole antenna's reflection coefficient. (a) Simulated results. (b) Measured results.

5.3.2 Radiation characteristics

The radiation pattern measurements for the loaded planar monopole antenna were conducted on the same day as for the standard planar monopole antenna, in the large tapered chamber at SAAB Grintek Defence South Africa. Measurement were recorded with an Anritsu 37269D vector network analyser and calibrated based on measurements of the CBL6143A bilog antenna from Teseq. Results were processed and graphed using the MATLAB software package.

5.3.2.1 Gain

The boresight gain was measured from 400 MHz to 460 MHz, where the loaded planar monopole antenna had a reflection coefficient of -10 dB or less from 428 MHz to 446 MHz. In Figure 5.16 it can be observed that the measured results were not as smooth as in simulation. Due to the differences between measured and simulated radiation patterns, and to a lesser extent the narrower measured impedance bandwidth, the boresight gain of the loaded planar monopole antenna increases more with frequency than in simulation. Furthermore, due to the lower reflection coefficient, and the narrower 3 dB beam width, the manufactured antenna had a higher maximum gain. As was the case for the standard planar monopole antenna, the loaded planar monopole antenna also underwent a slight frequency shift in terms of gain but, due to the tolerances that were incorporated in the design, the gain at 433 MHz is still comfortably larger than the design goal of 5 dBi.

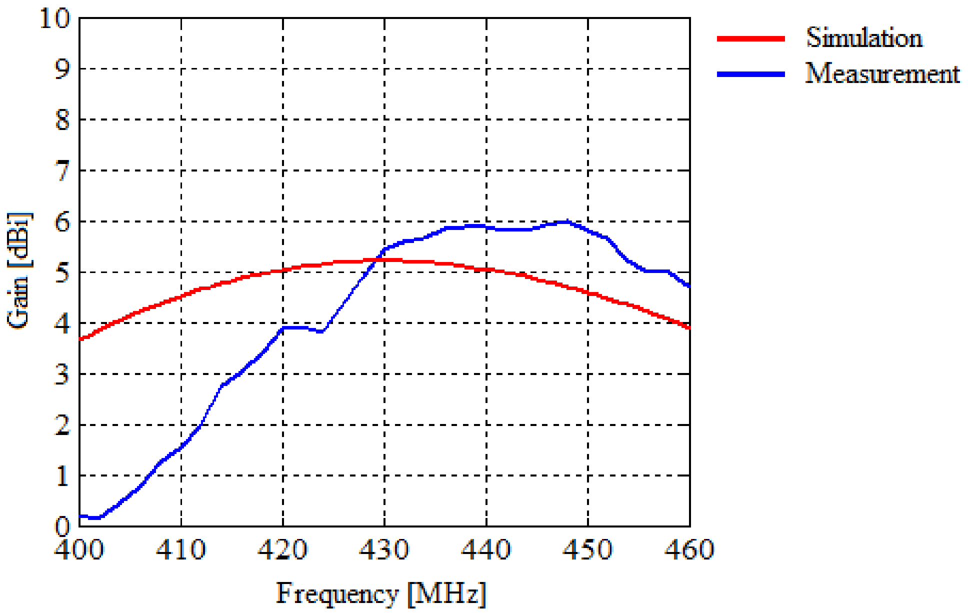

Figure 5.16. Simulated and measured gain as a function of frequency for the loaded planar monopole antenna.

5.3.2.2 Radiation patterns

A comparison between simulated and measured radiation patterns is given in Figure 5.17, where it can be observed that the simulated and measured co-polarization patterns are very similar in form. The measured H-plane 3 dB beam width was 88.64°, compared to a simulated beam width of 109.8°, and the measured E-plane 3 dB beam width was 79.47°, compared to the 94.4° achieved in simulation. Both the E- and H-plane 3 dB beam width was narrower in practice than in simulation, though still wide as both were wider than 70°. The measured cross-polarization was not as good as was achieved in simulation, in fact the simulated cross-polarization in Figure 5.6 (b) is almost unobservable. The measured E-plane cross-polarization was slightly worse than was the case for the standard planar monopole antenna, but the loaded planar monopole antenna still has a boresight cross-polarization in excess of 18 dB.

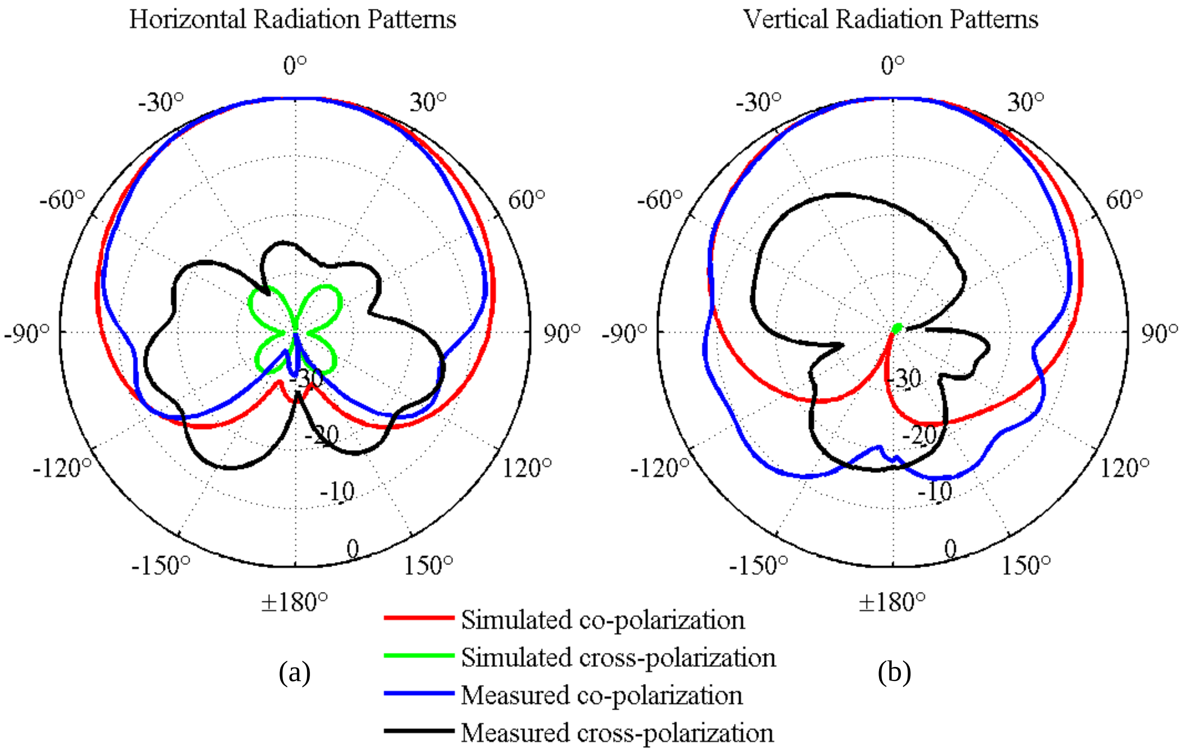

(a)

(b)

Figure 5.17. Normalised simulated and measured far field radiation patterns for the loaded planar monopole antenna. (a) H-plane co- and cross-polarization. (b) E-plane co- and cross-polarization.

The H-plane co-polarization far field magnitude is given in Figure 5.18 below as a function of both horizontal (azimuth) angle, and frequency. In Figure 5.18 it can be seen that the H-plane 3 dB beam width remains largely constant, although a slight increase in beam width with frequency is observable. It should also be noted that the majority of the radiated power is being radiated into the front hemisphere.

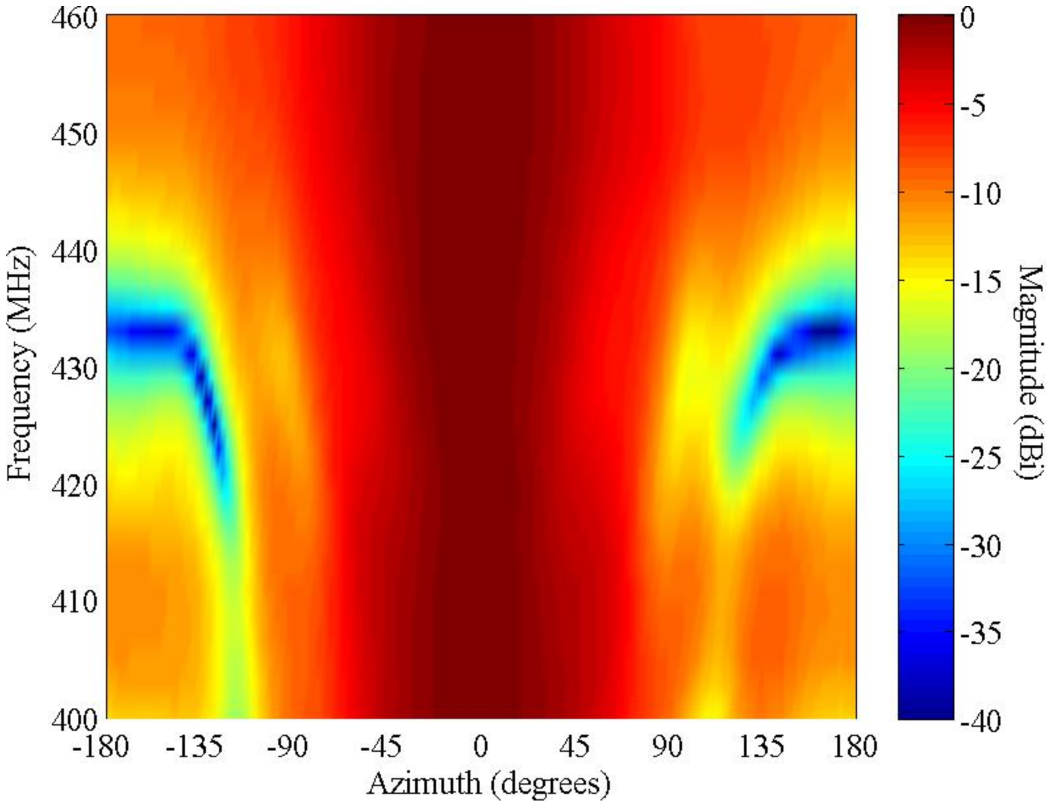

Figure 5.18. Colour plot of the manufactured loaded planar monopole antenna's normalised E-plane co-polarization, with the horizontal (azimuth) angle on the x-axis, the frequency on the y-axis, and the far field magnitude indicated with a colour scale.

The E-plane co-polarization far field magnitude is shown in Figure 5.19 below as a function of both vertical (elevation) angle, and frequency. In Figure 5.19 it can be observed that the majority of energy is being radiated in the front hemisphere and that, although the front hemisphere in general remains largely constant, a slight shift in maximum gain can be observed with a change in frequency. It should also be noted that the E-plane far field pattern is slightly unsymmetrical, which is mostly due to the manner in which the antenna is fed. The slight lack of symmetry is not a problem however, as the differences are not unduly large.

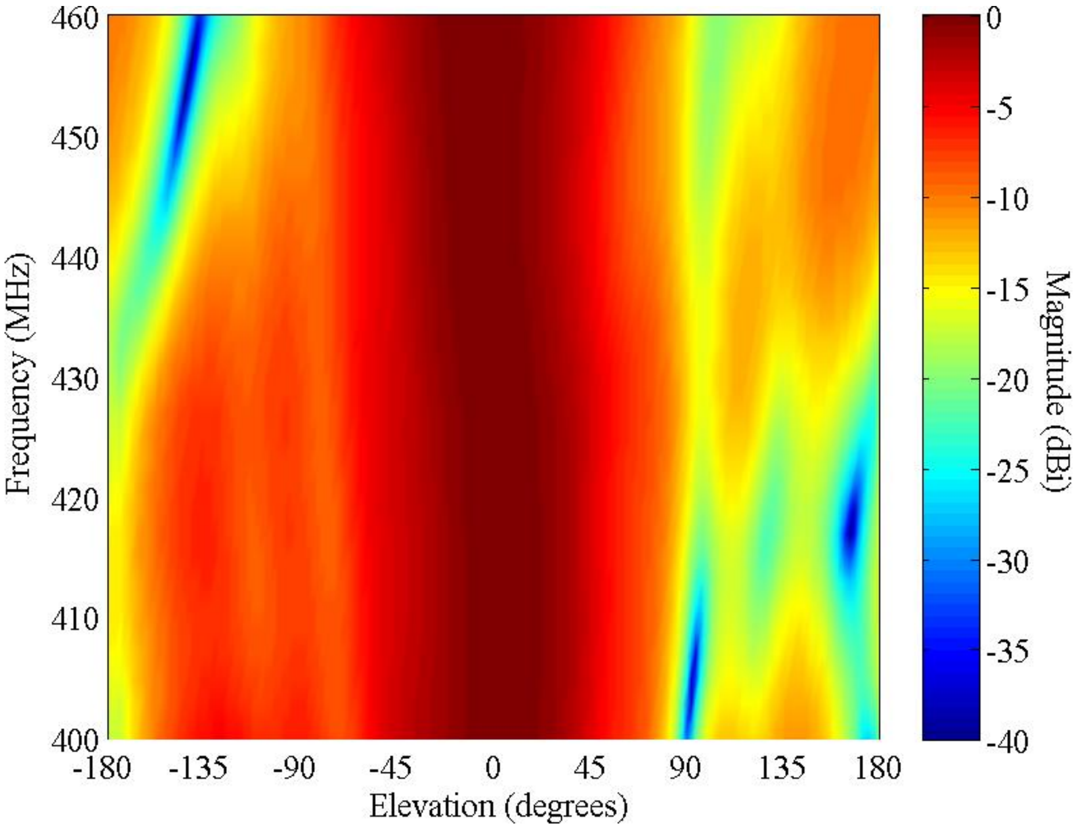

Figure 5.19. Colour plot of the manufactured loaded planar monopole antenna's E-plane co-polarization, with the horizontal (azimuth) angle on the x-axis, the frequency on the y-axis, and the far field magnitude indicated with a colour scale.

Figure 5.20, Figure 5.21, and Figure 5.22 show the measured radiation patterns, i.e. both E-plane and H-plane co- and cross-polarization, in 4 MHz increments, from 425 MHz to 445 MHz. Figure 5.20, Figure 5.21, and Figure 5.22 give an indication of how the loaded planar monopole antenna's radiation patterns change over frequency.

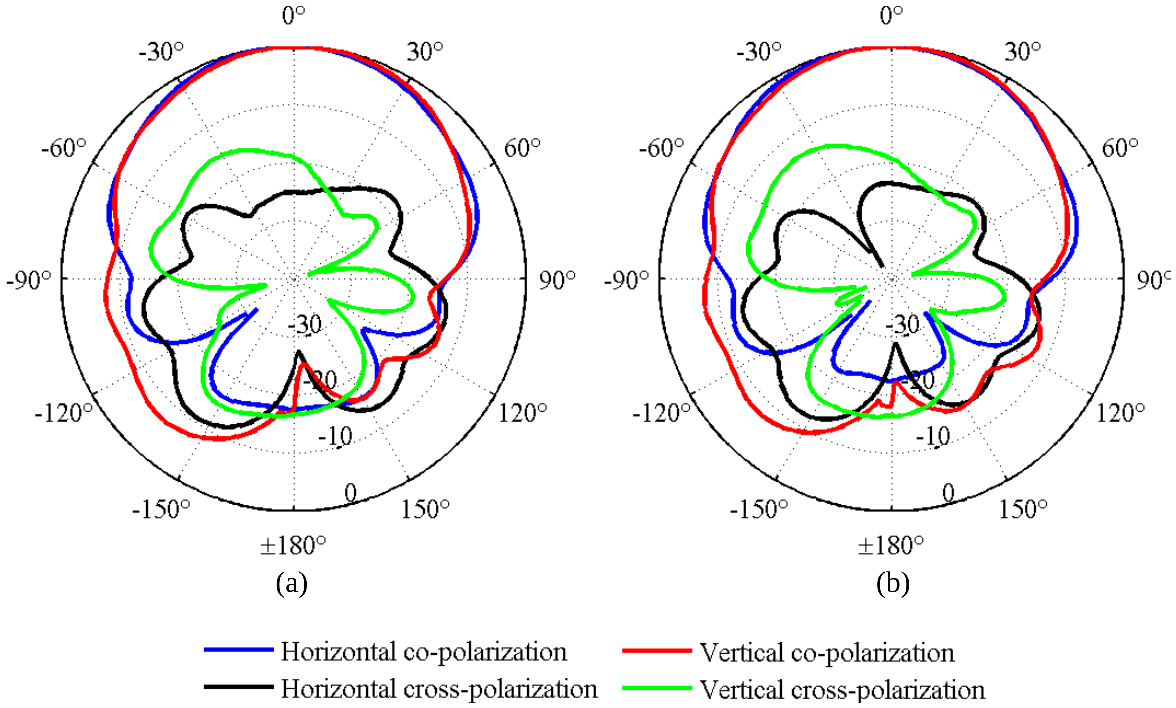

(a) (b)

Figure 5.20. Normalised measured radiation patterns. (a) 425 MHz. (b) 429 MHz.

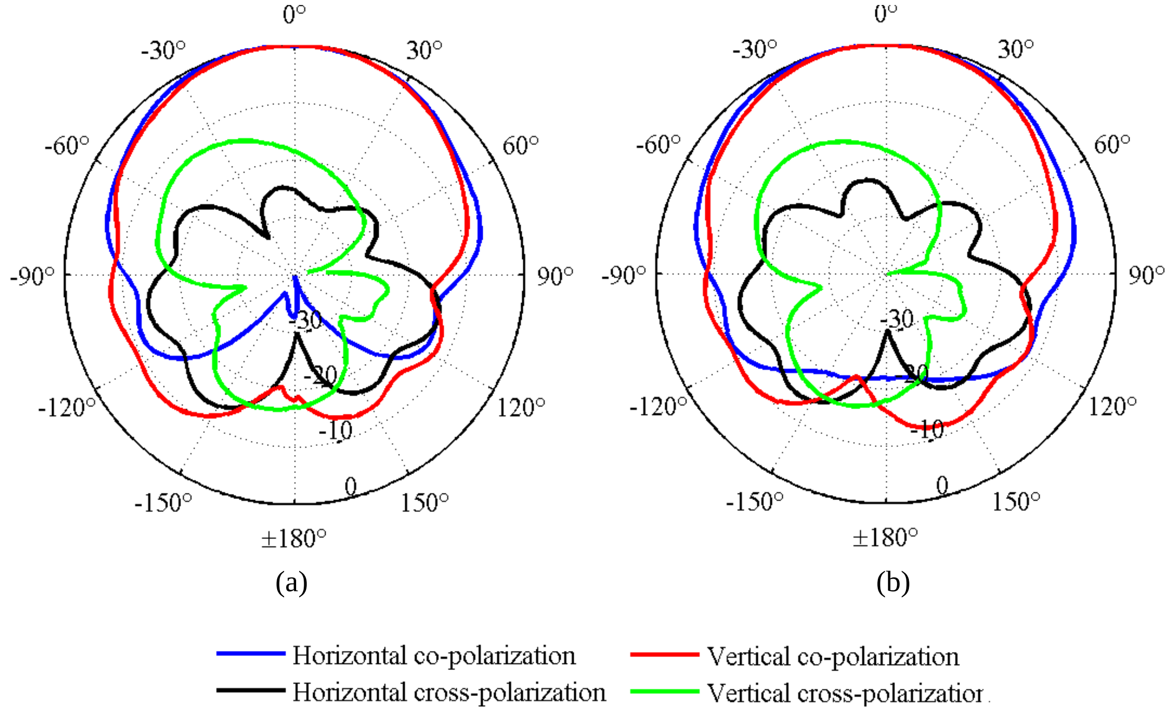

(a) (b)

Figure 5.21. Normalised measured radiation patterns. (a) 433 MHz. (b) 437 MHz.

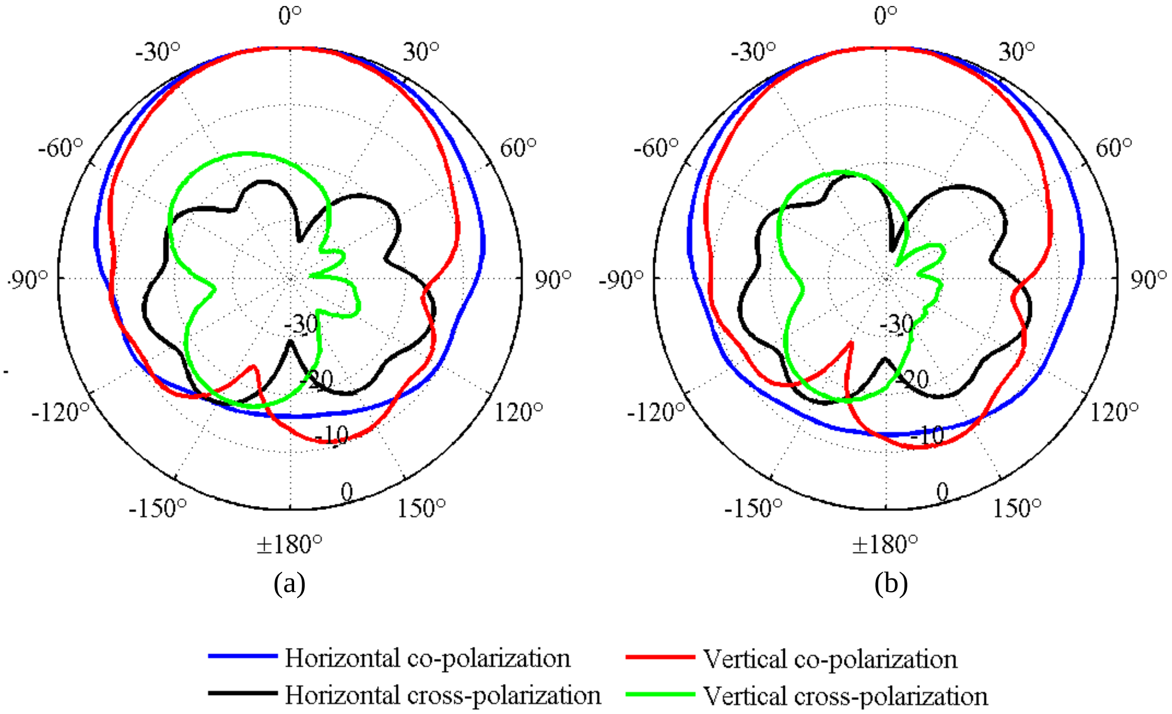

Figure 5.22. Normalised measured radiation patterns. (a) 441 MHz. (b) 445 MHz.

5.3.2.3 Power radiated forward

The power radiated forward is indicated by the ratio between the average power radiated in the front hemisphere to the average power radiated in the rear hemisphere, referred to below as the front to back power ratio. In Figure 5.23 it can be seen that the measured front to back power ratio was much better than the simulated result at 433 MHz, although it decreased rather sharply further away from 433 MHz. In practice 10 dB or more power is radiated forwards than backwards between 424 MHz and 438 MHz, and the band where at least 6 dB more power is radiated forward is even larger. This means that the loaded planar monopole antenna can confidently be used as a wearable antenna.

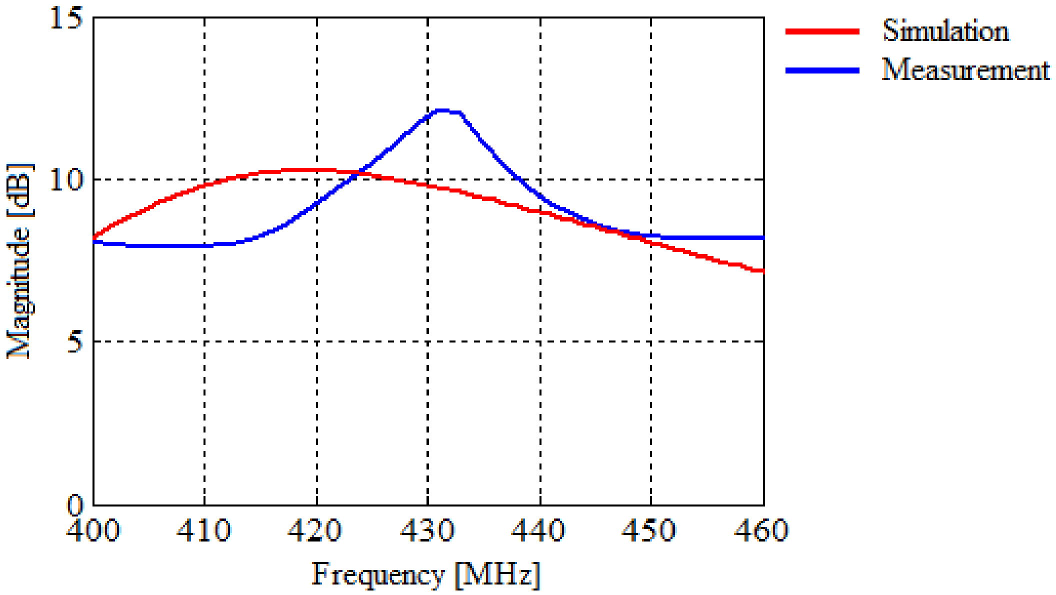

Figure 5.23. Simulated and measured front to back power ratio for the loaded planar monopole antenna. The front to back power ratio is the ratio between the average power radiated in the front hemisphere to the average power radiated in the rear hemisphere

5.4 SUMMARY

The performance of both the standard planar monopole and loaded planar monopole antennas were evaluated through practical measurement. The measured results were compared with the simulated results to validate the accuracy of the simulation models. The simulated results were generally very similar to the practical measurements, which means that the simulation models, and by extension the design procedure, can be taken as accurate and practical.

The reflection coefficients for both the standard planar monopole and loaded planar monopole antennas were measured at the University of Pretoria. The standard planar monopole antenna displayed a shift to a higher frequency compared to simulation, whereas the measured reflection coefficient of the loaded planar monopole antenna corresponded very well with the simulated results. The standard planar monopole antenna had a practical impedance bandwidth of 25.1 %, and the loaded planar monopole antenna had a practical impedance bandwidth of 5.28 %, compared to the simulated 24.2 % and 6.29 % respectively.

For both the standard planar monopole and loaded planar monopole antenna, the measured effects of human loading on reflection coefficient were very similar to that of the simulated models, although both antennas underwent an increase in bandwidth due to a close proximity of human tissue.

The radiation characteristics for both antennas were measured at both the Paardefontein National Antenna Measurement Range in Pretoria, South Africa, and the SAAB Grintek Defence facilities in Centurion, South Africa. Both antennas had slightly narrower 3 dB beam widths at 433 MHz in practice than in simulation, decreasing from the 90° to 100° range to the 80° to 90° range. Both antennas had acceptable front to back power ratios, and both of their boresight gains were acceptably similar in practice and simulation. The simulated and measured co-polarization patterns were very similar for both antennas, but their cross-polarization rejection was not as good in practice as in simulation.

Both antennas were found to be suitable for wearable applications, and the low-cost material that the antennas were manufactured from did not cause them to be impractical or excessively inefficient. Both antennas complied with the design objectives set forth in this investigation.

CHAPTER 6 CONCLUSION

The primary objective for this investigation was to develop a design procedure for a compact wearable antenna to be used in rescue operations in underground mines. As most miners already wear RFID systems, operating at 433 MHz, a wearable directional antenna can be used by rescuers to find the general direction towards the lost miners. To be able to solve this problem the designed antenna was to have a relatively high gain of 5 dBi, and a compact size at less than 0.5 λ_0 by 0.5 λ_0, where λ_0 is the wavelength of 433 MHz in a vacuum. The chosen solution was to use a basic antenna with a reactive impedance surface (RIS) reflector to focus the radiate fields away from the wearer. As it was known beforehand that the final product would be large, and therefore expensive, it was decided to use a low-cost material to manufacture the antenna. FR-4 was selected as the antenna material because it is inexpensive and readily available, at the cost of having high dielectric losses.

Various RIS designs were investigated, and the square patch RIS was found to be most suitable for this investigation. The final RIS design was a 2 by 2 square patch RIS. It was deemed unnecessary to use a complex antenna design, due to the fact that the RIS was already rather large. It was decided to use a basic planar monopole antenna, because integrating even a basic antenna with an RIS would result in a very complex model. Simulations were mainly done in CST Microwave Studio (2014). The final antenna was designed by first designing an RIS unit cell to have a zero-degree reflection coefficient at the design frequency, then the antenna was designed to resonate at the design frequency. Both the RIS unit cell and antenna were first optimised for the design frequency before being combined to form the integrated antenna. The integrated antenna was then optimised according to the design goals.

The aforementioned design goals were to design two antennas: one was designed for the optimal performance achievable with a planar monopole antenna and a 2 by 2 square patch RIS, and the other was designed to be as compact as possible. Section 4.4.2 gives the design procedure that was developed for the standard planar monopole antenna.

In simulation, the standard planar monopole antenna achieved a wide impedance bandwidth of 24.2 %, with a 5 dBi boresight gain bandwidth of 23.4 %. The final size of the standard planar monopole antenna was 0.4 λ_0 long, 0.4 λ_0 wide, and 0.069 λ_0 high. The measured performance of the manufactured standard planar monopole antenna agreed with the expected performance based on the simulation model. The measured -10 dB reflection coefficient bandwidth of the antenna shifted to a marginally higher frequency range than was found in simulation, but the shift was not large enough to cause alarm as the design frequency of 433 MHz still comfortably lay within the measured impedance bandwidth. The antenna's impedance bandwidth also increased moderately to 25.1 %, from the 24.2 % achieved in simulation. The measured far field radiation patterns were very similar to the simulated fields, although the 3 dB beam width decreased from 98.9° to 87.97° in the H-plane, and from 91.2° to 80.58° in the E-plane. There was a ripple on the measured boresight gain that was not present in simulation, however the design goal of 5 dBi at, and around, 433 MHz, with the entire 400 MHz to 500 MHz range falling within 1 dB of 5 dBi. Finally, from 400 MHz to 500 MHz, the ratio of the average power radiated forwards to the average power radiated backwards was consistently larger than 6 dB, which means that more than 80 % of the power would be radiated away from the wearer.

A design procedure was developed for the loaded planar monopole antenna and provided in 4.4.2. In simulation, the loaded planar monopole antenna achieved a wide impedance bandwidth of 6.29 %, which was more than the 5 % required, and a 5 dBi boresight gain bandwidth of 4.88 %. The final size of the standard planar monopole antenna was 0.346 λ_0 long, 0.346 λ_0 wide, and 0.107 λ_0 high. The measured performance of the manufactured loaded planar monopole antenna agreed with the expected performance based on the simulation model. The measured -10 dB reflection coefficient bandwidth of the loaded planar monopole antenna remained largely constant, only decreasing slightly from 6.29 % in simulation to the measured bandwidth of 5.28 %. The measured and simulated far field radiation patterns were very much alike, although the 3 dB beam width decreased from 109.8° to 88.64° in the H-plane, and from 94.4° to 79.47° in the E-plane. As was the case for the standard planar monopole antenna there was a ripple on the measured boresight gain of the loaded planar monopole antenna that was not present in simulation. The frequency where the loaded planar monopole achieved maximum boresight gain shifted higher between the simulated and measured results, however the design goal of 5 dBi at, and around, 433 MHz was still achieved. Finally, the ratio of the average power radiated forwards to the average power radiated backwards was larger than 10 dB at 433 MHz ± 10 MHz, which means that some tolerance is provided, and that the majority of energy is radiated away from the wearer.

With regards to wearability, simulation models were also created to investigate the effects of human loading on the performance of both antennas. According to the simulation models, the presence of human tissue in close proximity to the antennas does not cause the antennas' performance to deteriorate. The only effects that were found in simulation was that a slight frequency shift could occur, and that human loading can cause the antennas' impedance bandwidths to increase. In practice the simulated results were verified as human loading caused the impedance bandwidth for both antennas to increase. For both antennas the practical effects of human loading were more pronounced than in simulation, but the changes did follow the same trends as could be observed in simulation. Human loading did not detune the antennas in such a way as to render the design frequency of 433 MHz outside the respective impedance bandwidths. The differences between the simulated and measured effects of human loading are due to the inaccuracies in available models of human tissue, and the inherent complexity of human bodies.

In summary, a design procedure was developed, two antennas were designed through said procedure, and the final designs were manufactured. The manufactured antennas verified the design procedures, and proved that they are practical. The final designs achieved the goals for this investigation by being compact, wearable, and relatively inexpensive.

The following topics were identified as recommendations for possible future work:

- The designs presented in this investigation could allow for even more inexpensive materials with higher losses to be used in antenna design. This could allow relatively high performance antennas to be manufactured at much lower costs.
- The work done on textile based antennas can be combined with the findings presented here to develop high performance antennas that can comfortably be worn.
- If the available models for human bodies can be improved, antennas can be developed that are practically immune to human loading.
- Further investigation into using RISs to improve antenna wearability can also be pursued.

REFERENCES

[1] A. S. Bhat, B. Raghavendra and G. N. Kumar, "Enhanced passive RFID based disaster management for coal miners," *International Journal of Future Computer and Communication*, vol. 2, no. 5, pp. 476-480, Nov. 2013.

[2] K. Zhang, M. Zhu, Y. Wang, E. Fu and W. Cartwright, "Underground mining intelligent response and rescue systems," *Procedia Earth and Planetary Science*, vol. 1, no. 1, pp. 1044-1053, Sept. 2009.

[3] B. Li, L. Shang, W. Li and L. Chen, "Research on coal mine personnel orientation rescuing system based on RFID," in *International Conference on MultiMedia and Information Technology*, Three Gorges, China, Dec. 2008, pp. 555-557.

[4] I. M. S. ul Huque, K. S. Munasinghe, M. Abolhasan and A. Jamalipour, "SEA-BAN: semi-autonomous adaptive routing in wireless body area networks," in *2013 7th International Conference on Signal Processing and Communication Systems*, Carrara, Australia, Dec. 2013, pp. 1-7.

[5] Z. H. Jiang, D. E. Brocker, P. E. Sieber and D. H. Werner, "A compact, low-profile metasurface-enabled antenna for wearable medical body-area network devices," *IEEE Antennas and Propagation*, vol. 62, no. 8, pp. 4021-4030, Aug. 2014.

[6] L. Shi, J. Yuan, S. Yu and M. Li, "MASK-BAN: movement-aided authenticated secret key extraction utilizing channel characteristics in body area networks," *IEEE Internet of Things Journal*, vol. 2, no. 1, pp. 55-62, Feb. 2015.

[7] A. Michalopoulou, A. Alexandridis, T. Zervos and F. Lazarakis, "A wearable multiband monopole antenna for digital television and wireless communications," in *2014 8th European Conference on Antennas and Propagation (EuCAP)*, The Hague, Netherlands, Apr. 2014, pp. 1398-1402.

[8] G. Marrocco, "RFID antennas for the uhf remote monitoring of human subjects," *IEEE Transactions on Antennas and Propagation*, vol. 55, no. 6, pp. 1862-1870, Jun. 2007.

[9] R. Kohno, K. Hamaguchi, L. Huan-Bang and K. Takizawa, "R&D and standardization of body area network (BAN) for medical healthcare," in *2008 IEEE International Conference on Ultra-Wideband*, Hannover, Germany, Sept. 2008, pp. 5-8.

[10] M. Paulides, J. Bakker, N. Chavannes and G. van Rhoon, “A patch antenna design for application in a phased-array head and neck hyperthermia applicator,” *IEEE Transactions on Biomedical Engineering,* vol. 54, no. 11, pp. 2057-2063, Nov. 2007.

[11] J. Buckley, K. G. McCarthy, B. O'Flynn and C. O'Mathuna, “The detuning effects of a wrist-worn antenna and design of a custom antenna measurement system,” in *2010 European Microwave Conference (EuMC)*, Paris, France, Sept. 2010, pp. 1738-1741.

[12] A. Feresidis, G. Goussetis, S. Wang and J. Vardaxoglou, “Artificial magnetic conductor surfaces and their application to low-profile high-gain planar antennas,” *IEEE Transactions on Antennas and Propagation,* vol. 53, no. 1, pp. 209-215, Jan. 2005.

[13] J. Joubert, J. Vardaxoglou, W. Whittow and J. W. Odendaal, “CPW-fed cavity-backed slot radiator loaded with an AMC reflector,” *IEEE Transactions on Antennas and Propagation,* vol. 60, no. 2, pp. 735-742, Feb. 2012.

[14] H. Mosallaei and K. Sarabandi, “Antenna miniaturization and bandwidth enhancement using a reactive impedance substrate,” *IEEE Transactions on Antennas and Propagation,* vol. 52, no. 9, pp. 2403-2414, Sept. 2004.

[15] K. Sarabandi, A. M. Buerkle and H. Mosallaei, “compact wideband uhf patch Antenna on a Reactive Impedance Substrate,” *IEEE Antennas and Wireless Propagation Letters,* vol. 5, no. 1, pp. 503-506, Dec. 2006.

[16] Trans-Tech, “Trans-Tech Products: SMAT-10,” [Online]. Available: http://www.trans-techinc.com/products_detail.asp?ID=109&Name=SMAT-10.

[17] W. L. Stutzman and G. A. Thiele, *Antenna theory and design*, 3rd ed., New York: John Wiley & Sons, 2013, pp. 23-533

[18] M. R. Yuce and J. Y. Khan, “Antenna design and propagation for WBAN applications,” in *Wireless Body Area Networks: Technology, Implementation, and Applications*, Pan Stanford Publishing, Dec. 2011, pp. 349-373.

[19] P. Van Rysselberghe, “Remarks concerning the Clausius-Mossotti law,” *The Journal of Physical Chemistry*, vol. 36, no. 4, pp. 1152-1155, Jan. 1931.

[20] H. Mosallaei and K. Sarabandi, “Engineered meta-substrate for antenna miniaturization,” *Ann Arbor*, vol. 1001, pp. 191-193, Oct. 2004.

[21] J. Buckley, P. Haigh, C. O'Mathuna and K. G. McCarthy, “Antenna tuning for wearable wireless sensors,” in *2011 IEEE Sensors*, Limerick, Ireland, Oct. 2011, pp. 1990-1993.

[22] A. Sabban, “Compact tunable printed antennas for medical and commercial applications,” in *2013 IEEE International Conference on Microwaves, Communications, Antennas and Electronics Systems*, Tel Aviv, Israel, Oct. 2013, pp. 1-3.

[23] C. A. Balanis, *Antenna theory*, 2nd ed., New York: Wiley, 1997, pp. 339-784.

[24] B. Mandal, A. Chatterjee and S. K. Parui, “A wearable button antenna with FSS superstrate for WLAN health care applications,” in *2014 IEEE MTT-S International Microwave Workshop Series on RF and Wireless Technologies for Biomedical and Healthcare Applications*, London, United Kingdom, Dec. 2014, pp. 1-3.

[25] B. Sanz-Izquierdo, M. I. Sobhy and J. C. Batchelor, “Compact UWB wearable antenna,” in *2007 Loughborough Antennas and Propagation Conference*, Loughborough, United Kingdom, Apr. 2007, pp. 121-124.

[26] S. Sankaralingam, S. Dhar, S. Dasgupta and B. Gupta, “Performance of fully fabric wearable circular patch antennas in the vicinity of human body at 2.45 GHz,” in *2013 International Symposium on Electromagnetic Theory*, Hiroshima, Japan, May 2013, pp. 634-636.

[27] H. Iwasaki and N. Noda, “Evaluation related to finger position and rotation of wearable dual band inverted-F finger ring antenna,” in *2015 International Symposium on Antennas and Propagation*, Hobart, Australia, Nov. 2015, pp. 1-4.

[28] K. Nate and M. M. Tentzeris, “A novel 3-D printed loop antenna using flexible NinjaFlex material for wearable and IoT applications,” in *2016 IEEE Electrical Design of Advanced Packaging and Systems Symposium*, Honolulu, United States, Dec. 2015, pp. 171-174.

[29] A. Babar, L. Ukkonen and L. Sydanheimo, “Dual UHF RFID band miniaturized multipurpose planar antenna for compact wireless systems,” in *2010 International Workshop on Antenna Technology*, Lisbon, Portugal, Mar. 2010, pp. 1-4.

[30] J. Buckley, K. McCarthy, L. Loizou, B. O'Flynn and C. O'Mathuna, “A dual-ISM-band antenna of small size using a spiral structure with parasitic element,” *IEEE Antennas and Wireless Propagation Letters*, vol. 15, no. 99, pp. 630-633, Aug. 2015.

[31] J. Buckley, D. Gaetano, K. McCarthy, L. Loizou, B. O'Flynn and C. O'Mathuna, “Compact 433 MHz antenna for wireless smart system applications,” *IEEE Electronics Letters*, vol. 50, no. 8, pp. 572-574, Apr. 2014.

[32] A. Kiourti and K. Nikita, “Miniature scalp-implantable antennas for telemetry in the MICS and ISM bands: design, safety considerations and link budget analysis,” *IEEE Transactions on Antennas and Propagation*, vol. 60, no. 8, pp. 3568-3575, Aug. 2012.

[33] H. Wang, Z. Zhang, Y. Li and Z. Feng, “A dual-resonant shorted patch antenna for wearable application in 430MHz band,” *IEEE Transactions on Antennas and Propagation*, vol. 61, no. 12, pp. 6195-6200, Sept. 2013.

[34] S. Y. Suh, A. E. Waltho, L. Krishnamurthy, D. Souza, S. Gupta, H. K. Pan and V. K. Nair, “A miniaturized dual-band dipole antenna with a modified meander line for laptop computer application in the 2.5 and 5.25 GHz WLAN band,” *2006 Antennas and Propagation Society International Symposium*, Albuquerque, United States of America, Jul. 2006, pp. 2617-2620.

[35] J. E. Ruyle, “Investigation on placement sensitivity of meandered dipole performance for RFID systems,” in *Proceedings of the 2012 IEEE International Symposium on Antennas and Propagation*, Chicago, United States of America, Jul. 2012, pp. 1-2.

[36] M. Kanesan, “The effect of lossy dielectric objects on a UHF RFID meander line antenna,” in *Proceedings of the 2012 IEEE International Symposium on Antennas and Propagation*, Chicago, United States of America, Jul. 2012, pp. 1-2.

[37] G. Marrocco, “The art of UHF RFID antenna design: impedance-matching and size-reduction techniques,” *IEEE Antennas and Propagation Magazine*, vol. 50, no. 1, pp. 66-79, Feb. 2008.

[38] K. Jikwon, O. Il-Young, K. Dongsu, K. Tae-Wan and Y. Jong-Gwan, “Design of a meandered slot antenna for UHF RFID applications,” in *2010 IEEE Antennas and Propagation Society International Symposium*, Toronto, Canada, Jul. 2010, pp. 1-4.

[39] M. Z. A. Abd Aziz, Z. Zakaria, M. N. Husain, N. A. Zainuddin, M. A. Othman and B. H. Ahmad, “Investigation of dual and triple meander slot to microstrip patch antenna,” in *2013 Conference on Microwave Techniques*, Pardubice, Czech Republic, Apr. 2013, pp. 36-39.

[40] K. Hyungrak and J. Y. Young, “Compact microstrip-fed meander slot antenna for harmonic suppression,” *Electronics Letters,* vol. 39, no. 10, pp. 762-763, May, 2003.

[41] C. Calabrese and G. Marrocco, “Meandered-slot antennas for sensor-RFID tags,” *IEEE Antennas and Wireless Propagation Letters,* vol. 7, no. 1, pp. 5-8, Feb. 2008.

[42] H. M. Chen, Y. F. Lin, P. S. Cheng, H. H. Lin, C. T. P. Song and P. S. Hall, “Parametric study on the characteristics of planar inverted-F antenna,” *IEE Proceedings - Microwaves, Antennas & Propagation,* vol. 152, no. 6, pp. 534-538, Dec. 2005.

[43] H. T. Chattha, T. Huang, L. Yang and X. Zhu, “An ultra-wideband planar inverted-F antenna,” *Microwave & Optical Technology Letters,* vol. 52, no. 10, pp. 2285-2288, Oct. 2010.

[44] S. Villeger, P. Le Thuc, R. Staraj and G. Kossiavas, “Dual-band planar inverted-F antenna,” *Microwave and Optical Technology Letters*, vol. 38, no. 1, pp. 40-42, Jul. 2003.

[45] J. P. Gianvittorio and Y. Rahmat-Samii, “Fractal antennas: a novel antenna miniaturization technique and applications,” *IEEE Antennas and Propagation,* vol. 44, no. 1, pp. 36, Feb. 2002.

[46] J. L. Volakis (2007). “Fractal antennas,” in *Antenna engineering handbook.* (4th Ed.) [Online]. Available: http://accessengineeringlibrary.com/browse/antenna-engineering-handbook-fourth-edition/p200129ad99733_1001

[47] A. Sabban, *Low-visibility antennas for communication systems*, New York: CRC Press, Sept. 2016, pp. 133-225.

[48] N. Cohen, “Fractal antenna applications in wireless telecommunications,” *Electronics Industries Forum of New England*, Boston, United States of America, May 1997, pp. 43-49.

[49] L. Lizzi and G. Oliveri, “Hybrid design of a fractal-shaped GSM/UMTS antenna,” *Journal of Electromagnetic Waves and Applications*, vol. 24, no. 5, pp. 707-719, Apr. 2012.

[50] J. Abraham, K. Aju and T. Mathew, “Microstrip antenna based on Durer Pentagon fractal patch for multiband wireless applications,” in *2014 International Conference on Information Communication and Embedded Systems*, Chennai, India, Feb. 2014, pp. 1-5.

[51] E. E. C. de Oliveira, P. H. da F. Silva, A. L. P. S. Campos and S. G. da Silva, “Overall size antenna reduction using fractal elements,” *Microwave & Optical Technology Letters*, vol. 51, no. 3, pp. 671-675, Mar. 2009.

[52] R. V. Petrov, A. S. Tatarenko, G. Srinivasan and J. V. Mantese, “Antenna miniaturization with ferrite–ferroelectric composites,” *Microwave and Optical Technology Letters*, vol. 50, no. 12, pp. 3154-3157, Dec. 2008.

[53] C. R. Simovski, P. Maagt and I. V. Melchakova, “High-impedance surfaces having stable resonance with respect to polarization and incidence angle,” *IEEE Transactions on Antennas and Propagation*, vol. 53, no. 3, pp. 908-914, Mar. 2005.

[54] M. Hosseini, A. Pirhadi and M. Hakkak, “Design of an AMC with little sensitivity to angle of incidence using an optimized Jerusalem cross FSS,” in *IEEE International Workshop on Antenna Technology: Small Antennas and Novel Metamaterials*, Chiba, Japan, Mar. 2006, pp. 245-248.

[55] M. Hosseini and M. Hakkak, “Characteristics estimation for jerusalem cross-based artificial magnetic conductors,” *IEEE Antennas and Wireless Propagation Letters*, vol. 7, no. 4, pp. 58-61, Apr. 2008.

[56] A. Kush and A. Arokiaswami, “Triple-band compact circularly polarised stacked microstrip antenna over reactive impedance meta-surface for GPS applications,” *IET Microwaves, Antennas & Propagation,* vol. 8, no. 13, pp. 1057-1065, Oct. 2014.

[57] A. Vallecchi, M. Albani and F. Capolino, “Planar metamaterial transverse equivalent network and its application to low-profile antenna designs,” in *2009 3rd European Conference on Antennas and Propagation*, Berlin, Germany, Mar. 2009, pp. 861-865.

[58] J. Wu and K. Sarabandi, “Reactive impedance surface TM mode slow wave for patch antenna miniaturization,” *IEEE Antennas and Propagation Magazine,* vol. 56, no. 6, pp. 279-293, Dec. 2014.

[59] S. Saadat, H. Mosallaei and E. Afshari, “Radiation-efficient 60 Ghz on-chip dipole antenna realised by reactive impedance metasurface,” *IET Microwaves, Antennas & Propagation*, vol. 7, no. 2, pp. 98-104, Jan. 2013

[60] A. Vallecchi, F. Capolino, J. De Luis and F. De Flaviis, “A low profile folded dipole antenna on a reactive high impedance substrate,” in *2009 International Conference on Electromagnetics in Advanced Applications*, Torino, Italy, Sept. 2009, pp. 1062-1065.

[61] M. N. Suma, B. P. C. and P. Mohanan, “A wideband printed monopole antenna for 2.4 GHz WLAN applications,” *Microwave and Optical Technology Letters*, vol. 48, no. 5, pp. 871-873, May 2006.

[62] N. Pascoe, Reliability technology: principles and practice of failure prevention in electronic systems, John Wiley & Sons, Mar. 2011.

[63] C. P. Wong, Polymers for electronic & photonic application, Elsevier, Oct. 2013, pp. 120 -650.

[64] D. M. Pozar, Microwave engineering, 4th ed., Hoboken: John Wiley and Sons, 2012, pp. 10-316.

[65] A. R. Djordjevic, R. M. Biljie, V. D. Likar-Smiljanic and T. K. Sarkar, “Wideband frequency-domain characterization of FR-4 and time-domain causality,” *IEEE Transactions on Electromagnetic Compatibility*, vol. 43, no. 4, pp. 662-667, Nov. 2001.

[66] Y. Tikhov, Y. K and Y.-H. M., “A novel small antenna for passive RFID transponder,” *2005 European Microwave Conference*, Paris, France, Oct. 2005, pp. 4-6.

[67] W. H. and K. Sarabandi, “Low-profile, multi-element, miniaturized monopole antenna,” *IEEE Transactions on Antennas and Propagation*, vol. 57, no. 1, pp. 72-80, Jan. 2009.

[68] Y. Zhou, “A novel slot antenna for UHF RFID tag,” *2010 IET 3rd International Conference on Wireless, Mobile and Multimedia Networks*, Beijing, China, Sept. 2010, pp. 254-257.

[69] Y. Zhou, Z. Z and Y. Hong, “An effective fast matching oriented slot antenna designing method with RFID tag chip,” *2007 International Symposium on Microwave, Antenna, Propagation and EMC Technologies for Wireless Communications*, Hangzhou, China, Aug. 2007, pp. 575-578.

[70] W. Zeng, X. Li and J. Liu, “A dual-band RFID slot tag antenna for ITS application,” *2013 3rd International Conference on Consumer Electronics, Communications and Networks*, Xianning, China, Nov. 2013, pp. 5-7.

[71] J. Lu, Y. Zhou and C. Zheng, “Design of unsymmetrical slot antenna based on ANN for RFID tag,” *2010 International Conference on Microwave and Millimeter Wave Technology*, Chengdu, China, May 2010, pp. 317-320.